AGH UNIVERSITY OF KRAKOW

FIELD OF SCIENCE: NATURAL SCIENCES

SCIENTIFIC DISCIPLINE: PHYSICAL SCIENCES

DOCTORAL DISSERTATION

Electronic transport and topological superconductivity in nanoscopic Josephson junctions

Author : Dibyendu Kuiri
Supervisor: Dr. hab. inż. Michał P. Nowak, prof. AGH

AGH University of Krakow
Academic Center for Materials and Nanotechnology

Krakow, 2025

I dedicate this thesis to my beloved parents who always believed in me and allowed me the freedom to follow my own path. I also dedicate it to my brother Shibendu and my sister Anisha for their devotion to our parents in my absence, to my grandmother for her constant love and support, and to my late grandfather whose guidance has shaped me since childhood.

Declaration

Declaration of the Author of this dissertation:

Aware of legal responsibility for making untrue statements I hereby declare that I have written this dissertation myself and all the contents of the dissertation have been obtained by legal means.

.....

Date, Author's signature

Declaration of the thesis Supervisor:

This dissertation is ready to be reviewed.

.....

Date, Supervisor's signature

Acknowledgements

This thesis would not have been possible without the collective support, encouragement, and kindness of many people.

Most importantly, I would like to express my deepest gratitude to my PhD supervisor, Prof. Michał P. Nowak, for his immense support, guidance, and constant encouragement throughout my journey. From my first day in Poland and the initial stages of my PhD studies, he not only supported me academically, but also helped me in many personal aspects of life. I am truly grateful for his insightful teaching, as I learned something new almost every day under his guidance. I am always inspired by his work, and I remain grateful for his belief in me. Through his mentorship, I have gained invaluable lessons that have shaped me both as a researcher and as a person. I will always be grateful to him for creating a work environment that I could only have dreamed of.

I am deeply grateful to Prof. Michał Zegrodnik and Prof. Andrzej Biborski for their constant support and for creating a friendly, open, and collaborative group environment. In my first year, I was the only student in the group, yet my supervisor and both professors treated me as a colleague, showing respect and openness that continued throughout my PhD. I also thank them for introducing group meetings, which provided a valuable platform to share updates, exchange ideas, and address challenges, enriching my research experience. I am also grateful to Prof. Marek Przybylski for his support with official matters, especially in handling conference payments.

I acknowledge the collaboration of Prof. Srijit Goswami, Prof. Paweł Wójcik, and Prof. Andrzej Biborski in my PhD project. I thank my office colleagues Shalini, Jorge, Waseem, and Palash for making our group environment enjoyable, and Ewelina for sharing valuable information about AGH scholarships. I also appreciate the support of Kasia, Vitaly, and all ACMiN employees and students for creating a welcoming atmosphere.

I feel fortunate to have had a wonderful circle of friends in Kraków, especially Sagar, Rupam, Avrajyoti, Shalini, Rwik, and Tanmay, whose support helped me through difficult times. During my master's studies, I was also blessed with close friends including Sandip, Haradhan, Kushal, Sayan, Sagar, Vijay, Hasan, Hemlata, Pradeep, Ishfaq, Anubhav, and many others, whose friendship made that journey truly memorable.

I am thankful to my BSc physics teachers, Samiran Majee and Moumita Patra, whose teaching sparked my interest in physics, and to my BSc friends Kushal, Satya, Jayanta, Suraj, and Manu for their companionship. I am especially grateful to my elder brother Tanmay, Shibendu, and Anirban, who are my go-to persons in any crisis.

Finally, I acknowledge the financial support from the National Science Center (NCN) under Agreement No. UMO-2020/38/E/ST3/00418, and the Polish high-performance computing infrastructure PLGrid (HPC Center: ACK Cyfronet AGH) for providing computational facilities and support within Grant Nos. PLG/2024/017374 and PLG/2025/018486.

Abstract

Majorana zero modes, arising in topological superconductors, are promising building blocks for fault-tolerant quantum computation due to their non-Abelian exchange statistics and intrinsic robustness against decoherence. Planar Josephson junctions have emerged as a versatile platform for engineering Majorana zero modes and studying topological superconductivity. This thesis investigates the underlying physics of Andreev bound states, Majorana zero modes, and transport properties of Josephson junctions. First, Andreev bound state spectra of junctions in a perpendicular magnetic field are investigated. It is shown how the vector potential produces the relative phase shifts in the spectra, providing a transparent explanation of experimental tunneling spectroscopy measurements. Building on this, the interplay between spin–orbit coupling and magnetic field in Josephson junctions is studied with the demonstration of how nonlocal conductance can serve as a reliable probe of topological superconductivity. Realistic device limitations, such as phase slips in junctions embedded in superconducting loops, are shown to hinder the emergence of Majorana zero modes at low magnetic fields. To address this issue, it is proposed to elongate the junction, which widens the accessible phase interval and reduces the magnetic field required for the topological transition. This work contributes to the study of Josephson junctions as a promising platform for realizing Majorana zero modes, by exploring their transport properties, and by guiding experimental implementations.

Streszczenie

Stany zerowe Majorany, powstające w topologicznych nadprzewodnikach, stanowią obiecujące elementy budulcowe odpornych na błędy komputerów kwantowych dzięki swoim nieabelowym statystykom wymiany oraz wewnętrznej odporności na dekoherencję. Planarne złącza Josephsona rozważane są jako wszechstronna platforma do realizacji stanów zerowych Majorany i badania topologicznego nadprzewodnictwa. Niniejsza rozprawa analizuje fizykę stanów związanych Andreeva, stanów zerowych Majorany oraz właściwości transportowych złącz Josephsona. W pierwszej kolejności badane są widma stanów związanych Andreeva w złączach poddanych prostopadłemu polu magnetycznemu. Pokazano, w jaki sposób potencjał wektorowy wywołuje względne przesunięcia fazowe w widmach, dostarczając przejrzystego wyjaśnienia eksperymentalnych widm spektroskopii tunelowej. Następnie analizowane jest współdziałanie sprzężenia spin-orbita i pola magnetycznego w złączach Josephsona, przy czym wykazano, że nielokalna konduktancja może pełnić rolę wiarygodnej sondy topologicznego nadprzewodnictwa. Wykazano również, że realistyczne ograniczenia urządzeń, takie jak przeskoki fazowe w złączach osadzonych w pętlach nadprzewodzących, utrudniają pojawianie się stanów zerowych Majorany przy niskich polach magnetycznych. Aby rozwiązać ten problem, zaproponowano wydłużenie złącza, co poszerza dostępny przedział fazowy i zmniejsza wymagane pole magnetyczne dla przejścia topologicznego. Niniejsza praca wnosi wkład do badań nad złączami Josephsona jako obiecującej platformy do realizacji stanów zerowych Majorany, poprzez analizę ich właściwości transportowych oraz wspieranie rozwoju implementacji eksperymentalnych.

Table of contents

Chapter 1

Introduction

1.1 Overview of the research

Classical computers, such as those in our laptops or even the world's fastest supercomputers, are highly effective for many tasks, but they face fundamental limitations when dealing with complex quantum problems. This limitation arises from the exponential growth of the Hilbert space with system size [1]. For instance, simulating a system with just a few dozen particles already requires a classical computer to process an exponentially large number of configurations [2].

An illustrative example is provided by spin chains, such as those described by the Ising or Heisenberg models, which consist of one-dimensional arrays of spin-1/2 particles. Since each spin has two possible basis states, the Hilbert-space dimension grows exponentially as 2^N for a system of N spins [3].

Due to this exponential growth, exact diagonalization is only feasible for very small clusters, typically up to about 20 spins, beyond which the method is no longer feasible [4, 5]. Fermionic lattice systems such as the Hubbard model, where each site may be empty or occupied by an electron with spin, exhibit the same exponential complexity, further underscoring the limitations of classical approaches to quantum many-body problems [6, 7].

To overcome these limitations, new approaches are being explored, most notably quantum computing. Quantum computers encode and manipulate information using quantum bits (qubits) [2]. Unlike classical bits, qubits can exist in superpositions of states, offering the potential to solve problems that are intractable for classical computers [8–10]. Qubits can be realized in various physical platforms, such as electron spins or superconducting circuits, but they are highly sensitive to environmental noise, which can easily lead to errors.

One way to fix errors in quantum computers is quantum error correction, which spreads information across many physical qubits to make a single, more reliable logical qubit. However, this method requires a lot of extra qubits, sometimes more than 1000 physical qubits for just one logical qubit, which is a big challenge. A different approach is to use topological qubits,

which store information in pairs of Majorana zero modes (MZMs) that are spatially separated. These are naturally protected from errors because they're less affected by disturbances, making them a great option for building stable, fault-tolerant quantum computers [11].

In particular, the quantum information encoded in MZMs is topologically protected: it is stored non-locally in the fermion parity degrees of freedom that are shared between spatially separated Majoranas. This non-local encoding makes the information inherently robust against local perturbations and common sources of decoherence. Moreover, logical operations can be implemented through the braiding of Majoranas, and due to their non-Abelian exchange statistics, the resulting transformations depend only on the topology of the exchange path rather than microscopic details such as trajectory or timing [12, 13]. Topological superconductors (TSCs) are the natural host materials for MZMs [14]. In contrast, trivial superconductors lack such topological features and do not support MZMs. The presence of MZMs in topological superconductors makes them particularly promising for applications in topological quantum computing.

A well-known example is the spinless p-wave superconductor, which supports MZMs, but unfortunately such superconductors do not occur naturally, particularly as two-dimensional materials. Scientists came up with an idea to host MZMs using s-wave superconductors (abundant in nature). This can be realized by placing a one-dimensional semiconducting nanowire with strong spin-orbit coupling in proximity to an s-wave superconductor and applying an in-plane magnetic field, leading to the emergence of MZMs[15, 16]. In a pivotal study, Mourik et al. [17] provided a strong signature for MZMs, they observed zero-bias conductance peaks (ZBPs) in tunneling spectroscopy measurements, a characteristic that matches theoretical predictions for MZMs. Despite these findings, further studies indicate that ZBPs alone are not conclusive evidence of true MZMs; as elaborated in Sec. 1.5.1.

An alternative and promising platform for hosting MZMs are Josephson junctions (JJs), particularly those incorporating two-dimensional electron gas (2DEG) heterostructures, which are a highly effective platform for hosting MZMs and achieving topological superconductivity [18, 19], with a more detailed discussion provided in Sec. 1.5.2.

This thesis begins with a collaborative study, in which we provided a theoretical explanation of recent experimental observations of Andreev bound states (ABSs) in planar JJs [20]. As discussed earlier, planar JJs have been proposed as potential hosts of MZMs [19, 21, 22], whose location and coupling can be tuned by the vector potential [21]. In such junctions, the magnetic vector potential induces counterpropagating currents, generates Josephson vortices, and produces the characteristic Fraunhofer interference pattern in the critical current [21, 23]. Understanding the properties of the ABS spectrum is, therefore, a prerequisite for realizing MZMs in JJs.

In this work, shown in Chapter 5, our main focus was to investigate how the magnetic vector potential influences ABSs in planar JJs. Experimentally, tunneling spectroscopy was performed at both ends of the junction, revealing distinct ABS spectra: both edge probes detected ABSs

localized near the tunneling barriers. To interpret these findings, we developed a toy model that, despite its simplicity, captures the essential physics of ABSs under the influence of the magnetic vector potential. The model and further numerical calculations show that the local superconducting phase difference induced by the vector potential has equal magnitude but opposite sign at the two ends of the junction. This phase shift directly governs the spatial localization of the ABSs, which under strong magnetic fields tend to localize next to the barriers. In this way, the model provides a transparent physical explanation of the tunneling spectra and successfully reproduces the experimental observations. This finding also allows us to estimate the relative positions of localized ABSs, enhancing our understanding of phase-controlled topological superconductivity in planar JJs.

Magnetic field, superconductivity, and spin-orbit coupling (SOC) are the three key ingredients required to study MZMs. In planar JJs, the superconducting phase difference provides an additional knob for controlling the topological transition [19, 24].

Building on this understanding, Chapter 6 presents our study of spin effects in the system and their role in the emergence of topological superconductivity. Although both local and nonlocal spectroscopy have been performed on planar SNS junctions in the tunneling regime, clear signatures of the topological transition have remained elusive [25, 26]. In this work [27], we theoretically investigate how nonlocal conductance measurements can reveal hallmarks of topological superconductivity.

In realistic devices, the phase bias is typically imposed by threading magnetic flux through a superconducting loop embedding the SNS junction [20, 28]. Such loops have finite inductance and induce phase slips. These phase slips skip large regions of phase space near π, which is the most crucial region for realizing MZMs. As a result, they strongly hinder the emergence and detection of MZMs at low magnetic fields.

As we learned from the previous work, MZMs cannot be realized at low magnetic fields because phase slips prevent access to the crucial region near π [27, 29]. Consequently, experiments typically require large in-plane magnetic fields to extend the topological phase. However, large fields suppress superconductivity. In Ref. [30], detailed in Chapter 7, we addressed these limitations by proposing an alternative route to stabilize and extend the topological phase in planar junctions. We demonstrated that elongating the junction can significantly widen the phase interval over which topological superconductivity emerges, thereby reducing the magnetic fields required for the transition.

1.2 Bogoliubov-de Gennes formalism for superconductivity

One of the most remarkable phenomena in condensed matter physics is superconductivity, which was discovered by Kamerlingh Onnes in 1911 [31]. However, the first microscopic theory, known as the BCS theory [32, 33] was developed later in 1957 by Bardeen, Cooper,

and Schrieffer. They discovered that two electrons near the Fermi surface, with opposite momentum and opposite spins ($k_\uparrow$ and -$k_\downarrow$) form a Cooper pair. This pairing happens because of electron-phonon coupling.

The BCS Hamiltonian in the second quantization, describing the pairing of electrons into Cooper pairs, is given by:

$$\hat{H}_{\mathrm{BCS}} = \sum_{k,\sigma} \varepsilon_k c^\dagger_{k\sigma} c_{k\sigma} - \sum_{k,k'} V_{kk'} c^\dagger_{k\uparrow} c^\dagger_{-k\downarrow} c_{-k'\downarrow} c_{k'\uparrow}, \tag{1.1}$$

where, $\varepsilon_k = \frac{\hbar^2 k^2}{2m} - \mu$ is the free electron term, m represents the effective mass, μ is the chemical potential. The second term represents the scattering process in which a Cooper pair with momenta $(k, -k)$ is scattered into another pair with momenta $(k', -k')$, with a scattering amplitude $V_{kk'}$ and $c^\dagger_{k\sigma}$ and $c_{k\sigma}$ are the creation and annihilation operators for an electron with momentum k and spin $\sigma(\uparrow$ or $\downarrow)$. The mean field approach is essential, as it accounts for the coherent ground state of the BCS Hamiltonian, where operator pairs such as $c_{-k'\downarrow} c_{k'\uparrow}$ produce non-zero average values. Single-particle excitations exist in states that are separated from the condensate at the Fermi energy E_F by an energy gap, known as the pair potential Δ. These excitations, referred to as Bogoliubov quasiparticles, consist of both electron and hole components, denoted by u_k and v_k, respectively. They are described using the Bogoliubov–de Gennes (BdG) equations within the framework of the mean-field approximation [34].

$$\begin{bmatrix} H & \Delta \\ \Delta^* & -H \end{bmatrix} \begin{bmatrix} u_k \\ v_k \end{bmatrix} = E \begin{bmatrix} u_k \\ v_k \end{bmatrix}. \tag{1.2}$$

H is the one-electron Hamiltonian defined as

$$H = -\frac{\hbar^2}{2m^*} \nabla^2 + V(r) - \mu, \tag{1.3}$$

where μ is the chemical potential and m^* is the effective electron mass, and $V(r)$ is the external potential. For a homogenoues superconductor with $V(r) = 0$, the vector (u_k, v_k) can be written as:

$$\begin{bmatrix} u_k \\ v_k \end{bmatrix} = e^{\imath \vec{k} \cdot \vec{r}} \begin{bmatrix} u \\ v \end{bmatrix}. \tag{1.4}$$

Here u and v given by

$$u^2 = \frac{1}{2}\left(1 + \sqrt{\frac{E^2 - \Delta^2}{E^2}}\right), \tag{1.5}$$

$$v^2 = \frac{1}{2}\left(1 - \sqrt{\frac{E^2 - \Delta^2}{E^2}}\right), \tag{1.6}$$

where the energy eigenvalues for Bogoliubov quasiparticles in the BCS theory are:

$$E = \pm\left[\left(\frac{\hbar^2 k^2}{2m^*} - \mu\right)^2 + \Delta^2\right]^{1/2}. \tag{1.7}$$

In the spectrum (Figure 1.1), we observe two branches, electron-like and hole-like excitations, and a gap opened between them.

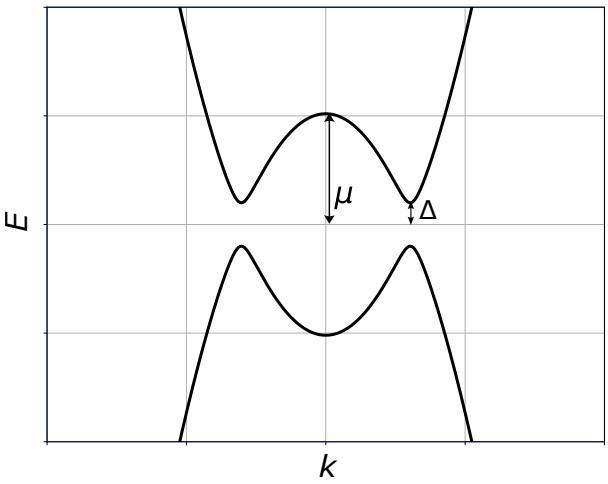

Fig. 1.1 Analytical BdG spectrum $E(k)$ showing electron-like and hole-like branches.

1.3 Josephson junction

1.3.1 DC Josephson effect

After the formulation of the BCS theory, Brian Josephson, a Ph.D. student at Cambridge University, predicted the quantum-mechanical tunneling of pairs of electrons between two different superconductors separated by a thin insulating layer. He predicted that a dissipationless current (supercurrent) would flow, driven by the phase difference between the two superconductors, ϕ

$$I = I_c sin(\phi), \tag{1.8}$$

where I_c is the maximum Josephson current that can flow and is called the critical current of the junction. It is known as the DC Josephson effect and has since been confirmed by numerous experiments [35]. It is now well established that the Josephson effect arises more generally whenever two superconductors are connected by a weak link; this can be not only an insulator but also a metal or a semiconductor. For $I < I_c$ the Josephson current is perfectly dissipationless.

1.3.2 AC Josephson effect

Josephson further predicted that if a constant voltage V_b is applied across the junction, the superconducting phase difference evolves as

$$\frac{d\phi}{dt} = \frac{2eV_b}{\hbar}, \tag{1.9}$$

so that $\phi(t) = \phi_0 + \frac{2eV_b}{\hbar}t$. Consequently, the Josephson current becomes an alternating current of amplitude I_c and frequency $\omega = 2eV_b/h$:

$$I(t) = I_c \sin\left(\phi_0 + \frac{2eV_b}{\hbar}t\right), \tag{1.10}$$

an effect known as the AC Josephson effect [35, 36].

1.4 Andreev reflection and Andreev bound states

1.4.1 Andreev reflection

In the case of normal reflection, an electron is reflected as an electron at interfaces with vacuum or insulating materials. However, this behavior changes at a normal–superconductor (NS) interface. When a right-moving electron in the normal region, with energy less than Δ reaches the right NS interface, as shown in Fig. 1.2(a). It cannot enter the superconductor because there are no quasiparticle states available below the energy gap. Instead, the incoming electron is reflected as a hole with reversed spin and wave vector. This process, known as Andreev reflection [37], is accompanied by the injection of a Cooper pair into the superconducting region. To describe a one-dimensional NS interface, we restrict the single-particle Hamiltonian of Eq. 1.3 to the case of 1D and a δ-function barrier at the interface,

$$V(x) = U_0\,\delta(x), \tag{1.11}$$

with strength U_0. It is convenient to parameterize the interface transparency by the dimensionless Blonder–Tinkham–Klapwijk (BTK) barrier strength [38],

$$Z = \frac{U_0}{\hbar v_F}, \qquad v_F = \frac{\hbar k_F}{m^*}, \qquad k_F = \frac{\sqrt{2m^*\mu}}{\hbar}, \tag{1.12}$$

where m^* is the effective electron mass. In the clean limit ($U_0 = 0$), one has $Z = 0$ and the interface is perfectly transparent. On the normal side ($x < 0$), only propagating electron and hole states are retained.

For subgap energies $|E| < \Delta$, the superconducting side ($x > 0$) does not support propagating quasiparticles; instead, the Bogoliubov–de Gennes solutions have complex momenta corre-

sponding to evanescent modes that decay over the superconducting coherence length. Transport in this regime therefore occurs entirely through reflection at the interface.

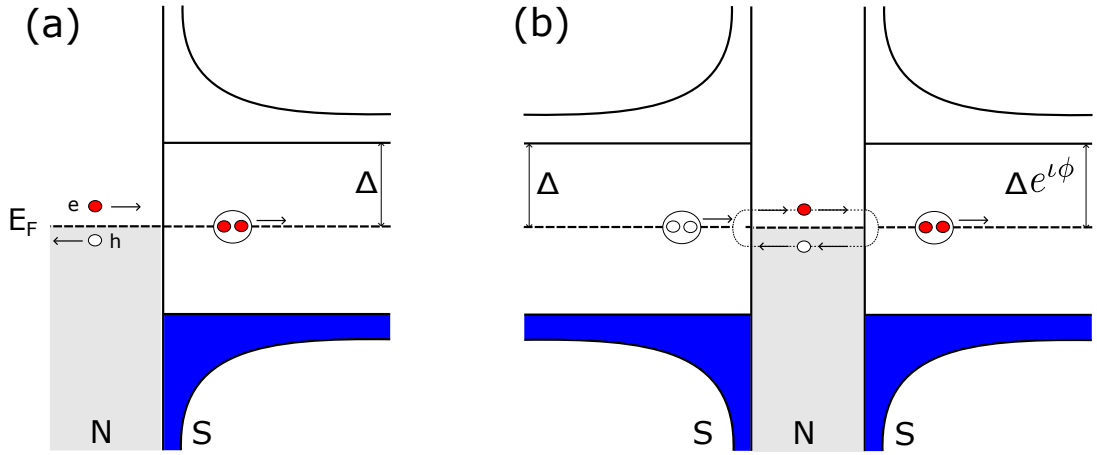

Fig. 1.2 A schematic illustration of Andreev reflection is shown. At the NS interface, an incoming electron is reflected as a hole (retro-reflected), while a Cooper pair is transmitted into the superconductor, as shown in Figure (a). Figure (b) represents a S–N–S junction; the reflected hole reaching the left interface undergoes another Andreev reflection.

In the normal region, the scattering state for an electron incident from the left is written as

$$\psi_N(x) = \begin{bmatrix} 1 \\ 0 \end{bmatrix} e^{\iota k_e x} + b \begin{bmatrix} 1 \\ 0 \end{bmatrix} e^{-\iota k_e x} + a \begin{bmatrix} 0 \\ 1 \end{bmatrix} e^{\iota k_h x}, \tag{1.13}$$

where a and b are reflection coefficients. The electron and hole wavevectors are

$$k_e = \frac{\sqrt{2m^*(\mu + E)}}{\hbar}, \qquad k_h = \frac{\sqrt{2m^*(\mu - E)}}{\hbar}, \tag{1.14}$$

which, in the limit $E \ll \mu$, both approach the Fermi momentum $k_F = \sqrt{2m^*\mu}/\hbar$. In the superconducting region ($x > 0$), the wave function is

$$\psi_S(x) = c \begin{bmatrix} u \\ v \end{bmatrix} e^{\iota q x} + d \begin{bmatrix} v \\ u \end{bmatrix} e^{-\iota q x}, \tag{1.15}$$

where c and d are transmission coefficients, and (u, v) are the BCS coherence factors defined in Eqs. (1.5)–(1.6), normalized such that $|u|^2 + |v|^2 = 1$. For $|E| < \Delta$, the momentum in the superconductor is complex,

$$q = k_F \pm \iota\kappa(E), \qquad \kappa(E) = \frac{\sqrt{\Delta^2 - E^2}}{\hbar v_F}, \tag{1.16}$$

so the solutions describe evanescent quasiparticles. Applying boundary conditions at $x = 0$ yields the scattering amplitudes and allows one to define the corresponding probabilities in the BTK

formalism [38]:

$$A(E) = |a(E)|^2, \qquad B(E) = |b(E)|^2, \qquad C(E) = |c(E)|^2, \qquad D(E) = |d(E)|^2. \tag{1.17}$$

Probability conservation imposes

$$A(E) + B(E) + C(E) + D(E) = 1. \tag{1.18}$$

For subgap energies $|E| < \Delta$, there are no propagating states in the superconductor, implying that

$$C(E) = D(E) = 0, \tag{1.19}$$

and therefore

$$A(E) + B(E) = 1. \tag{1.20}$$

In the clean limit of a perfectly transparent interface ($Z = 0$), the BTK result simplifies to

$$A(E) = 1, \qquad B(E) = 0, \qquad C(E) = D(E) = 0, \qquad |E| < \Delta, \tag{1.21}$$

which corresponds to perfect Andreev reflection: each incident electron is retro-reflected as a hole with unit probability. This confirms that subgap transport occurs entirely through Andreev reflection at an ideal NS interface, providing the microscopic basis for the doubling of conductance compared to the normal state [39–41].

1.4.2 Andreev bound states

Let us attach another superconductor on the left side of the NS junction. This gives rise to an SNS junction composed of a left superconductor with pairing potential Δ and the right superconductor with pairing potential $\Delta e^{\imath\phi}$.

Let us revisit the case of a right-moving electron with energy $|E| < \Delta$. At the NS interface, this electron undergoes Andreev reflection and is converted into a left-moving hole, which results in the addition of a charge $2e$ to the right superconductor. As the hole propagates to the SN interface, it is reflected as a right-moving electron, extracting a charge $2e$ from the left superconductor as shown in Fig. 1.2(b). This entire process leads to the net transfer of a Cooper pair from the left to the right superconductor, and discrete states emerge whose energies depend on the superconducting phase. These states are known as ABSs [42].

The condition for the formation of bound states in one dimension, where the total phase acquired during one cycle is a multiple of 2π, is given by ABS energies [43, 44]:

$$-2\arccos\frac{E(\phi)}{\Delta} \pm \phi + \frac{2E(\phi)}{\Delta}\frac{L_N}{\xi_0} = 2\pi n, \quad n = 0, \pm 1, \ldots \tag{1.22}$$

Where L_N is the length of the normal region, i.e., the distance between the two superconductors, and $\xi_0 = \frac{\hbar v_F}{\Delta}$ is the superconducting coherence length, which defines the two spatial limits of the SNS junctions.

$$L_N \ll \xi_0 \Rightarrow \text{short SNS junction}, \tag{1.23}$$

$$L_N \gg \xi_0 \Rightarrow \text{long SNS junction}. \tag{1.24}$$

In the short junction limit, i.e., $L_N \to 0$, the third term can be neglected, and the two degenerate Andreev levels are given by:

$$E(\phi) = \pm\Delta\cos(\phi/2). \tag{1.25}$$

Here, we have considered ballistic SNS junctions. When the normal region N has a finite transmission τ, the ABS energies are:

$$E(\phi) = \pm\sum_i E_i(\phi) = \pm\sum_i \Delta\sqrt{1-\tau_i\sin^2(\phi/2)}. \tag{1.26}$$

The ground-state energy is obtained by summing over the negative energy Andreev levels, i.e.,

$$E_{\mathrm{GS}}(\phi) = -\sum_i E_i(\phi). \tag{1.27}$$

The power dissipation at the junction, P, is then given by

$$P = \frac{dE_{\mathrm{GS}}(\phi)}{dt} = -\sum_i \frac{\partial E_i(\phi)}{\partial\phi}\frac{d\phi}{dt}. \tag{1.28}$$

From the AC Josephson effect (see Eq. 1.9), we know that $\frac{d\phi}{dt} = \frac{2eV_b}{\hbar}$. Substituting this into the above expression and recognizing that $P = I(\phi)V_b$, we obtain the expression for the persistent current in the ground state, known as the supercurrent $I(\phi)$:

$$I(\phi) = -\frac{2e}{\hbar}\sum_i \frac{\partial E_i(\phi)}{\partial\phi}. \tag{1.29}$$

By substituting Eq. 1.26 in Eq. 1.29, current-phase relation (CPR) can be expressed as,

$$I(\phi) = \frac{e\Delta}{2\hbar}\sum_i \frac{\tau_i\sin(\phi)}{\sqrt{1-\tau_i\sin^2(\phi/2)}} \tag{1.30}$$

From Fig. 1.3(a), we observe that for $\tau < 1$ the spectrum exhibits an avoided crossing at $\phi = \pi$ and the CPR becomes sinusoidal.

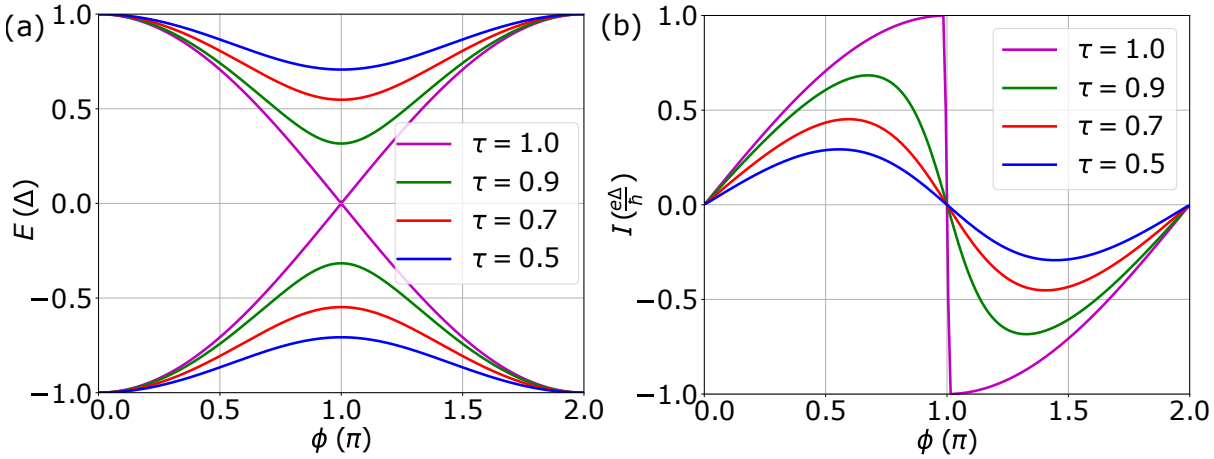

Fig. 1.3 (a) ABS energy levels for a single-channel JJ for different transparencies, (b) represents the corresponding CPR.

In the low transmission limit ($\tau << 1$),[1] the CPR approaches $I = I_c \sin(\phi)$, where $I_c = \frac{e\Delta}{2\hbar} \sum_i \tau_i$, which corresponds to the DC Josephson effect (see Eq. 1.8). This is the case for a Superconductor–Insulator–Superconductor (SIS) junction. In contrast, for the high transmission limit ($\tau = 1$), the equilibrium CPR is

$$I(\phi) = 2I_c \sin\left(\frac{\phi}{2}\right) \mathrm{sgn}\left(\cos\left(\frac{\phi}{2}\right)\right). \tag{1.31}$$

This CPR is 2π-periodic and exhibits a discontinuity at $\phi = (2n+1)\pi$, where $n \in \mathbb{Z}$.

1.5 Majorana-bound states and Majorana zero modes

Ettore Majorana was an exceptional Italian theoretical physicist who mysteriously disappeared in 1938, shortly after completing his groundbreaking work on what are now known as Majorana fermions. The circumstances of his disappearance remain unknown, with rumors ranging from accidental drowning or suicide to retreating into a monastery or starting a secret life in South America. Interestingly, Majorana fermions themselves remain elusive to this day, making both the man and the particles he predicted equally mysterious and intriguing.

Majorana proposed that there could exist neutral fermions described by real solutions to the Dirac equation, particles that are their own antiparticles. Mathematically, this implies that the Majorana operators are Hermitian [45]:

$$\gamma_j^\dagger = \gamma_j, \tag{1.32}$$

The anticommutation relations of Majorana operators satisfy the following relations [45]:

$$\{\gamma_i^a, \gamma_j^b\} = 2\delta_{ij}\delta_{ab}, \quad \gamma_j^{\dagger 2} = \gamma_j^2 \tag{1.33}$$

[1] For plotting the CPR, only negative-energy ABSs are considered.

Any fermionic operator that satisfies the above conditions is a Majorana fermion operator. Here $\gamma_j^a = c_j + c_j^\dagger$, $\gamma_j^b = \imath(c_j^\dagger - c_j)$, that is, the linear combination of fermionic operators.

In condensed matter systems, it is possible to engineer quasiparticle excitations that obey the desired properties of Majorana operators. These emergent excitations behave as their own antiparticles, differ fundamentally from conventional fermions, and are described theoretically within the Majorana formalism. They belong to a class of topological objects known as non-Abelian anyons [46]. Unlike ordinary fermions or bosons, these anyons obey exchange statistics unique to two dimensions, where particle exchanges correspond to braid group operations rather than simple permutations.

Among condensed matter platforms, superconductors provide a natural setting for realizing Majorana-like excitations. Their low-energy excitations, the Bogoliubov quasiparticles, are coherent superpositions of electron and hole states with amplitudes u and v, reflecting the particle-hole symmetry of the superconducting state. In general, the electron and hole contributions (Eq. 1.5) and (Eq. 1.6) are unequal, with the quasiparticle energy given by Eq. 1.7.

To realize a Majorana excitation, one needs to identify a neutral state that is an equal superposition of an electron and a hole. Such an excitation is described by a self-adjoint Majorana operator, which creates a mid-gap state, a quasiparticle sitting exactly at zero energy within the superconducting gap. These zero-energy excitations are not purely electrons or holes; rather, they are effectively half of each, giving them an exotic, anyonic character. Because condensed matter systems are built from electrons and holes, a single Majorana mode is only half of a fermion; two such modes must combine to form a conventional fermionic state, corresponding to either an occupied or an unoccupied level.

To be classified as a MZM, a Majorana operator γ_j must commute with the system's Hamiltonian; that is,

$$[H, \gamma_j] = 0. \tag{1.34}$$

This condition implies that the corresponding excitation has zero energy. These modes are often found at the edges of topological superconductors or bound to defects [47, 48, 48] and are commonly referred to as MZMs or Majorana-bound states (MBSs).

The realistic behavior of MZMs in superconducting systems deviates from ideal conditions. The commutator between the Hamiltonian H Majorana operator γ_j is approximately given by [49–51]:

$$[H, \gamma_j] \approx e^{-x/\xi}, \tag{1.35}$$

with x denoting the separation between two MBSs and ξ the correlation length associated with H. For infinite separation, that is, $x \approx \infty$, this relation aligns with the ideal condition of Eq. 1.34. One can define the fermion occupation number operator $\hat{N}_j$ in terms of Majorana operators as:

$$\hat{N}_j = c_j^\dagger c_j = \frac{1}{2}\left[1 + \imath \gamma_j^a \gamma_j^b\right]. \tag{1.36}$$

The expectation values of this operator yield:

$$\langle j|c_j^\dagger c_j|j\rangle = \begin{cases} 1, & \text{if } |j\rangle \text{ is occupied,} \\ 0, & \text{if } |j\rangle \text{ is empty,} \end{cases} \tag{1.37}$$

leading to

$$\langle j|2c_j^\dagger c_j - 1|j\rangle = \langle j|\imath\gamma_j^a\gamma_j^b|j\rangle = \begin{cases} 1, & \text{if } |j\rangle \text{ is occupied,} \\ -1, & \text{if } |j\rangle \text{ is empty.} \end{cases} \tag{1.38}$$

Since $\hat{N}_j$ does not commute with H in superconducting systems, the number-parity operator is defined as [52–54]:

$$P = (-1)^{\hat{N}} = -\imath\gamma_j^a\gamma_j^b. \tag{1.39}$$

It obeys $\{\gamma_j, P\} = 0$ for the Majorana operators, while $[H, P] = 0$, holds for the Hamiltonian. Consequently, the expectation value determines the parity [55]:

$$\langle j|-\imath\gamma_j^a\gamma_j^b|j\rangle = \begin{cases} -1, & \text{if } |j\rangle \text{ is occupied (odd parity),} \\ 1, & \text{if } |j\rangle \text{ is empty (even parity).} \end{cases} \tag{1.40}$$

This allows the eigenstates of H to be classified into even and odd parity states [56]. Superconductors that host midgap MZMs are referred to as topological superconductors. Spinless p-wave superconductors are theoretically ideal hosts for MZMs, while in two dimensions it has not been observed in nature. To address this, researchers proposed an alternative using conventional s-wave superconductors, which are readily available. In this approach, a one-dimensional semiconducting nanowire with strong spin–orbit coupling is placed in proximity to an s-wave superconductor, and a magnetic field is applied.

1.5.1 Majorana zero modes in nanowires

Let us consider a one-dimensional single-channel nanowire with SOC and Zeeman interaction, whose BdG Hamiltonian is given by: on the basis $\Psi = (\psi_{e\uparrow}, \psi_{h\downarrow}, \psi_{e\downarrow}, -\psi_{h\uparrow})^T$ (where e and h correspond to electron and hole components with spin up $\uparrow$ or down, $\downarrow$, respectively) is

$$H_{BdG} = \left(\frac{\hbar^2\hat{k_x}^2}{2m^*} - \mu\right)\sigma_0\otimes\tau_z + E_z\sigma_z\otimes\tau_0 - \alpha\sigma_y\hat{k_x}\otimes\tau_z + \Delta\sigma_0\otimes\tau_x. \tag{1.41}$$

where $\hat{k_x} = -\imath\partial/\partial x$, $E_z = \frac{1}{2}g\mu_B B$, σ_i and τ_i with $(i = x, y, z)$ are the Pauli matrices that act on the spin and electron-hole degree of freedom, respectively, where σ_0 is (2×2) identity matrix.

Following experimental studies on InSb nanowires with NbTiN superconducting contacts, we model the system using commonly adopted parameters: Landé g-factor $g = 50$, effective mass

$m^* = 0.014\,m_e$, chemical potential $\mu = 3\,\text{meV}$, superconducting gap $\Delta = 1\,\text{meV}$, and spin–orbit coupling strength $\alpha = 40$ meVnm [15, 16]. These parameters are consistent with those reported in experimental studies [17, 57], most notably the pioneering work of [17], where proximity-induced superconductivity was realized in an InSb nanowire device with electrostatic gates, as illustrated in Fig. 1.5.

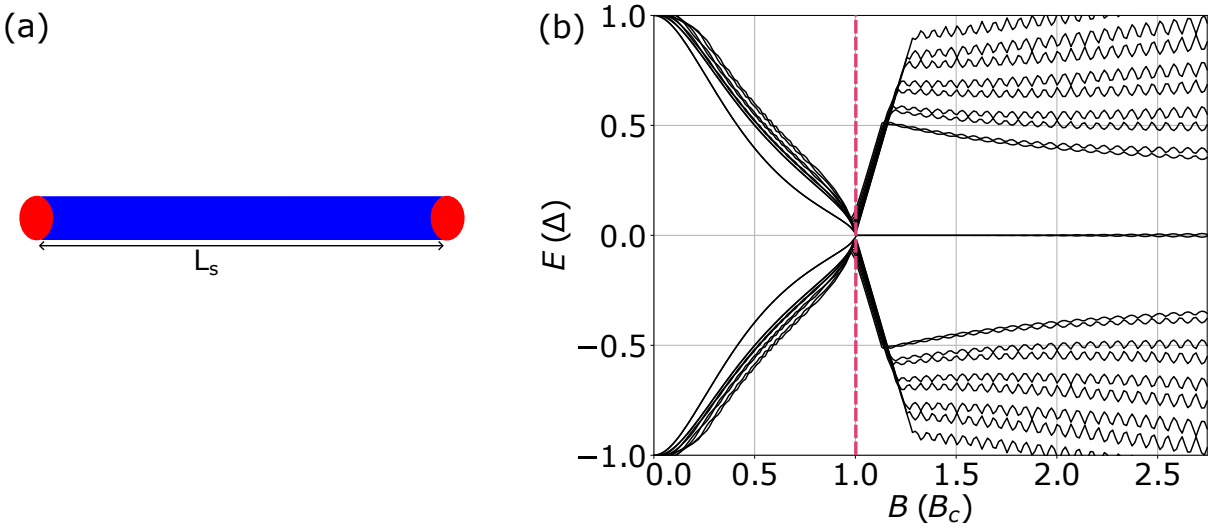

Fig. 1.4 (a) A semiconductor nanowire with Rashba spin–orbit coupling, which in proximity to an *s*-wave superconductor forms MBSs (red filled circles) at its ends. (b) The evolution of the spectrum with magnetic field B, where the vertical red dashed line marks the topological transition point.

When the applied Zeeman field exceeds the critical field, $E_Z > \sqrt{\mu^2 + \Delta^2}$, the system enters the topological phase and MBSs emerge at the two ends of the nanowire.

As shown in Fig. 1.4(b), when the magnetic field reaches the critical value B_c, the superconducting gap closes. For $B > B_c$, zero-energy modes appear that correspond to MBSs localized at the ends of the wire. In this regime, the bulk states shift to higher energies, while the emergence of zero-energy modes indicates a transition into the topological regime.

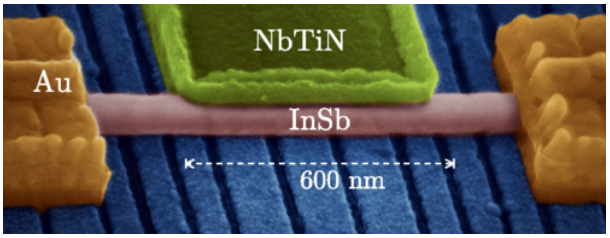

Fig. 1.5 A scanning electron microscope (SEM) image of a device similar to that used in the study by [17] shows an InSb nanowire coupled to a NbTiN superconductor, enabling proximity-induced superconductivity. Gold (Au) electrodes serve as normal-metal Ohmic contacts, allowing measurement of the nanowire's electrical conductance. Image is adapted from [48].

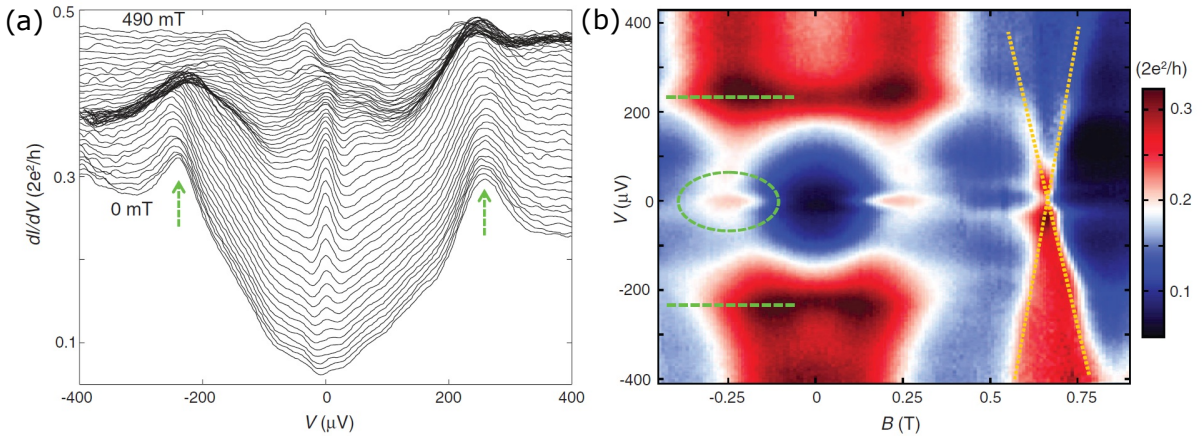

Fig. 1.6 Magnetic field–dependent conductance spectroscopy. (a) Differential conductance (dI/dV) plotted against voltage (V) across different magnetic fields, with traces shifted for clarity except at zero field, indicating induced gap features with arrows. (b) Color-scale map of dI/dV versus V and magnetic field, emphasizing a ZBP with a dashed oval and gap boundaries with green dashed lines, while a non-Majorana state crosses zero bias near $0.6T$, marked by sloped yellow dotted lines. The data in (a) is derived from (b). This figure is adapted from [17].

The presence of MBSs at the ends of a superconducting wire was investigated experimentally by measuring the differential conductance dI/dV across a weak tunnel junction formed between the normal and superconducting regions. This conductance reflects the local density of states.

Upon increasing the magnetic field, a pronounced ZBP appeared between 100 mT ≤ B ≤ 400 mT, as shown in Fig. 1.6(a), suggesting the emergence of MBSs, but disappeared at higher field strengths. However, key theoretical signatures were missing: the ZBP height was significantly lower than expected $\frac{2e^2}{h}$ (only approximately $0.05 \times \frac{2e^2}{h}$), and no clear evidence of the superconducting gap closing and reopening was observed, creating some doubt on the identification of MBSs.

Following this, several independent research groups confirmed similar ZBP in nanowires in non-zero magnetic fields, further strengthening evidence for MZMs [58–60]. However, these experiments also revealed challenges: ZBPs can be mimicked by other effects, such as Kondo physics [61, 62] disorder [63, 64] in the nanowire, smooth confinement [65, 66] or parity crossings of Andreev levels [67], making it difficult to confirm the true nature of the observed ZBP. However, for robust and controllable MZM formation, it is still desirable for the semiconductor to be nearly defect-free, exhibit strong spin-orbit coupling and a large effective g factor, and allow the semiconductor-superconductor interface to remain as clean as possible.

1.5.2 Majorana zero modes in a Josephson junction

In recent years, JJs incorporating 2DEG heterostructures have emerged as a promising alternative platform for realizing MZMs and topological superconductivity [18, 19]. The phase difference ϕ between superconductors acts as an additional tuning parameter to access the topological

regime. In contrast to nanowire-based systems, which require relatively high magnetic fields [15, 16] to reach the topological phase, JJs allow this transition at significantly lower fields. This not only enhances experimental control but also helps maintain the superconducting state. Figure 1.7(a) illustrates a schematic of a device in which a 2DEG exhibiting Rashba SOC is coupled to a pair of s-wave superconductors. These superconductors possess a phase difference denoted by ϕ and an external magnetic field B is applied along the x axis.

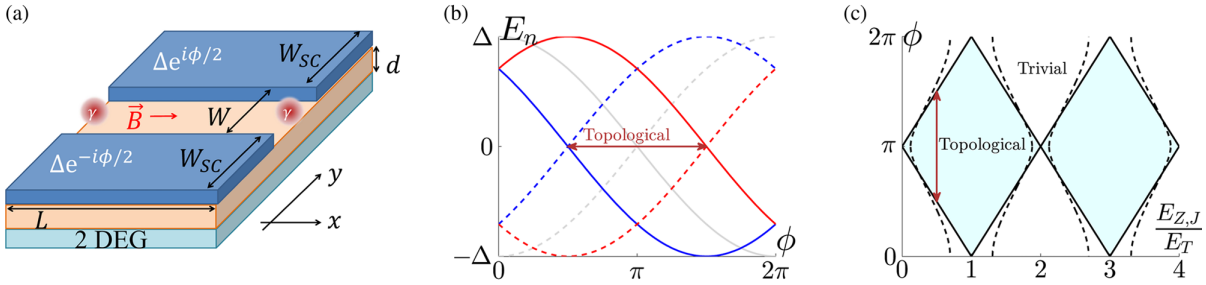

Fig. 1.7 (a) A JJ is created in a 2DEG with Rashba spin–orbit coupling by coupling it to two s-wave superconductors with a phase difference ϕ, and with an in-plane magnetic field applied along the interface. (b) At $k_x = 0$, the bound-state spectrum is spin-degenerate without a Zeeman field (gray), but splits into distinct spin states (red, blue) under the field, enabling a topological phase. (c) The phase diagram shows topological and trivial regions as a function of the Zeeman energy $E_{Z,J}$ and phase difference ϕ, with solid and dashed lines representing different junction transparencies. This figure is adapted from [19].

The BdG Hamiltonian describing this planar JJ is given by:

$$H_{\text{BdG}} = \left(\frac{\hbar^2 (k_x^2 - \partial_y^2)}{2m^*} + \frac{m^* \alpha^2}{2\hbar^2} \tau_z - \mu \right) \tau_z + \alpha \left(k_x \sigma_y + \imath \partial_y \sigma_x \right) \tau_z + E_Z(y) \sigma_x + \Delta(y) \tau_+ + \Delta^*(y) \tau_-, \tag{1.42}$$

where a position-dependent Zeeman energy $E_Z(y)$ is applied only in the normal (non-superconducting) region, such that:

$$E_Z(y) = E_{Z,J} = \frac{1}{2} g \mu_B B. \tag{1.43}$$

The superconducting-order parameter in the junction is modeled as:

$$\Delta(y) = \Delta e^{\imath\, (\text{sgn}(y)) \frac{\phi}{2}} \theta(|y| - W/2), \tag{1.44}$$

where ϕ is the superconducting phase difference and θ is the Heaviside function.

The spin and particle-hole Pauli matrices are denoted by σ and τ, respectively, and $\tau_\pm = (\tau_x \pm \imath \tau_y)/2$. The topological nature of the junction is determined by the ground state parity of the BdG Hamiltonian at $k_x = 0$.

At $k_x = 0$, the Rashba spin-orbit coupling can be gauged away because the SOC and Zeeman field both point along the x direction. The effective Hamiltonian simplifies to:

$$H_{\text{eff}} = \left(-\frac{\hbar^2 \partial_y^2}{2m^*} - \mu \right) \tau_z + E_{Z,J}(y) \sigma_x + \Delta(y) \tau_+ + \Delta^*(y) \tau_-. \tag{1.45}$$

Assuming $\mu \gg \Delta, E_{Z,J}$ and perfect transparency at the interfaces, the spectrum of ABS is [43, 44]:

$$\arccos\left(\frac{E}{\Delta}\right) = \frac{1}{2}\left(\frac{E}{E_{\mathrm{Th}}} - \frac{E_{Z,J}}{E_{\mathrm{Th}}} \pm \frac{\phi}{2}\right) + \pi n, \tag{1.46}$$

where Thouless energy is $E_{\mathrm{Th}} = \hbar v_F / 2W$ [2]. In the absence of a magnetic field, the Andreev levels remain spin degenerate, resulting in even ground state parity for all ϕ. Applying a Zeeman field lifts this degeneracy, and the levels cross zero energy as ϕ is varied. Each crossing corresponds to a change in ground state parity, marking topological phase transitions. The subgap spectrum of H_{eff}, is shown in Fig. 1.7(b).

The boundaries of the topological phase can be obtained by setting the energy $E = 0$ in Eq. 1.46, yielding:

$$\frac{1}{2}\frac{E_{Z,J}}{E_{\mathrm{Th}}} \pm \frac{\phi}{2} = \frac{\pi}{2} + \pi n. \tag{1.47}$$

This condition defines a phase diagram with alternating trivial and topological regions forming a diamond-shaped structure, as shown in Fig. 1.7(c).

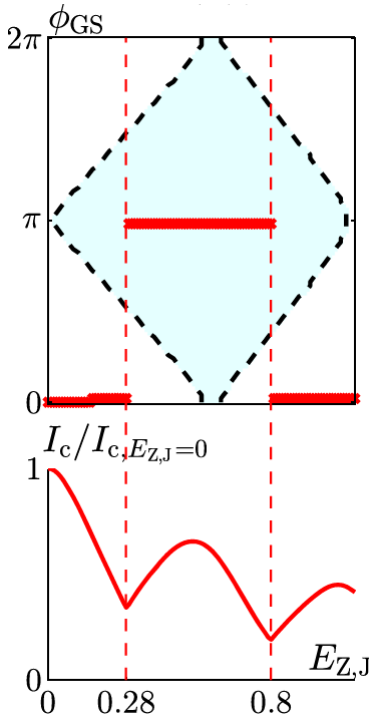

Fig. 1.8 Without external phase control, the system relaxes into the topological regime for certain ranges of the Zeeman field by minimizing its ground-state energy (top panel). The associated 0–π transitions manifest as local minima in the critical current (bottom panel). This figure is taken from [19].

In particular, the system is always in a topological regime at $\phi = \pi$ and remains trivial at $\phi = 0$. As a result, biasing the phase at $\phi = \pi$ allows MBS to emerge at arbitrarily low magnetic fields. This phenomenon is attributed to mirror symmetry, which enforces the degeneracy at

[2] This equation is identical to Eq. 1.22, but with an additional shift of $E_{Z,J}/E_{\mathrm{Th}}$.

$\phi = 0$ and $\phi = \pi$, thus preventing any gap closing and excluding a topological transition at these phase values.

However, this degeneracy holds only under the assumption of perfect Andreev reflection at the NS interface. In realistic scenarios, factors such as low chemical potential, a mismatch in chemical potential between the normal and superconducting regions, or interface imperfections can introduce normal reflection. This reflection couples the left and right moving states, lifting the degeneracy to $\phi = 0$ and $\phi = \pi$, and distorts the ideal diamond structure of the topological phase diagram.

In the configuration where the phase is set by minimizing the ground-state energy, the system can self-tune into the topological phase over a broad range of Zeeman fields, undergoing a first-order topological transition. At the transition points, the minimizing phase ϕ_{GS} abruptly switches between 0 and π, corresponding to trivial and topological regimes, which leads to minima in the critical current (see Fig. 1.8). The critical current can thus serve as a novel experimental probe of topological phase transitions.

In experiments, this superconducting phase difference (ϕ) can be realized by threading a magnetic flux through a loop that connects the two superconductors.

Using tunneling spectroscopy [18] via a quantum point contact (QPC) placed at one end of the junction, as shown in Fig. 1.9, ZBPs can be detected. These ZBPs are phase dependent, appearing prominently when the superconducting phase difference is $\phi \approx \pi$, consistent with theoretical expectations for MZMs. The magnetic field, chemical potential, and phase can be varied to map out the topological regime. Taken together, these measurements demonstrate that phase biasing provides an efficient control knob for accessing and diagnosing the topological phase.

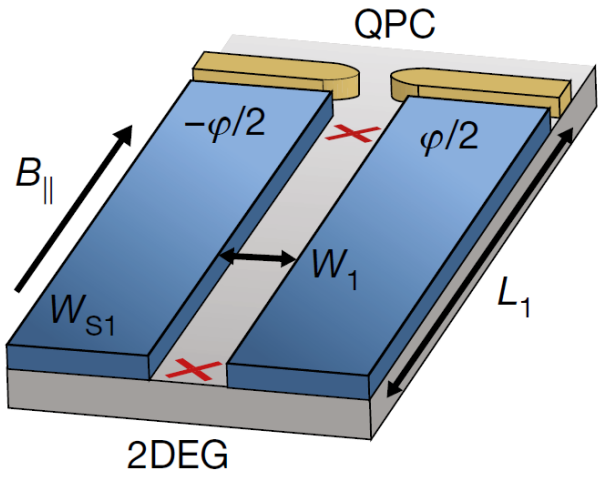

Fig. 1.9 A planar JJ consists of two epitaxial superconductors (blue) on a 2DEG with strong spin–orbit coupling (grey). A 1D channel forms between the leads, where Majorana modes (red crosses) can emerge at its ends by tuning the parallel magnetic field ($B_{\parallel}$), chemical potential (μ), and phase difference (ϕ). A QPC enables tunneling spectroscopy to probe these modes. This figure is adapted from [18].

Chapter 2

Quantum transport

2.1 Eletronic transport

In general, the conductance (G) of a rectangular three-dimensional conductor follows Ohm's law,

$$G = \frac{1}{R} = \frac{1}{\rho}\frac{A}{L} = \frac{\sigma A}{L}, \tag{2.1}$$

where R is the resistance, σ the conductivity, $\rho = 1/\sigma$ the resistivity, L the length of the conductor and A its cross-sectional area. For a two-dimensional conductor of width W and length L, this reduces to

$$G = \frac{\sigma W}{L}. \tag{2.2}$$

Here, σ is a material property that does not depend on the dimensions of the sample.

The natural question then arises: How small can the width W or length L be before Ohm's law breaks down? A conductor exhibits Ohmic behavior as long as its characteristic dimensions are larger than three fundamental length scales: the de Broglie wavelength (set by the kinetic energy of the electrons), the mean free path (the average distance an electron travels before scattering) and the phase relaxation length (distance over which the electron maintains its phase). Conductors with dimensions that fall between the microscopic and macroscopic regimes are referred to as mesoscopic. Such systems are larger than atomic scales but small enough that Ohmic behavior is no longer valid.

2.2 The Landauer-Büttiker formalism

As we move to smaller dimensions, the conductance is no longer governed by the length (L) and width (W), but by the transmission of transverse modes carrying charge through the conductor. In a narrow conductor, these transverse modes arise from quantization of the spectrum perpendicular to transport. Each mode, labeled by N, is characterized by a dispersion relation

$E(N,k)$, with k the longitudinal wave vector along the conductor. The lowest energy of mode N is reached at $k = 0$ and is denoted by [68]

$$\varepsilon_N = E(N, k = 0). \tag{2.3}$$

A single transverse mode does not contribute to transport for energies below ε_N. For a given energy E, the total number of modes that contribute can therefore be written as

$$M(E) = \sum_N \Theta(E - \varepsilon_N), \tag{2.4}$$

where $\Theta(x)$ is the Heaviside step function. For clarity, we begin by considering quantum transport at zero temperature and restrict the analysis to a two-terminal rectangular device. Consider a conductor connected to two large contacts by leads, as shown in Fig. 2.1(a). The transport process can be represented schematically in Fig. 2.1(b): electrons incident from the reservoirs enter the central scattering region, where they are either transmitted with probability $T(E)$ into the opposite lead or reflected back into the injecting reservoir.

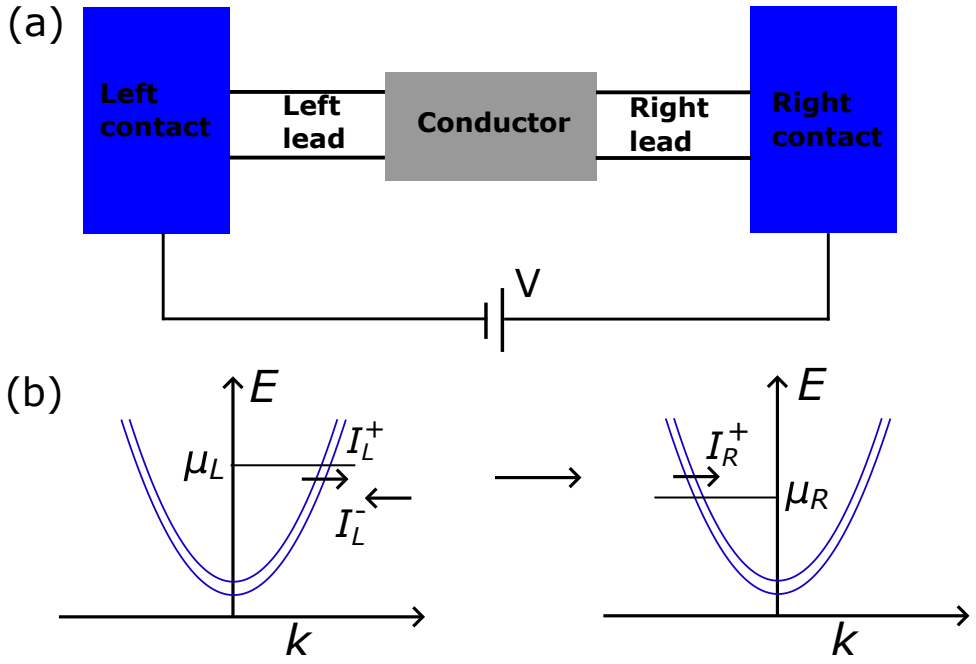

Fig. 2.1 (a) Schematic of a rectangular ballistic conductor, coupled to two large reservoirs through ideal leads. (b) Dispersion relations in the left and right leads, showing electrons propagating from the left reservoir through the conductor into the right reservoir.

We assume that the contacts are ballistic, i.e., charge carriers inside the leads can enter the contacts without any reflection. To calculate the electric current, a potential is applied across the conductor, driving electrons from the left contact to the right contact. As shown in Fig. 2.1(a), the left reservoir has chemical potential μ_L and the right reservoir has chemical potential μ_R, with

$\mu_L > \mu_R$. The states in the leads are filled according to the respective Fermi–Dirac distributions $f_L(E)$ and $f_R(E)$.

To analyze transport, it is useful first to evaluate the current carried by the right-moving states ($+k$) in a single transverse mode and then sum over all modes. If the electron density along the transport direction is n, and the carriers move with group velocity v (i.e., $v = \frac{1}{\hbar}\frac{\partial E}{\partial k}$), the basic relation gives the corresponding current as

$$I = envv. \tag{2.5}$$

Thus we obtain

$$I_L^+ = \frac{e}{L}\sum_k v f_L(E) = \frac{e}{L}\sum_k \frac{1}{\hbar}\frac{\partial E}{\partial k} f_L(E). \tag{2.6}$$

Replacing the sum by an integral over k,

$$\sum_k \longrightarrow 2\frac{L}{2\pi}\int dk, \qquad \text{(factor of 2 accounts for spin degeneracy)}, \tag{2.7}$$

one obtains

$$I_L^+ = \frac{2e}{h}\int_\varepsilon^\infty dE\, f_L(E), \tag{2.8}$$

where ε is the cutoff energy of the mode. Extending this to all available modes leads to

$$I_L^+ = \frac{2e}{h}\int_{-\infty}^\infty dE\, f_L(E) M(E). \tag{2.9}$$

The transmitted current into the right lead is

$$I_R^+ = \frac{2e}{h}\int_{-\infty}^\infty dE\, f_L(E) M(E) T(E). \tag{2.10}$$

The backward-moving current in the left lead arises from electrons injected from the left reservoir that are reflected, together with electrons injected from the right reservoir that are transmitted into the left lead:

$$I_L^- = \frac{2e}{h}\int_{-\infty}^\infty dE\Big[f_L(E) M(E)\,[1 - T(E)] + f_R(E) M(E) T(E)\Big]. \tag{2.11}$$

The net current in the left lead is therefore

$$I_L = I_L^+ - I_L^-. \tag{2.12}$$

Analogously, the current in the right lead can be expressed as

$$I_R = I_R^+ - I_R^-. \tag{2.13}$$

In steady state, the net current flowing through the device is the same in both leads, i.e.,

$$I = I_L = I_R. \tag{2.14}$$

It can be expressed as

$$I = \frac{2e}{h} \int_{-\infty}^{\infty} dE \left[f_L(E) - f_R(E) \right] M(E) T(E). \tag{2.15}$$

At zero temperature, the Fermi–Dirac distributions in the two reservoirs reduce to step functions, equal to 1 for energies below the respective chemical potentials and 0 above:

$$f_L(E) = \begin{cases} 1, & E < \mu_L, \\ 0, & E > \mu_L, \end{cases} \qquad f_R(E) = \begin{cases} 1, & E < \mu_R, \\ 0, & E > \mu_R. \end{cases} \tag{2.16}$$

In this limit, the Landauer current expression simplifies to

$$I = \frac{2e}{h} \int_{\mu_R}^{\mu_L} dE\, M(E) T(E). \tag{2.17}$$

Consequently, only states within the bias window $[\mu_R, \mu_L]$ contribute to transport. For small bias $V = (\mu_L - \mu_R)/e$, both $M(E)$ and $T(E)$ can be taken as constant within this window, yielding

$$I = \frac{2e^2}{h} M T V, \tag{2.18}$$

and the corresponding conductance is the Landauer formula [68],

$$G = \frac{dI}{dV} = \frac{2e^2}{h} M T. \tag{2.19}$$

This is the well-known Landauer equation for quantum conductance, which describes quantum transport properties in a coherent regime. Also, for wide conductors, the number of transverse modes scales as $M \propto W$, while the transmission probability decreases as $T \propto 1/L$. Substituting into the Landauer relation, leading to Eq. (2.2) Ohm's law. The above Eq. (2.19) is closely analogous to the Einstein relation for conductivity:

$$\sigma = e^2 N_S D \iff G = \frac{2e^2}{h} MT, \tag{2.20}$$

where the correspondence is

$$\sigma \Rightarrow G, \qquad N_S \Rightarrow M, \qquad D \Rightarrow T.$$

Here, σ is the electrical conductivity, N_S the density of states, and D the diffusion coefficient. In the Landauer picture, M represents the number of transverse modes and T transmission probability. Thus, the Landauer formula may be regarded as the mesoscopic analog of the Einstein relation.

The Landauer approach was originally introduced to describe the current–voltage characteristics of tunnel junctions in the limit of small transmission probabilities. Over time, it has become the standard theoretical framework for understanding transport in mesoscopic conductors and is often viewed as the mesoscopic analog of Ohm's law.

The Landauer formula provides a transparent description of transport in a two-terminal system, but many experiments employ multiterminal geometries. Büttiker proposed a natural extension by treating each terminal as an ideal voltage probe, so that transport can be formulated entirely in terms of measurable currents and voltages. In this framework, the current entering contact α is

$$I_\alpha = \frac{2e}{h}\sum_\beta \Big[T_{\beta\alpha}\,\mu_\alpha - T_{\alpha\beta}\,\mu_\beta\Big] = \sum_\beta \Big[G_{\beta\alpha}\,U_\alpha - G_{\alpha\beta}\,U_\beta\Big], \tag{2.21}$$

where $T_{\alpha\beta}$ is the total transmission probability from lead β into lead α (summing over all propagating modes), $G_{\alpha\beta} = (2e^2/h)T_{\alpha\beta}$ are the corresponding conductance coefficients, and $U_\alpha = \mu_\alpha/e$ is the voltage at contact α. Current conservation requires the conductance coefficients to satisfy

$$\sum_\alpha G_{\alpha\beta} = 0, \qquad \forall\beta, \tag{2.22}$$

which reflects the fact that no net current flows when all contact voltages are equal. With this constraint, the expression simplifies to the compact form

$$I_\alpha = \sum_\beta G_{\alpha\beta}\,(U_\alpha - U_\beta). \tag{2.23}$$

An additional property follows from the time-reversal symmetry of the scattering matrix: the conductance coefficients satisfy the Onsager reciprocity relation

$$G_{\alpha\beta}(B) = G_{\beta\alpha}(-B), \tag{2.24}$$

where B denotes the applied magnetic field. In the absence of magnetic field, the conductance coefficients are symmetric, $G_{\alpha\beta} = G_{\beta\alpha}$. This relation, known as the Büttiker formula, generalizes the Landauer approach to multiterminal systems and provides the theoretical foundation for analyzing four-probe measurements, Hall-bar geometries, and other mesoscopic transport configurations [68–70].

2.2.1 Conductance in terms of the scattering matrix

The scattering matrix acts as a linear map between incoming and outgoing amplitudes [68, 69, 71], treating the conductor as a "black box" [72]. In this approach, the microscopic details of the sample interior do not matter. All the information about how electrons are transmitted or reflected is contained in the elements of the scattering matrix S. This provides a convenient starting point for deriving measurable quantities such as the transmission function T and, ultimately, the conductance.

Formally, this mapping takes the form

$$c^{\text{out}} = S\,c^{\text{in}}. \tag{2.25}$$

Here, c^{in} and c^{out} denote the amplitudes of the incoming and outgoing states, respectively.

Conservation of probability current in a coherent device requires the scattering matrix to be unitary,

$$S^{\dagger}S = \mathbb{I} = SS^{\dagger}, \tag{2.26}$$

where $S^{\dagger}$ is the Hermitian conjugate of S, and $\mathbb{I}$ is the identity matrix. If lead i supports $M_i(E)$ propagating modes, the total number of modes is

$$N(E) = \sum_i M_i(E), \tag{2.27}$$

and therefore S has dimension $N \times N$.

Example: two-terminal case

The two-terminal geometry is illustrated in Fig. 2.1(a), shows the schematic of the device with contacts and leads, and although Fig. 2.1(b) depicts the associated dispersion relations with two modes per lead, for simplicity, we restrict here to the case of a single propagating mode in each lead. In this case, the scattering matrix is reduced to

$$S_{2\times 2} = \begin{pmatrix} r & t' \\ t & r' \end{pmatrix}, \tag{2.28}$$

and therefore

$$\begin{pmatrix} c_{\alpha}^{\text{out}} \\ c_{\beta}^{\text{out}} \end{pmatrix} = S_{2\times 2} \begin{pmatrix} c_{\alpha}^{\text{in}} \\ c_{\beta}^{\text{in}} \end{pmatrix}. \tag{2.29}$$

Here r, r' are reflection amplitudes and t, t' are transmission amplitudes. This compact form already captures all possible scattering events in the two-terminal case.

Multiterminal systems

For systems with several leads, each of which can support multiple propagating modes, it is convenient to label the scattering amplitudes by both the lead index and the mode index. Thus, $c^{\text{in}}_{\beta,m}$ denotes the incoming amplitude in the mode m of lead β, while $c^{\text{out}}_{\alpha,n}$ denotes the outgoing amplitude in the mode n of lead α. The general scattering relation then reads

$$c^{\text{out}}_{\alpha,n}(E) = \sum_{\beta}\sum_{m} S^{nm}_{\alpha\beta}(E)\, c^{\text{in}}_{\beta,m}(E), \tag{2.30}$$

where $S^{nm}_{\alpha\beta}(E)$ is the scattering amplitude for transmission from mode m in lead β into mode n in lead α at energy E. The corresponding transmission probability is

$$T^{nm}_{\alpha\beta}(E) = \left|S^{nm}_{\alpha\beta}(E)\right|^2, \tag{2.31}$$

and the total transmission from lead β to lead α is obtained by summing over modes,

$$T_{\alpha\beta}(E) = \sum_{m\in\beta}\sum_{n\in\alpha} T^{nm}_{\alpha\beta}(E). \tag{2.32}$$

Within the Landauer–Büttiker approach, the conductance matrix is expressed as

$$G_{\alpha\beta}(E) = \frac{2e^2}{h} T_{\alpha\beta}(E) = \frac{2e^2}{h} \sum_{m\in\beta}\sum_{n\in\alpha} \left|S^{nm}_{\alpha\beta}(E)\right|^2. \tag{2.33}$$

In practice, the scattering matrix can be obtained for simple models by solving the Schrödinger equation, or numerically using approaches such as recursive Green's functions or wavefunction matching; comprehensive discussions of these methods and the scattering formalism can be found in Refs. [68, 70]

In summary, the scattering matrix provides the bridge between microscopic scattering processes and macroscopic transport quantities such as conductance.

2.2.2 Landauer–Büttiker approach to NS interfaces

We now extend the scattering formalism to an NS interface. At subgap energies $|E| < \Delta$, transport occurs exclusively by reflection in the normal lead: either normal reflection of an electron (r_{ee}) or Andreev reflection, where an incoming electron is reflected as a hole (r_{he}).

In the Nambu basis (ψ_e, ψ_h), the incoming and outgoing amplitudes are related by

$$\begin{pmatrix} c^{\text{out}}_e(E) \\ c^{\text{out}}_h(E) \end{pmatrix} = \begin{pmatrix} r_{ee}(E) & r_{eh}(E) \\ r_{he}(E) & r_{hh}(E) \end{pmatrix} \begin{pmatrix} c^{\text{in}}_e(E) \\ c^{\text{in}}_h(E) \end{pmatrix}, \tag{2.34}$$

where r_{ee}, r_{hh} describe normal reflection of electrons and holes, and r_{he}, r_{eh} describe Andreev reflection processes. The corresponding reflection probabilities (trace over propagating modes, per spin) are

$$R_{ee}(E) = \mathrm{Tr}\big[r_{ee}(E)\, r_{ee}^{\dagger}(E)\big], \qquad R_{he}(E) = \mathrm{Tr}\big[r_{he}(E)\, r_{he}^{\dagger}(E)\big]. \tag{2.35}$$

Following Tinkham (BTK picture), we assume that each reservoir is in equilibrium, so incoming occupations are Fermi functions shifted by the electrochemical difference $\mu_N - \mu_S = eV$: $f(E - eV)$ for electronlike and $f(E + eV)$ for holelike states, which yields [38]

$$I = \frac{e}{h} \int dE \big[f(E - eV) - f(E + eV)\big]\big[N - R_{ee}(E) + R_{he}(E)\big], \tag{2.36}$$

where N is the number of propagating modes. The linear-response conductance then reads [1]

$$G = \left.\frac{dI}{dV}\right|_{V=0} = \frac{2e^2}{h} \int dE \left(-\frac{\partial f}{\partial E}\right)\big[N - R_{ee}(E) + R_{he}(E)\big]. \tag{2.37}$$

At zero temperature, evaluated at the Fermi energy $E = 0$, this simplifies to

$$G_{NS}(0) = \frac{2e^2}{h}\big[N - R_{ee}(0) + R_{he}(0)\big]. \tag{2.38}$$

In the normal state (no superconductivity), the electron and hole sectors decouple ($r_{he} = 0$). The two-terminal conductance in linear response (at $T = 0$) is

$$G_N = \frac{2e^2}{h} \sum_{n=1}^{N} T_n, \tag{2.39}$$

where T_n are the transmission eigenvalues (eigenvalues of $t\,t^{\dagger}$), and the sum runs over all open modes [71, 73, 74]. *This is the Landauer formula.* In the presence of both spin–orbit coupling and a magnetic field, the twofold degeneracy does not hold; the conductance quantum is reduced to $G_0 = e^2/h$.

[1] Expanding the Fermi functions for small V gives $f(E - eV) - f(E + eV) \approx -2eV\, \partial f/\partial E$, so $dI/dV|_{V=0}$ defines the linear-response conductance. At $T = 0$, $-\partial f/\partial E \to \delta(E)$ and the conductance reduces to its value at the Fermi energy $E = 0$.

Chapter 3

Numerical method

3.1 Numerical quantum transport and the role of KWANT

In condensed matter physics, solving the scattering problem is a general and common task. The scattering problem essentially reduces to determining the scattering matrix, which relates incoming and outgoing modes through transmission and reflection probabilities, as explained in Sec. 2.2.1.

Over the past decades, a variety of numerical methods have been developed to address this problem, each with different strengths and limitations. The recursive Green's function (RGF) method has played a central role in numerical quantum transport. Initially formulated for simple one-dimensional chains [75, 76], the approach was subsequently extended to handle quasi-one-dimensional geometries [77], square-lattice tight-binding models [78], and later more general lattice types and multi-terminal architectures [79–81]. In parallel, significant effort was devoted to improving computational efficiency, leading to refinements such as modular decomposition approaches [82], precalculation of building blocks [83], and optimized slicing techniques for recursive algorithms [84].

Despite these advances, most implementations of RGF remained group-specific codes with limited accessibility. This motivated the development of publicly available software packages for numerical quantum transport. Several alternative approaches have been proposed [85], as the scattering problem also arises in contexts beyond mesoscopic quantum transport.

A more general and flexible approach to simulating arbitrary tight-binding models is provided by KWANT [86]. It is an open-source Python library designed for both efficiency and ease of use. In KWANT, a tight-binding Hamiltonian is built by specifying onsite terms for each site and hopping terms between sites. This is exactly the same way the Hamiltonian is usually written in textbooks, so the code looks very similar to the standard blackboard expression.

Once the system is constructed, it is finalized into a sparse matrix representation of the Hamiltonian, which is then used in transport calculations.

While many introductory examples focus on two-dimensional systems, KWANT itself does not restrict dimensionality and can be applied equally well to one-, two-, or three-dimensional models. This generality, together with its compatibility with widely used Python scientific libraries, has established KWANT as a versatile and widely adopted tool for numerical quantum transport.

Although KWANT was developed primarily for quantum transport calculations, it can also be applied to closed systems, that is, a scattering region without leads. In this case, spectral properties, such as the eigenenergies and eigenfunctions, can be obtained by diagonalizing the Hamiltonian defined in KWANT. Since the wave functions contain information about current flow, one can also analyze local currents inside the system. This demonstrates how KWANT provides a unified framework for investigating closed and open tight-binding systems [86].

3.1.1 Defining the tight-binding system

To describe quantum transport through mesoscopic structures, it is convenient to discretize the system into a lattice. In this framework, the Hamiltonian is expressed as

$$\hat{H} = \sum_{p,q} H_{pq} c_p^\dagger c_q, \tag{3.1}$$

where $c_p^\dagger$ (c_q) creates (annihilates) an electron at the site p (q), and H_{pq} are the Hamiltonian matrix elements. In first quantization, this can be written as

$$\hat{H} = \sum_{p,q} H_{pq} |p\rangle\langle q|, \tag{3.2}$$

with the state $|p\rangle = |\mathbf{r}, \alpha\rangle$ that contains both the lattice coordinate $\mathbf{r}$ and an internal degree of freedom α (e.g. orbital or spin). The diagonal entries H_{pp} correspond to on-site energies, while off-diagonal terms $H_{p\neq q}$ describe hopping between sites.

In quantum transport calculations, the system is defined as a finite scattering region connected to semi-infinite leads. This finite scattering region corresponds to the system under study (often referred to as the device in experimental realizations), while the semi-infinite leads represent ideal reservoirs that provide the propagating modes.

3.1.2 Scattering theory using KWANT

After the lattice Hamiltonian is specified, the subsequent step is the determination of the scattering states. For clarity, we consider a single semi-infinite lead attached to a finite scatterer; although attaching multiple leads is also straightforward. Let H_{sc} denote the Hamiltonian of the scattering region, H_ℓ the Hamiltonian of a single unit cell in the lead, V_ℓ the hopping matrix that connects neighboring lead cells, and V_c the coupling matrix between the scatterer and

the first lead cell. With this notation, the Hamiltonian of the infinite system can be written in block-matrix form as

$$\hat{H} = \begin{pmatrix} \ddots & V_\ell & 0 & 0 \\ V_\ell^\dagger & H_\ell & V_\ell & 0 \\ 0 & V_\ell^\dagger & H_\ell & V_c \\ 0 & 0 & V_c^\dagger & H_{\mathrm{sc}} \end{pmatrix}. \tag{3.3}$$

The total wavefunction may be written as

$$\Psi = (\ldots, \psi_{\ell,2}, \psi_{\ell,1}, \psi_{\mathrm{sc}})^T, \tag{3.4}$$

where $\psi_{\ell,q}$ represents the wave function in the q-th unit cell of the lead and ψ_{sc} denotes the wave function within the scattering region. The translational invariance of the lead Hamiltonian implies that its eigenstates can be written in Bloch form. These modes can be expressed as

$$\phi_n(q) = \lambda_n^q \chi_n, \quad \lambda_n = \exp(\imath k_n a), \tag{3.5}$$

where λ_n and χ_n denote the eigenvalue and the eigenvector of the lead, respectively, with k_n the momentum for the nth channel (or mode) and a the lattice spacing. The classification of the modes falls into three categories: $|\lambda_n| = 1$ correspond to propagating states; those with $|\lambda_n| < 1$ are evanescent (exponentially decaying), while modes with $|\lambda_n| > 1$ are non-normalizable and therefore excluded [1]. Inserting the Bloch form into the Schrödinger equation yields

$$\left(H_\ell + V_\ell \lambda_n^{-1} + V_\ell^\dagger \lambda_n\right)\chi_n = E\,\chi_n. \tag{3.6}$$

And the particle current can be written as

$$< I >= 2\,\mathrm{Im}(\langle \phi_n(q)|V_\ell|\phi_n(q-1)\rangle). \tag{3.7}$$

For transport calculations, the lead modes are required to carry unit current. This is enforced by choosing the normalization of each mode such that the corresponding current fulfills

$$\langle I \rangle = \begin{cases} +1, & \text{incoming modes,} \\ -1, & \text{outgoing modes,} \\ 0, & \text{evanescent modes.} \end{cases} \tag{3.8}$$

Here, "incoming" refers to modes with a group velocity directed *towards* the scatterer, while "outgoing" modes have a group velocity directed *away* from it. Evanescent solutions with $|\lambda_n| < 1$

[1] Writing $k_n = \alpha + \imath\beta$, one finds $\lambda_n = e^{\imath k_n a} = e^{\imath\alpha a} e^{-\beta a}$. For $\beta > 0$, the amplitude decays with distance ($|\lambda_n| < 1$); for $\beta < 0$, it diverges ($|\lambda_n| > 1$), making the state non-normalizable.

carry no net current and therefore do not contribute to transport, although they are essential for boundary matching at the interface.

Scattering matrix from lead-mode expansion

The wave function in lead ℓ associated with an incoming mode n can be written as

$$\psi_n(p) = \phi_n^{\text{in}}(p) + \sum_m S_{mn}\,\phi_m^{\text{out}}(p) + \sum_r \widetilde{S}_{rn}\,\phi_r^{\text{ev}}(p), \tag{3.9}$$

where $\phi_n^{\text{in}}(p)$, $\phi_m^{\text{out}}(p)$, and $\phi_r^{\text{ev}}(p)$ denote, respectively, incoming, outgoing, and evanescent transverse lead modes evaluated on slice p. Here, S_{mn} are the elements of the scattering matrix relating propagating modes, while $\widetilde{S}_{rn}$ are coefficients associated with evanescent modes.

The wave function in the scattering region corresponding to mode n is denoted ϕ_n^{sc}. At the interface between the lead and the scatterer, continuity of the wave function is imposed by matching the wave functions of the scatterer and the lead.

$$\psi_n(0) = \phi_n^{sc}, \tag{3.10}$$

which satisfies the stationary Schrödinger equation

$$\hat{H}\psi_n = E\psi_n, \tag{3.11}$$

where $\hat{H}$ is the block Hamiltonian given in Eq. (3.3). Once the scattering matrix is known, the transport coefficients follow directly. In particular, the two-terminal differential conductance between leads α and β is

$$G_{\alpha\beta} = \frac{e^2}{h} \sum_{n\in\alpha} \sum_{m\in\beta} \left| S_{\alpha\beta}^{nm} \right|^2. \tag{3.12}$$

where n and m label the transverse modes in the leads α and β, respectively. When spin degeneracy is included, Eq. (3.12) reduces to Eq. (2.33) in Sec. (2.2.1). The internal properties of the system can be obtained from the scattering-region wavefunctions. A compact expression is

$$\langle \mathcal{O} \rangle = \frac{1}{2\pi} \sum_n \int dE\, f_n(E)\, \psi_n^{(sc)\dagger}(E)\, \hat{\mathcal{O}}\, \psi_n^{(\text{sc})}(E), \tag{3.13}$$

where $\hat{\mathcal{O}}$ is the operator corresponding to the desired observable (for example, the local density of states or the current density), and $f_n(E)$ is the Fermi–Dirac distribution of the lead for the channel n. This formulation shows how KWANT turns the scattering problem into a numerically tractable task. Using lattice discretization, mode classification, and normalization to unit current, it provides a robust framework for quantum transport in mesoscopic systems [86].

3.1.3 Scattering in a tight-binding chain

To illustrate the tight-binding scattering formalism, consider a simple one-dimensional (1D) chain of atoms. Two semi-infinite leads are attached to a finite region consisting of L sites. The lattice constant is denoted a and is assumed to be uniform throughout the system. One can begin from the continuum Schrödinger equation as

$$-\frac{\hbar^2}{2m}\frac{d^2\psi(x)}{dx^2} + V(x)\psi(x) = E\psi(x). \tag{3.14}$$

To discretize this problem, derivatives are approximated using the central (three-point) finite-difference scheme. In a lattice with spacing a,

$$\left.\frac{d\psi}{dx}\right|_{x=na} \approx \frac{\psi(x+a)-\psi(x-a)}{2a}, \tag{3.15}$$

$$\left.\frac{d^2\psi}{dx^2}\right|_{x=na} \approx \frac{\psi(x+a)-2\psi(x)+\psi(x-a)}{a^2}. \tag{3.16}$$

Substituting into Eq. 3.14 gives the discrete equation

$$(2t+V_n)\psi_n - t\psi_{n-1} - t\psi_{n+1} = E\psi_n. \tag{3.17}$$

This can be written as

$$\sum_m \mathcal{H}_{nm}\psi_n = E\psi_n, \tag{3.18}$$

where $\mathcal{H}_{nm}$ denotes the matrix elements, $\psi_n = \psi(x = na)$, and $V_n = V(x = na)$. The diagonal terms $\mathcal{H}_{nn} = 2t + V_n$ act as on-site energies, while the off-diagonal terms $\mathcal{H}_{n\neq m} = -t$ describe nearest-neighbor hopping with $t = \hbar^2/(2ma^2)$. In higher dimensions the coordination number increases, giving $(4t + V_{i,j})$ on a square lattice (2D) and $(6t + V_{i,j,k})$ on a cubic lattice (3D) [87].

As established above, the eigenstates of the periodic leads take the Bloch form. In the one dimension, Eq. 3.17 admits plane-wave solutions. For the incidence from the left lead ($n \leq 0$), the state is written as a superposition of incoming and reflected waves:

$$\psi_n = e^{\imath kna} + Ae^{-\imath kna}, \tag{3.19}$$

while in the right lead ($n \geq L+1$) it contains only a transmitted component,

$$\psi_n = Be^{\imath kna}. \tag{3.20}$$

The dispersion relation follows as follows.

$$E(k) = -2t\cos(ka), \tag{3.21}$$

with corresponding group velocity;

$$v(k) = \frac{1}{\hbar}\frac{dE}{dk} = \frac{2ta}{\hbar}\sin(ka). \tag{3.22}$$

The transmitted flux [2] is therefore proportional to $|B|^2 v(k)$, which reduces to the continuum result in the long-wavelength limit $ka \to 0$ [3]. The coefficients $|A|^2$ and $|B|^2$ directly represent reflection and transmission probabilities, respectively. This connects the explicit wave-function approach to the general scattering-matrix formalism developed in the previous section.

Within the finite region, the amplitudes $\psi_1, \ldots, \psi_L$ are determined by enforcing continuity at the boundary sites $n = 0, 1, L, L+1$. This results in a system of $L+2$ linear equations for unknowns $\{A, \psi_1, \ldots, \psi_L, B\}$. In compact notation, this is written as

$$M\Psi = b, \tag{3.23}$$

where M is a tridiagonal matrix $(L+2)\times(L+2)$ and b an inhomogeneous vector. Solving this system yields the reflection and transmission amplitudes, together with the scattering-state amplitudes inside the finite region. Explicit forms of the boundary equations are given in Ref. [87]. Repetition of the procedure for the incidence from the right lead yields two additional coefficients. Collecting all four amplitudes defines the 2×2 scattering matrix

$$S = \begin{pmatrix} s_{LL} & s_{LR} \\ s_{RL} & s_{RR} \end{pmatrix}, \tag{3.24}$$

where $s_{\alpha\beta}$ denotes the amplitude of the scattering from lead β to lead α, with $\alpha, \beta \in \{L, R\}$. Thus, s_{LL} and s_{RR} correspond to reflection in the left and right leads, while s_{RL} and s_{LR} represent transmission across the device. Thus, the full scattering matrix that was the central object of the transport problem in this example is obtained, derived here within the wave-function approach.

[2] In the continuum case with dispersion $E(k) = \hbar^2 k^2/(2m)$, the probability current for the transmitted wave is $I = \frac{\hbar k}{m}|B|^2 = |B|^2 v_k$, where $v_k = \frac{1}{\hbar}\frac{dE}{dk}$ is the group velocity.

[3] At $ka \to 0$ (as long as the wave function varies only gradually over the lattice spacing), the Eq. (3.22) reduces to $v(k) = \frac{\hbar k}{m}$

Chapter 4

Summary of Articles

4.1 Controlling Andreev Bound States with the Magnetic Vector Potential

C. M. Moehle, P. K. Rout, N. A. Jainandunsing, D. Kuiri, C. Ting Ke, D. Xiao, C. Thomas, M. J. Manfra, M. P. Nowak, S. Goswami, Nano Lett. 22, 8601 (2022).

Planar JJs have been proposed as a platform for realizing MBSs, whose position and coupling can be tuned by the magnetic vector potential. This vector potential drives counter-propagating currents, generates Josephson vortices, and produces the characteristic Fraunhofer interference pattern in the critical current. A detailed understanding of the ABS spectrum is therefore an essential prerequisite for the realization of MBSs in JJs. Semiconductor–superconductor heterostructures naturally host ABSs, which are coherent superpositions of electron- and hole-like excitations with energies below the superconducting gap. In recent years, such hybrid systems have emerged as versatile platforms for studying and controlling ABSs. In JJs, the ABS spectrum also determines macroscopic properties such as the critical current, which can be tuned via the superconducting phase difference controlled by magnetic flux.

The goal of this work was to investigate how the vector potential influences ABSs in planar JJs. The key experimental observation was that tunneling spectroscopy at the two ends of the junction revealed distinct ABS spectra, with each local probe detecting only part of the spectrum due to coupling to ABSs localized near the respective tunnel barrier. The spectra displayed abrupt phase jumps and opposite shifts of the ABS maxima at the two ends, consistent with a local superconducting phase difference of equal magnitude but opposite sign induced by the magnetic vector potential. In addition, the cusps near the ABS minima develop into sharp jumps, resulting in a highly asymmetric and skewed shape away from zero magnetic field. The skewness is not only reversed for positive and negative fields, but also for the top and bottom ends of the junction. These features demonstrate that each probe is sensitive only to a region of

limited spatial extent in its vicinity, making it difficult to extract bulk junction properties from local spectroscopy alone.

To interpret these findings, we introduce a toy model. The model assumes the presence of localized ABSs at the edges of the junction and demonstrates how the vector potential produces relative phase shifts in their spectra. It therefore explains the observed shifts, skewness reversals, and phase jumps in the tunneling data. To support the toy model, detailed numerical simulations were performed, which not only reproduced the experimentally observed ABS spectra but also confirmed that the tunneling current is dominated by edge-localized ABSs and reproduced the observed phase shifts.

In addition to the ballistic case, we also studied disordered regimes with different mean free paths based on experimental parameters. Unlike the ballistic case, where the spectra at both ends remain closely related, disorder makes the ABS spectra at the top and bottom drastically different due to their sensitivity to the local disorder configuration. Disorder also causes the main resonance to split into multiple, more distinguishable ABSs localized near the ends of the JJ. Their precise position is determined by the local potential landscape, leading to different relative phase shifts that can be observed experimentally near the tunnel probe.

This study makes a significant contribution by elucidating the effects of a spatially varying superconducting phase difference on the ABS spectrum in extended JJs. The results are directly relevant for ongoing efforts to understand and realize topological superconductivity in planar JJs.

4.2 Nonlocal transport signatures of topological superconductivity in a phase-biased planar Josephson junction

D. Kuiri, M. P. Nowak, Phys. Rev. B 108, 205405 (2023).

Zero-bias peaks in tunneling spectroscopy, which were initially considered evidence for MBSs in proximitized nanowires, can also arise from disorder-induced trivial ABSs, leading to false positive results. Planar SNS junctions are regarded as promising platforms for hosting MBSs, with the superconducting phase difference offering an extra knob to control the topological transition. Nonlocal measurements have recently attracted considerable attention. Although both local and nonlocal spectroscopy have been performed on planar SNS junctions in the tunneling regime, they did not exhibit a clear signature of the topological transition.

In this work, we theoretically explored the detection of the topological transition in a planar JJ using nonlocal spectroscopy. The transition, associated with a fermion parity change controlled by the in-plane magnetic field and the superconducting phase difference, is manifested by a change of the sign of the nonlocal conductance at zero energy. This effect originates from a change in the quasi-particle character of the bands and can serve as a clear signature of the topological transition in transport measurements.

At the same time, we highlight an important limitation for realizing the topological phase in SNS junctions: in practical devices where the phase bias is controlled by threading magnetic flux through a superconducting loop embedding the junction. Such loops always have a finite and non-negligible inductance. As a result, the increasing flux through the loop induces superconducting phase slips. Phase slips can prevent continuous access to the full phase space, skipping the most substantial region of phase space required for realizing MZMs. As a result, phase slips strongly hinder the emergence and detection of MBSs at lower magnetic fields.

A significant contribution of this work is to show that, in realistic devices, nonlocal spectroscopy not only provides a tool for identifying topological transitions but also exposes practical challenges for accessing and stabilizing MBSs. This constraint highlights the importance of careful device design, as reducing the loop inductance or suppressing the junction current may help recover access to the required phase space.

4.3 Enhancement of the topological regime in elongated Josephson junctions

D. Kuiri, P. Wójcik, M. P. Nowak, Phys. Rev. B 111, 085416 (2025).

The realization of topological superconductivity in hybrid Josephson junctions has attracted enormous attention due to the possibility of hosting MBSs. The crossover between the trivial and topological regimes can be controlled primarily through two experimentally accessible parameters: the Zeeman interaction strength, adjusted via the magnitude of the in-plane magnetic field, and the superconducting phase difference. The previous nonlocal study has shown that finite loop inductance in flux-biased junctions induces phase slips that skip substantial regions of phase, thereby preventing stable access to the $\phi \equiv \pi$ region where the topological gap forms and MBSs emerge. Consequently, experiments typically require large in-plane magnetic fields to extend the topological phase. Such fields, however, reduce the induced superconducting gap, resulting in the emergence of trivial subgap states, and ultimately suppress superconductivity.

To address this limitation, we demonstrate in this work that the topological region can be significantly extended by elongating the junction rather than by increasing the magnetic field. However, this junction elongation comes with an important drawback: in the normal region, additional transverse modes appear, which close the induced gap and destroy the MBS.

We demonstrate that those unwanted in-gap states can be eliminated by further proximitizing the junction with two additional superconducting contacts, thereby restoring both the topological gap and the Majorana edge modes. Our numerical simulations, supported by an analytical model, reveal that the expansion of the phase interval corresponding to the topological regime scales linearly with the junction length.

Moreover, we show that the topological transition is accessible via critical-current measurements, which additionally reflect the linear decrease of the critical magnetic field required for the transition as the junction length increases.

Chapter 5

Controlling Andreev Bound States with the Magnetic Vector Potential

NANO LETTERS

pubs.acs.org/NanoLett Letter

Controlling Andreev Bound States with the Magnetic Vector Potential

Christian M. Moehle,[▽] Prasanna K. Rout,[▽] Nayan A. Jainandunsing, Dibyendu Kuiri, Chung Ting Ke, Di Xiao, Candice Thomas, Michael J. Manfra, Michał P. Nowak, and Srijit Goswami*

Cite This: *Nano Lett.* 2022, 22, 8601−8607 Read Online

ACCESS | Metrics & More | Article Recommendations | Supporting Information

ABSTRACT: Tunneling spectroscopy measurements are often used to probe the energy spectrum of Andreev bound states (ABSs) in semiconductor-superconductor hybrids. Recently, this spectroscopy technique has been incorporated into planar Josephson junctions (JJs) formed in two-dimensional electron gases, a potential platform to engineer phase-controlled topological superconductivity. Here, we perform ABS spectroscopy at the two ends of planar JJs and study the effects of the magnetic vector potential on the ABS spectrum. We show that the local superconducting phase difference arising from the vector potential is equal in magnitude and opposite in sign at the two ends, in agreement with a model that assumes localized ABSs near the tunnel barriers. Complemented with microscopic simulations, our experiments demonstrate that the local phase difference can be used to estimate the relative position of localized ABSs separated by a few hundred nanometers.

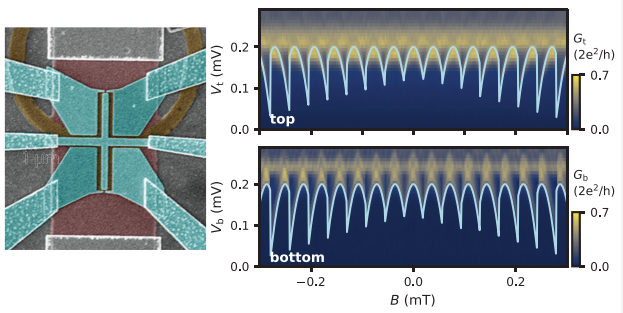

KEYWORDS: *Planar Josephson junctions, Tunneling spectroscopy, Andreev bound states, Local superconducting phase difference*

Hybrid structures composed of superconductors and normal conductors host Andreev bound states (ABSs).[1−3] These states are superpositions of electron-like and hole-like excitations with energies lower than the superconducting gap. In recent years, superconductor−semiconductor hybrids have emerged as an appealing platform to manipulate these bound states. For example, controllable coupling between individual ABSs has led to the creation of Andreev molecules,[4−7] and Josephson junctions (JJs) based on these hybrids have been combined with superconducting circuits to realize Andreev qubits.[8,9] In JJs, the microscopic properties of ABSs determine global properties of the junction, such as its critical current.[2] The energy of ABSs is dependent on the phase difference between the superconducting leads, which can be tuned by the application of a magnetic flux through a superconducting loop connecting the leads. In planar JJs, the vector potential of the magnetic field leads to streams of positive and negative current, to the formation of Josephson vortices, and to the well-known Fraunhofer interference pattern in critical current.[10−12] It has been proposed that such planar JJs can host Majorana bound states,[13−16] and that the location and coupling of these states can be controlled via the vector potential.[17]

In order to investigate how the vector potential modifies ABSs in a JJ, one needs experimental techniques that provide information about the spatial extent and location of ABSs. Studies in junctions that simultaneously probe the spatial distribution and energy spectrum of ABSs have mainly been performed using scanning probe techniques,[18,19] and more recently, via local tunnel probes in two-dimensional electron gases (2DEGs).[20,21]

Here, we perform tunneling spectroscopy at both ends of planar JJs embedded in a superconducting loop, allowing us to probe the effects of the magnetic vector potential on the phase-dependence of the ABS energy. We directly show that the local superconducting phase difference originating from the vector potential has equal magnitude but opposite sign at the two ends of the JJ. This is manifested by a striking difference in the spectroscopy maps obtained from each side, in excellent agreement with a model that assumes tunnel coupling to a single ABS localized at each end. Microscopic numerical simulations confirm that such a localization of the ABSs is indeed expected, and that the tunneling current is only sensitive to ABSs located near the ends of the JJ. By modifying the potential landscape in the vicinity of the tunnel probe, we show that the local phase difference allows us to resolve

Received: August 7, 2022
Revised: October 16, 2022
Published: October 24, 2022

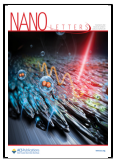

https://doi.org/10.1021/acs.nanolett.2c03130
Nano Lett. 2022, 22, 8601−8607

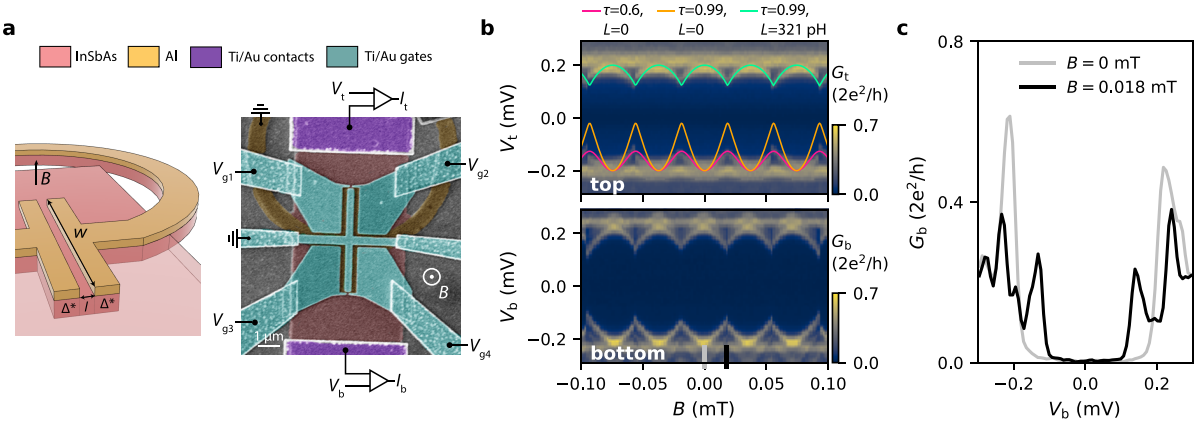

Figure 1. Tunneling spectroscopy at the two ends of a planar phase-biased JJ. (a) Schematic (before the gate deposition) and false-colored SEM of Dev 1. (b) Spectroscopy maps measured at the top (V_{g1} = −0.39 V, V_{g2} = −0.74 V, V_{g3} = 0 V, V_{g4} = 0 V) and bottom end of the JJ (V_{g1} = 0 V, V_{g2} = 0 V, V_{g3} = −1.1 V, V_{g4} = −0.6 V). The three curves in the top panel correspond to single-channel ABS spectra calculated for different combinations of transmission (τ) and loop inductance (L) as specified in the legend. (c) Line cuts of the bottom spectroscopy map at the indicated positions in panel b.

multiple ABSs within a spatial extent of a few hundred nanometers, in qualitative agreement with simulations.

The JJs are fabricated using an $InSb_{0.92}As_{0.08}$ 2DEG with in situ grown Al as the superconductor (details about the molecular beam epitaxy growth of the heterostructure can be found in ref 22). Figure 1a shows a schematic and a false-colored scanning electron micrograph (SEM) of such a device. To fabricate the devices, we first use a combination of Al and 2DEG etches to define the JJ and the superconducting loop. The exposed 2DEG on the top and bottom sides of the JJ is contacted by Ti/Au, and the Al loop is contacted by NbTiN, resulting in a three-terminal device. A globally deposited layer of AlO_x forms the gate dielectric. Lastly, split gates are evaporated on the top and bottom ends of the JJ, allowing us to define tunnel barriers, while also depleting the 2DEG around the junction. A central gate (kept grounded throughout this study) covers the normal section of the JJ. We study two JJs (Dev 1 and Dev 2), both with length l = 80 nm and width w = 5 μm. More details about the device fabrication can be found in the Supporting Information - Section 1 (SI-1). The devices are measured in a dilution refrigerator with a base temperature of 30 mK using standard lock-in techniques.

In Figure 1b (top panel) we present a tunneling spectroscopy map for Dev 1 at the top end of the JJ. The conductance, $G_t = dI_t/dV_t$, is measured as a function of voltage bias, V_t, and perpendicular magnetic field, B. The bottom panel shows the conductance measured at the bottom end, $G_b = dI_b/dV_b$, with representative line cuts presented in Figure 1c. In both maps we see a superconducting gap that is modulated by B, with an oscillation period equal to Φ_0/S, where $\Phi_0 = h/2e$ is the magnetic flux quantum and S is the area of the superconducting loop. This modulation indicates the presence of flux-periodic ABSs in the JJ. For a normal region much shorter than the superconducting coherence length, the relation between the ABS energy and the gauge-invariant phase difference between the two superconducting leads, φ, is given by[2]

$$E_n(\varphi) = \pm\Delta^* \sqrt{1 - \tau_n \sin^2(\varphi/2)} \quad (1)$$

where Δ^* is the induced gap in the 2DEG regions below the Al leads and τ_n is the transmission probability of the nth conduction channel. The flux through the loop, $\Phi = BS$, and φ are related via $\varphi = 2\pi\Phi/\Phi_0$. The relatively small modulation depth observed in the experiment might suggest low-transmission ABSs [see the field evolution of a single ABS with τ = 0.6 (pink) and τ = 0.99 (orange) in Figure 1b]. However, when looking more closely at the energy minima, we find that they display pronounced cusps, not expected from eq 1. These cusps are indicative of phase slips that occur when the superconducting loop has a sizable inductance, L, whereby the standard linear flux-phase relation no longer holds. We independently estimate L = 321 pH (see SI-2) and use the appropriate flux-phase conversion (see SI-6) to find that the measured ABS spectrum is consistent with a large transparency of τ = 0.99 (light green line in Figure 1b). We further confirm this by performing spectroscopy at higher B, as will be discussed later. This highlights the fact that the inductance, which can be significant in thin film superconductors, strongly affects the ABS spectra observed in experiments.

Thus far we have assumed that the superconducting phase difference is constant along the width of the JJ (see Figure 2a for a top-view schematic of the junction). However, the vector potential of the magnetic field creates a phase gradient, $\phi'(y)$, and the total gauge-invariant phase difference is given by $\varphi(y) = \phi + \phi'(y)$, where ϕ is the phase difference that can be tuned by the flux through the loop. The position-dependent local phase difference can be expressed as[10,23]

$$\phi' = -2\pi\frac{fBly}{\Phi_0} \quad (2)$$

where f is a flux focusing factor that increases the effective magnetic flux in the JJ (see SI-3 andRef. 24). This expression for φ is valid for JJs with a width much smaller than the Josephson penetration length, which is the case for our junctions (see SI-4). The magnetic vector potential also leads to the formation of localized ABSs with a well-defined supercurrent direction (see SI-7 for numerical simulations). Figure 2b shows a plot of the expected local phase difference for Dev 1 at B = 1 mT, demonstrating that the phase difference experienced by an ABS located at the top and bottom end of the JJ will be significantly different. Therefore, for localized ABSs (as depicted in Figure 2a), one expects observable differences in the field evolution of their energies. This is more

https://doi.org/10.1021/acs.nanolett.2c03130
Nano Lett. 2022, 22, 8601−8607

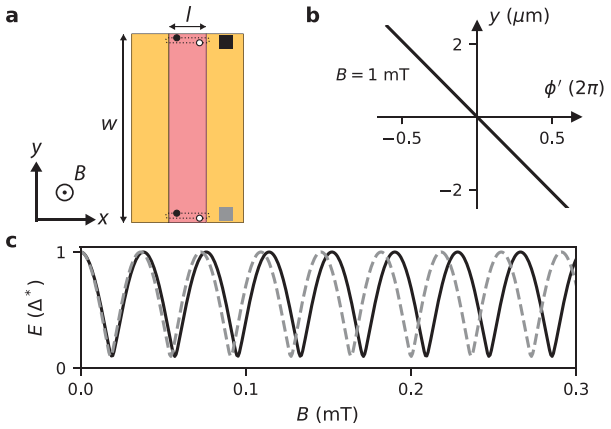

Figure 2. Effect of the magnetic vector potential. (a) Top-view schematic of the JJ in Dev 1. Two ABSs located at the top and bottom end are indicated. (b) Calculated local phase difference arising from the vector potential at $B = 1$ mT ($f = 6.2$). (c) Magnetic field evolution for the ABS located at the top (black) and bottom (gray), showing a relative shift due to the local phase difference.

clearly illustrated in Figure 2c, where we plot the ABS energy, E, as a function of B. As B increases, the maxima for the top and bottom ABS shift relative to each other. This is a direct consequence of eq 2, whereby ABSs located at opposite ends of the JJ are sensitive to the local phase difference with equal magnitude but opposite sign.

With an understanding of the effect of the magnetic vector potential on the ABS spectrum, we now turn to spectroscopy measurements over a significantly larger field range (Figure 3). Figure 3a and b show the top and bottom spectroscopy maps, respectively. We first look at the high field regime (Figure 3a2 and b2), where the ABS oscillation amplitude has increased significantly (compare to 1b). This is caused by the Fraunhofer-like reduction of the critical current, I_c, thereby reducing the so-called screening parameter, $\beta \propto LI_c$. The lower β results in a linear flux-phase relation, making it possible to probe the complete phase-dependence of the ABS (see SI-6 for more details). The fact that the ABS energy reaches very close to zero confirms that the ABSs we are probing have extremely high transparency.

In the intermediate field range (see Figure 3a1 and b1) we find that the cusps near the ABS minima develop into sharp jumps, resulting in a highly asymmetric and skewed shape away from $B = 0$. The skewness is not only reversed for positive and negative fields, but also for the top and bottom end of the JJ. Furthermore, we find that the ABS energy maxima shift in opposite directions in the top and bottom spectroscopy map, as expected for bound states localized at the edges. This is a strong indication that each probe is sensitive only to a region of limited spatial extent in its vicinity, and that it is in general difficult to reliably estimate bulk junction properties from a local spectroscopy measurement.[25]

To explain these findings we introduce a model that takes into account the combined effects of the inductance and vector potential, and assumes that each tunnel probe couples only to a single localized ABS with $\tau = 0.99$ (a full description of the model can be found in SI-6). The resulting ABS spectra are shown as light blue lines plotted on the spectroscopy maps of Figure 3a and b. We find an excellent agreement between the model and the experiments in the entire magnetic field range. We show in SI-6 that the observed reversal of the skewness can only occur when both the vector potential and the loop inductance are taken into account. Therefore, the loop inductance serves as an extremely useful tool to clearly see the effects of a spatially varying phase difference along the JJ.

In order to systematically analyze the difference between the energy spectra of the top and bottom ABS, we introduce the quantity $\Delta B = B_t - B_b$ (see Figure 3c). In Figure 3d, we plot ΔB as a function of B_t for experiment (dark blue circles) and theory (light blue circles). Both show a nonlinear dependence, which can be well accounted for by the variation of I_c (and hence β). It is interesting to note that while our device geometry makes it impossible to directly measure I_c of the JJ, the nodes in the Fraunhofer pattern can still be identified by regions where $\beta \approx 0$ (see arrows), and therefore the experiment/theory plots with finite L approach the theory curve with $L = 0$ (red circles). All of these findings are reproduced in Dev 2 (see spectroscopy maps in SI-5 and the ΔB analysis in Figure 3e).

Although our toy model is effective in capturing the most important features observed in experiments, it relies on the assumption that the tunnel probes couple to a single localized ABS in the vicinity of the barriers. In the following, we use numerical simulations to show that the tunneling current is indeed dominated by edge-located ABSs, and that the phase shifts for these states agree with the experiments. For the simulations, we consider a planar JJ composed of two semi-infinite superconducting leads and a normal region that is connected to two normal leads through tunneling barriers. We calculate the conductance from the top (bottom) normal lead, G_t (G_b), by tracing the quasiparticles entering and leaving the top (bottom) lead. In the simulation, we include the effect of a perpendicular magnetic field and disorder, which results in a finite mean free path, l_e. A superconducting phase difference, ϕ, is imposed between the superconducting terminals (more details about the model can be found in SI-7).

We first consider a ballistic JJ with infinite mean free path. In Figure 4a and b, we show the conductance calculated from the top and bottom, respectively, at $B = 1$ mT. In both maps, the main resonance is shifted by an equal amount in ϕ, but in opposite directions. This shift agrees very well with our toy model (black lines), where we assumed tunnel-coupling to a single ABS localized at the top/bottom end of JJ. The presence of localized ABSs is clearly seen by inspecting the supercurrent distribution calculated at the energy/phase values denoted by the colored circles in Figure 4a. We find that the top probe is only sensitive to the ABSs located in the vicinity of the top barrier (see Figure 4c).

To make a connection with the experiments, we also consider a semiconductor with $l_e = 150$ nm, a good estimate for the mean free path in our 2DEGs.[22] The top and bottom conductances are shown in 4d and e, respectively. As in the ballistic case, we again find a predominant sensitivity to edge-located ABSs, and a relative shift of the ABS maxima. However, we also note two important differences. First, unlike the ballistic case, the ABS spectra at the top and bottom are now drastically different from each other. This is not surprising, given the fact that the ABSs can be sensitive to the particular disorder configuration present at each end. Second, the main resonance splits into more clearly distinguishable ABSs. These ABSs are also localized close to the top/bottom end of JJ, as seen in Figure 4f. The specific location of these states is sensitive to the local potential landscape. However, we expect

https://doi.org/10.1021/acs.nanolett.2c03130
Nano Lett. 2022, 22, 8601−8607

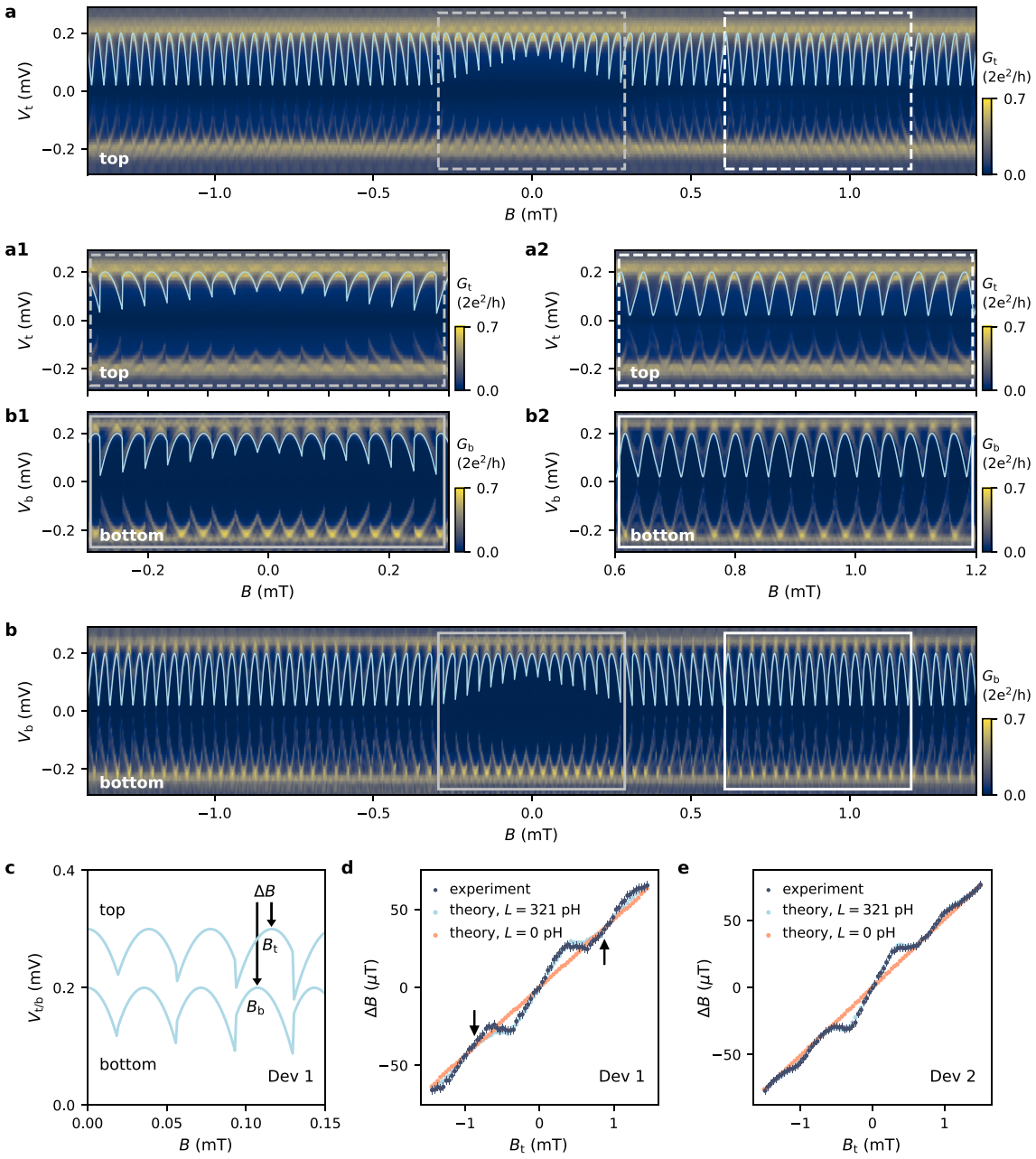

Figure 3. Tunneling spectroscopy over a large magnetic field range. (a) Spectroscopy map at the top end of Dev 1 (V_{g1} = −0.39 V, V_{g2} = −0.74 V, V_{g3} = 0 V, V_{g4} = 0 V), with zoomed-in views presented in panel a1 and a2. (b) Spectroscopy map at the bottom end (V_{g1} = 0 V, V_{g2} = 0 V, V_{g3} = −1.1 V, V_{g4} = −0.6 V) with zoom-in views in panel b1 and b2. The model (light blue lines) assumes coupling to a single ABS (τ = 0.99), taking into account the local phase difference in the JJ and the loop inductance (L = 321 pH). (c) Model curves for the top and bottom end plotted together (offsetted vertically for clarity). The ABS maxima on the top (B_t) and bottom (B_t) are shifted. (d,e) $\Delta B = B_t - B_b$ as a function of B_t for Dev 1 and Dev 2 (dark blue circles). We also include the ΔB values from the toy model with L = 321 pH (light blue circles), and L = 0 (red circles). The arrows indicate the position of the first Fraunhofer node.

them to acquire different relative phase shifts depending on their precise location in the JJ.

This spatially dependent phase shift in the vicinity of the tunnel probe can also be experimentally observed. Figure 5a presents spectroscopy measurements on the top end of Dev 2, where the split gate settings have been modified to locally alter the disorder landscape. At B = 0 (central panel), distinct ABSs are hardly visible (see also black line cut in Figure 5b). However, when increasing the magnetic field (left and right panel), the localized ABSs acquire different phase shifts making it possible to resolve them more clearly (see also gray line cut in Figure 5b). Reversing the field direction leads to ABSs shifted in the opposite direction, as expected for spatially separated ABSs. A similar pattern of ABSs located at different positions close to the edge of the junction and experiencing different phase shifts is obtained in the numerical calculation shown in Figure 5c and d. This demonstrates that the effect of the vector potential (and resulting local phase difference) can indeed be used to estimate the location of the ABSs in the JJ. Around B = 2.09 mT, the maxima of the two states (indicated

https://doi.org/10.1021/acs.nanolett.2c03130
Nano Lett. 2022, 22, 8601−8607

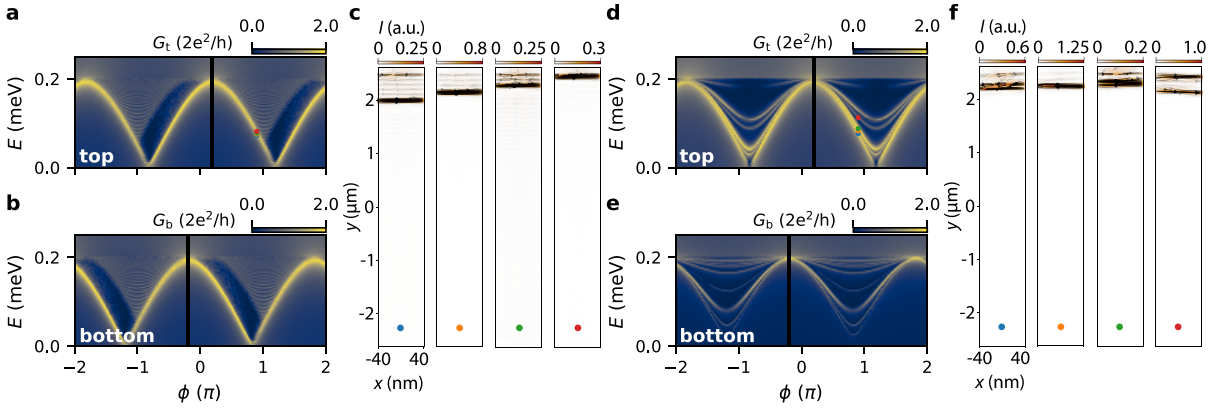

Figure 4. Numerical simulation of the tunneling conductance for a ballistic and disordered JJ. (a,b) Conductance maps at B = 1 mT for a ballistic JJ probed from the top and bottom. The black lines correspond to the phase shifts expected from the toy model. **c** Supercurrent distribution in the normal region of the JJ obtained for the E and ϕ values denoted with the circles in panel a. (d,e) Conductance maps at B = 1 mT for a disordered JJ (l_e = 150 nm) probed from the top and bottom. (f) Supercurrent distributions for the E and ϕ values denoted with the circles in panel d.

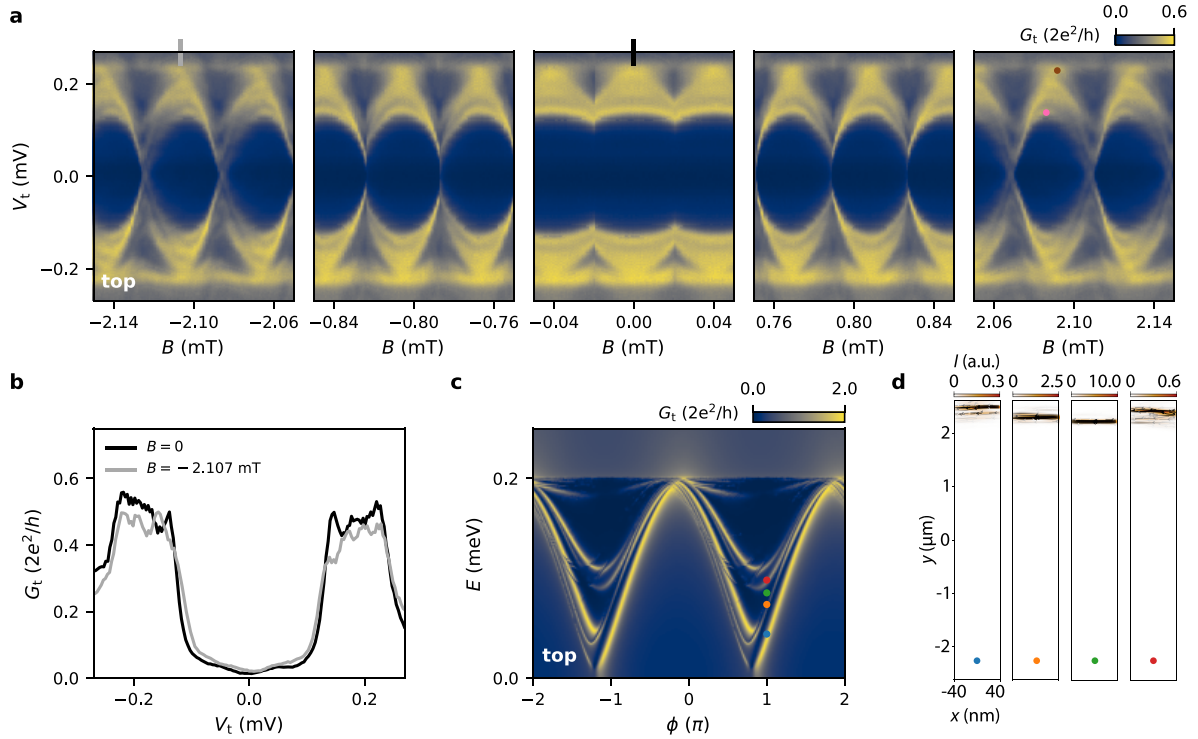

Figure 5. Probing spatially separated ABSs. (a) Tunneling spectroscopy maps at the top end of Dev 2 (V_{g1} = −1.90 V, V_{g2} = −1.40 V, V_{g3} = −2.10 V, V_{g4} = −1.43 V). The ABSs that are initially hardly resolvable around B = 0 are better resolved at larger B, where localized ABSs acquire different phase shifts depending on their location in the JJ. (b) Line cuts at two indicated positions in panel a showing this improvement in resolution. (c) Simulated tunneling conductance map for a disordered JJ (l_e = 150 nm) at B = 10 mT probed from the top. (d) Supercurrent distributions for the E and ϕ values marked by circles in panel c, showing how localized ABSs at different positions correspond to ABS spectra that are shifted in ϕ.

by the brown and pink circles) are shifted by ≈ 5 μT. This shift can be translated into an estimate of their spatial separation by using the spectroscopy results at the two extreme ends of the JJ (Figure S4 and Figure 3e), where we find ΔB = 106 μT at B = 2.09 mT for ABSs separated by 5 μm. Using this, we can estimate the spatial separation of the two states indicated by the brown and pink circles to be approximately 250 nm.

In conclusion, we employed local tunneling spectroscopy at two ends of planar phase-biased JJs to study the influence of the magnetic vector potential on the ABS spectrum. The combined effect of inductance and a spatially varying local phase difference results in striking differences in the tunneling spectra measured at the two edges of these junctions. Supporting our experiments with a theoretical toy model and microscopic numerical simulations, we showed that our results are consistent with the measurement of ABSs localized at the ends of the JJ, in the vicinity of the tunnel barriers. Finally, we showed that the effects of the vector potential are not only observable for ABSs separated by microns, but can also be used to estimate the relative locations of ABSs separated by a few hundred nanometers. Our results provide insights into the effects of a spatially varying phase difference on the ABS

https://doi.org/10.1021/acs.nanolett.2c03130
Nano Lett. 2022, 22, 8601−8607

spectrum in extended JJs, and are relevant for ongoing efforts on investigating topological superconductivity in planar JJs.

Additional Note: During the preparation of this manuscript, we became aware of a related work on tunneling spectroscopy in planar JJs.[26]

■ ASSOCIATED CONTENT

Data Availability Statement

Raw data and analysis scripts for all presented figures are available at the 4TU.ResearchData repository: 10.4121/20059364.

Supporting Information

The Supporting Information is available free of charge at https://pubs.acs.org/doi/10.1021/acs.nanolett.2c03130.

Device fabrication, estimation of loop inductance, flux focusing in planar JJ, tunneling spectroscopy for Dev 2, toy model, microscopic model (PDF)

■ AUTHOR INFORMATION

Corresponding Author

Srijit Goswami − *QuTech and Kavli Institute of Nanoscience, Delft University of Technology, 2600 GA Delft, The Netherlands;* orcid.org/0000-0002-9095-4363; Email: s.goswami@tudelft.nl

Authors

Christian M. Moehle − *QuTech and Kavli Institute of Nanoscience, Delft University of Technology, 2600 GA Delft, The Netherlands;* orcid.org/0000-0002-6094-3663

Prasanna K. Rout − *QuTech and Kavli Institute of Nanoscience, Delft University of Technology, 2600 GA Delft, The Netherlands*

Nayan A. Jainandunsing − *QuTech and Kavli Institute of Nanoscience, Delft University of Technology, 2600 GA Delft, The Netherlands*

Dibyendu Kuiri − *Academic Centre for Materials and Nanotechnology, AGH University of Science and Technology, 30-059 Krakow, Poland*

Chung Ting Ke − *QuTech and Kavli Institute of Nanoscience, Delft University of Technology, 2600 GA Delft, The Netherlands;* Present Address: Institute of Physics, Academia Sinica, Taipei, 11529, Taiwan

Di Xiao − *Department of Physics and Astronomy, Purdue University, West Lafayette, Indiana 47907, United States*

Candice Thomas − *Department of Physics and Astronomy, Purdue University, West Lafayette, Indiana 47907, United States*

Michael J. Manfra − *Department of Physics and Astronomy, Purdue University, West Lafayette, Indiana 47907, United States; Elmore School of Electrical and Computer Engineering and School of Materials Engineering, Purdue University, West Lafayette, Indiana 47907, United States; Microsoft Quantum Lab West Lafayette, West Lafayette, Indiana 47907, United States*

Michał P. Nowak − *Academic Centre for Materials and Nanotechnology, AGH University of Science and Technology, 30-059 Krakow, Poland*

Complete contact information is available at: https://pubs.acs.org/10.1021/acs.nanolett.2c03130

Author Contributions

[▽]C.M.M.and P.K.R. contributed equally to this work.

Author Contributions

C.M.M. and C.T.K. fabricated the devices. C.M.M., P.K.R. and N.A.J. performed the measurements and analyzed the data. S.G. supervised the experimental work. The numerical simulations were performed by D.K. under the supervision of M.P.N. who also provided the toy model. The semiconductor heterostructure was grown by D.X. and C.T. under the supervision of M.J.M. The manuscript was written by C.M.M., P.K.R., D.K., M.P.N. and S.G. with input from all authors.

Notes

The authors declare no competing financial interest.

■ ACKNOWLEDGMENTS

We thank T. Dvir, G. Wang and C. Prosko for fruitful discussions. The research at Delft was supported by the Dutch National Science Foundation (NWO), the Early Research Programme of The Netherlands Organisation for Applied Scientific Research (TNO) and a TKI grant of the Dutch Topsectoren Program. The work at Purdue was funded by Microsoft Quantum. The research at Krakow was supported by National Science Centre (NCN) agreement number UMO-2020/38/E/ST3/00418.

■ REFERENCES

(1) Kulik, I. O. Macroscopic quantization and the proximity effect in SNS junctions. *Sov. Phys. JETP* **1969**, *30*, 944.

(2) Beenakker, C. W. J. Universal limit of critical-current fluctuations in mesoscopic Josephson junctions. *Phys. Rev. Lett.* **1991**, *67*, 3836−3839.

(3) Wendin, G.; Shumeiko, V. S. Josephson transport in complex mesoscopic structures. *Superlattices Microstruct.* **1996**, *20*, 569−573.

(4) Su, Z.; Tacla, A. B.; Hocevar, M.; Car, D.; Plissard, S. R.; Bakkers, E. P.; Daley, A. J.; Pekker, D.; Frolov, S. M. Andreev molecules in semiconductor nanowire double quantum dots. *Nat. Commun.* **2017**, *8*, 1−6.

(5) Pillet, J.-D.; Benzoni, V.; Griesmar, J.; Smirr, J.-L.; Girit, Ç. Ö. Nonlocal Josephson effect in Andreev molecules. *Nano Lett.* **2019**, *19*, 7138−7143.

(6) Kürtössy, O.; Scherübl, Z.; Fülöp, G.; Lukács, I. E.; Kanne, T.; Nygård, J.; Makk, P.; Csonka, S. Andreev molecule in parallel InAs nanowires. *Nano Lett.* **2021**, *21*, 7929−7937.

(7) Jünger, C.; Lehmann, S.; Dick, K. A.; Thelander, C.; Schönenberger, C.; Baumgartner, A.Intermediate states in Andreev bound state fusion. 2021; https://arxiv.org/abs/2111.00651, (accessed July 13, 2022).

(8) Hays, M.; de Lange, G.; Serniak, K.; van Woerkom, D. J.; Bouman, D.; Krogstrup, P.; Nygård, J.; Geresdi, A.; Devoret, M. H. Direct Microwave Measurement of Andreev-Bound-State Dynamics in a Semiconductor-Nanowire Josephson Junction. *Phys. Rev. Lett.* **2018**, *121*, 047001.

(9) Hays, M.; Fatemi, V.; Bouman, D.; Cerrillo, J.; Diamond, S.; Serniak, K.; Connolly, T.; Krogstrup, P.; Nygard, J.; Levy Yeyati, A.; Geresdi, A.; Devoret, M. H. Coherent manipulation of an Andreev spin qubit. *Science* **2021**, *373*, 430−433.

(10) Tinkham, M.*Introduction to Superconductivity*, 2nd ed.; Dover Publications, 1996; pp 215−220.

(11) Cuevas, J. C.; Bergeret, F. S. Magnetic Interference Patterns and Vortices in Diffusive SNS Junctions. *Phys. Rev. Lett.* **2007**, *99*, 217002.

(12) Kaperek, K.; Heun, S.; Carrega, M.; Wójcik, P.; Nowak, M. P. Theory of scanning gate microscopy imaging of the supercurrent distribution in a planar Josephson junction. *Phys. Rev. B* **2022**, *106*, 035432.

(13) Hell, M.; Leijnse, M.; Flensberg, K. Two-Dimensional Platform for Networks of Majorana Bound States. *Phys. Rev. Lett.* **2017**, *118*, 107701.

(14) Pientka, F.; Keselman, A.; Berg, E.; Yacoby, A.; Stern, A.; Halperin, B. I. Topological Superconductivity in a Planar Josephson Junction. *Phys. Rev. X* **2017**, *7*, 021032.
(15) Ren, H.; Pientka, F.; Hart, S.; Pierce, A. T.; Kosowsky, M.; Lunczer, L.; Schlereth, R.; Scharf, B.; Hankiewicz, E. M.; Molenkamp, L. W.; Halperin, B. I.; Yacoby, A. Topological superconductivity in a phase-controlled Josephson junction. *Nature* **2019**, *569*, 93−98.
(16) Fornieri, A.; et al. Evidence of topological superconductivity in planar Josephson junctions. *Nature* **2019**, *569*, 89−92.
(17) Stern, A.; Berg, E. Fractional Josephson Vortices and Braiding of Majorana Zero Modes in Planar Superconductor-Semiconductor Heterostructures. *Phys. Rev. Lett.* **2019**, *122*, 107701.
(18) le Sueur, H.; Joyez, P.; Pothier, H.; Urbina, C.; Esteve, D. Phase Controlled Superconducting Proximity Effect Probed by Tunneling Spectroscopy. *Phys. Rev. Lett.* **2008**, *100*, 197002.
(19) Roditchev, D.; Brun, C.; Serrier-Garcia, L.; Cuevas, J. C.; Bessa, V. H. L.; Milošević, M. V.; Debontridder, F.; Stolyarov, V.; Cren, T. Direct observation of Josephson vortex cores. *Nat. Phys.* **2015**, *11*, 332−337.
(20) Banerjee, A.; Lesser, O.; Rahman, M. A.; Wang, H. R.; Li, M. R.; Kringhøj, A.; Whiticar, A. M.; Drachmann, A. C. C.; Thomas, C.; Wang, T.; Manfra, M. J.; Berg, E.; Oreg, Y.; Stern, A.; Marcus, C. M.Signatures of a topological phase transition in a planar Josephson junction. 2022; https://arxiv.org/abs/2201.03453, (accessed July 13, 2022).
(21) Banerjee, A.; Lesser, O.; Rahman, M. A.; Thomas, C.; Wang, T.; Manfra, M. J.; Berg, E.; Oreg, Y.; Stern, A.; Marcus, C. M.Local and Nonlocal Transport Spectroscopy in Planar Josephson Junctions. 2022; https://arxiv.org/abs/2205.09419, (accessed July 13, 2022).
(22) Moehle, C. M.; Ke, C. T.; Wang, Q.; Thomas, C.; Xiao, D.; Karwal, S.; Lodari, M.; van de Kerkhof, V.; Termaat, R.; Gardner, G. C.; Scappucci, G.; Manfra, M. J.; Goswami, S. InSbAs Two-Dimensional Electron Gases as a Platform for Topological Superconductivity. *Nano Lett.* **2021**, *21*, 9990−9996.
(23) Newrock, R.; Lobb, C.; Geigenmuller, U.; Octavio, M. The two-dimensional physics of Josephson junction arrays. *Solid State Physics* **2000**, *54*, 263−512.
(24) Suominen, H. J.; Danon, J.; Kjaergaard, M.; Flensberg, K.; Shabani, J.; Palmstrøm, C. J.; Nichele, F.; Marcus, C. M. Anomalous Fraunhofer interference in epitaxial superconductor-semiconductor Josephson junctions. *Phys. Rev. B* **2017**, *95*, 035307.
(25) Nichele, F.; Portolés, E.; Fornieri, A.; Whiticar, A. M.; Drachmann, A. C. C.; Gronin, S.; Wang, T.; Gardner, G. C.; Thomas, C.; Hatke, A. T.; Manfra, M. J.; Marcus, C. M. Relating Andreev Bound States and Supercurrents in Hybrid Josephson Junctions. *Phys. Rev. Lett.* **2020**, *124*, 226801.
(26) Banerjee, A.; Geier, M.; Rahman, M. A.; Sanchez, D. S.; Thomas, C.; Wang, T.; Manfra, M. J.; Flensberg, K.; Marcus, C. M.Control of Andreev bound states using superconducting phase texture. 2022; https://arxiv.org/abs/2205.15690, (accessed July 13, 2022).

https://doi.org/10.1021/acs.nanolett.2c03130
Nano Lett. 2022, 22, 8601−8607

Supplementary Information for: Controlling Andreev bound states with the magnetic vector potential

Christian M. Moehle,[1,*] Prasanna K. Rout,[1,*] Nayan A. Jainandunsing,[1]
Dibyendu Kuiri,[2] Chung Ting Ke,[1,†] Di Xiao,[3] Candice Thomas,[3]
Michael J. Manfra,[3,4,5,6] Michał P. Nowak,[2] and Srijit Goswami[1]

[1]*QuTech and Kavli Institute of Nanoscience, Delft University of Technology, 2600 GA Delft, The Netherlands*

[2]*AGH University of Science and Technology, Academic Centre for Materials and Nanotechnology, 30-059 Krakow, Poland*

[3]*Department of Physics and Astronomy, Purdue University, West Lafayette, Indiana 47907, USA*

[4]*Elmore School of Electrical and Computer Engineering, Purdue University, West Lafayette, Indiana 47907, USA*

[5]*School of Materials Engineering, Purdue University, West Lafayette, Indiana 47907, USA*

[6]*Microsoft Quantum Lab West Lafayette, West Lafayette, Indiana 47907, USA*

1. DEVICE FABRICATION

The two phase-biased JJs (Dev 1, Dev 2) and the DC SQUID are fabricated using electron beam lithography. Due to a possible intermixing of Al and Sb we perform all fabrication steps at room temperature unless stated otherwise. The device fabrication starts by etching the Al and the 2DEG in unwanted areas. The Al etch is performed in Transene D etchant at a temperature of 48.2 °C for 9 s resulting a etching thickness of 100 nm. Afterwards, using the same PMMA mask, the 2DEG is etched in a solution of 560 ml deionized water, 9.6 g citric acid powder, 5 ml H_2O_2 and 4 ml H_3PO_4, using an etching time of 90 s. To define the JJs, we perform a second Al etch, carried out in 38.2 °C Transene D for 16 s. This is followed by sputtering a 60 nm thick layer of SiN_x that partly covers the superconducting loop, isolating it from the intended 2DEG contact inside the loop. Next, we contact the exposed 2DEG region on the top and bottom side of the JJ by Ti/Au. Prior to the evaporation of 10 nm Ti and 190 nm Au, a gentle Ar etching is performed in the loadlock of the evaporator to remove any oxides that might have formed on the 2DEG. Afterwards, we contact the superconducting loop by sputtering 150 nm of NbTiN (before the sputter process an in-situ Ar etch is performed to remove the oxide on the Al). As the gate dielectric, we deposit a global layer (40 nm thick) of AlO_x by atomic layer deposition at 40 °C. The gates are formed in two steps: First, the fine structures (split gates and central gate) are deposited by evaporating 10 nm of Ti and 40 nm of Au. In the second step, 10 nm Ti and 100 nm Au are evaporated to define the gate leads.

A schematic and false-colored SEM of Dev 1 is shown in Fig. 1a of the main text. In Fig. S1a we present a SEM of Dev 2, which is similar to Dev 1. The main difference is that the normal region of the JJ is slightly zigzag-shaped ($z_x = 0.24\,\mu$m, $z_y = 1.43\,\mu$m). This was originally introduced into this device to potentially suppress long quasiparticle trajectories and thereby increase the size of the topological gap [1]. The superconducting leads of Dev 1 and Dev 2 have a length of 500 nm. Figure S1b shows a SEM of the DC SQUID, consisting of two JJs (device JJ and reference JJ) in the superconducting loop. The device JJ has a superconducting lead length of 300 nm. Two additional gates are deposited, one covering the normal region of the reference JJ and one covering the 2DEG region around this junction

* These authors contributed equally to this work.

† Present Address: Institute of Physics, Academia Sinica, Taipei, 11529, Taiwan

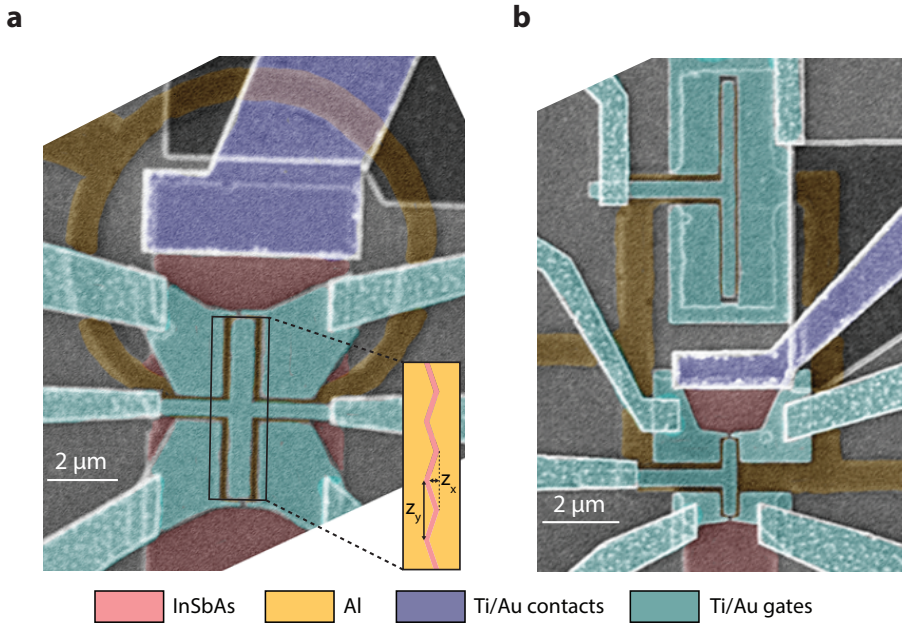

FIG. S1. **a** SEM of Dev 2 having a zigzag-shaped normal region ($z_x = 0.24\,\mu$m, $z_y = 1.43\,\mu$m) with a length of $l = 80\,$nm and width of $w = 5\,\mu$m. **b** SEM of the DC SQUID. The device JJ (on the bottom) has dimensions $l = 120\,$nm and $w = 2\,\mu$m. The reference JJ (on the top) has dimensions $l = 80\,$nm and $w = 5\,\mu$m.

(always kept at -2.5 V to deplete the 2DEG there).

2. ESTIMATION OF LOOP INDUCTANCE

In order to extract the inductance of the SQUID loop, we measure the SQUID interference pattern for different reference JJ gate voltages, $V_{\mathrm{g,ref}}$. Figure S2a-l shows the obtained differential resistance maps as a function of applied current bias, I, and perpendicular magnetic field, B. Panel a-l corresponds to $V_{\mathrm{g,ref}} = 0$, -0.4, -0.8, -0.9, -1, -1.1, -1.2, -1.25, -1.3, -1.35, -1.4, and -1.45 V, respectively. The device JJ gate is grounded in all measurements. With the colored circles we mark the positions where the total critical current is maximum. For a given SQUID oscillation, the field at which the maximum occurs is different for positive and negative current bias: $\Delta B = B^+ - B^-$. The corresponding flux difference is given by: $\Delta\Phi = 2(L_{\mathrm{ref}} I_{\mathrm{c,ref}} - L_{\mathrm{dev}} I_{\mathrm{c,dev}})$ [2]. Here, $I_{\mathrm{c,ref}}$ and $I_{\mathrm{c,dev}}$ are the critical current of the reference and device junction, respectively. The inductances of the two SQUID arms are

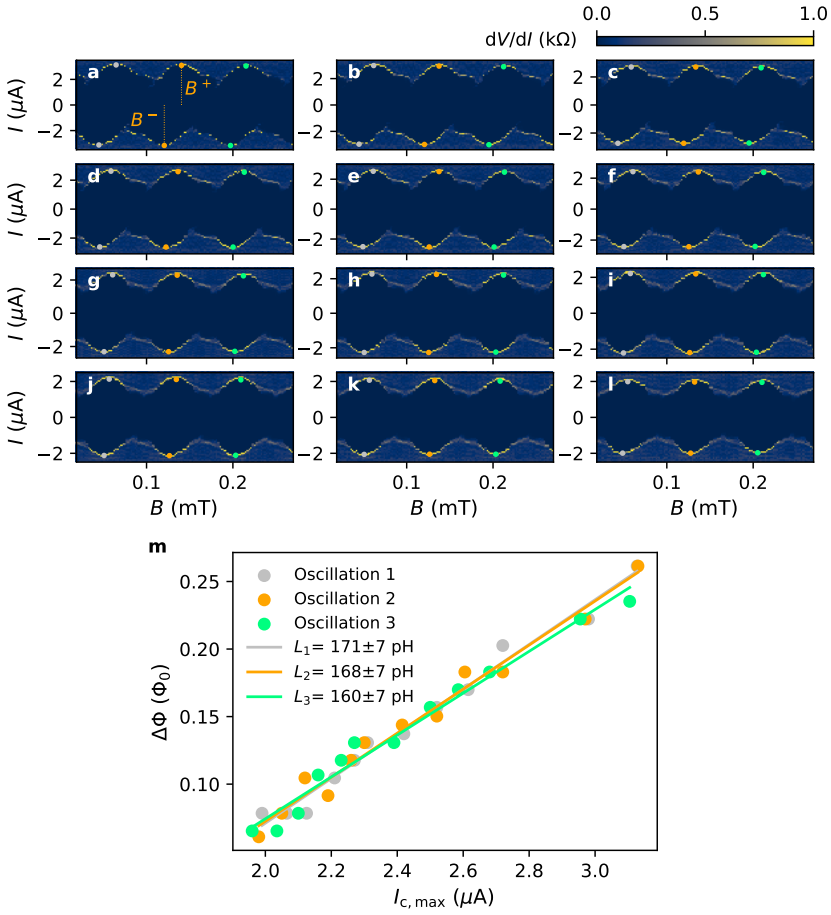

FIG. S2. Differential resistance, $\mathrm{d}V/\mathrm{d}I$, as a function of applied current bias, I, and perpendicular magnetic field, B. Panel **a-l** corresponds to reference gate voltage $V_{\mathrm{g,ref}} = 0$, -0.4, -0.8, -0.9, -1, -1.1, -1.2, -1.25, -1.3, -1.35, -1.4, and -1.45 V, respectively. No voltage is applied to the device junction gate. The colored circles mark the positions of maximum total critical current. **m** $\Delta\Phi$ plotted against $I_{\mathrm{c,max}}$ for the three oscillations shown in **a-l**. The extracted ΔB is normalized with respect to the oscillation period, giving $\Delta\Phi$ in units of the magnetic flux quantum, Φ_0. The average value of the maximum critical current on the positive and negative current bias sides gives $I_{\mathrm{c,max}}$.

L_{ref} and L_{dev}. The above expression can be rewritten as: $\Delta\Phi = 2L_{\mathrm{ref}}I_{\mathrm{c,max}} - 2LI_{\mathrm{c,dev}}$, using the relations for the maximum critical current, $I_{\mathrm{c,max}} = I_{\mathrm{c,ref}} + I_{\mathrm{c,dev}}$, and the total loop inductance, $L = L_{\mathrm{ref}} + L_{\mathrm{dev}}$.

In Fig. S2m we plot the extracted $\Delta\Phi$ as a function of $I_{\mathrm{c,max}}$ for the three oscillations indicated in Fig. S2a-l. The linear fits yield $L_{\mathrm{ref}} = 166$ pH as the average value. Since the width

and the thickness of the superconducting loop is the same for all three devices, the inductance should only depend on the length of the superconducting loop. Under this assumption the loop inductance of the phase-biased JJs can be estimated to be $L_{\mathrm{ref}} l_{\mathrm{PBJJ}}/l_{\mathrm{ref}} = 321\,\mathrm{pH}$, where $l_{\mathrm{ref}} = 15.3\,\mu\mathrm{m}$ is the length of SQUID reference arm and $l_{\mathrm{PBJJ}} = 29.6\,\mu\mathrm{m}$ is the loop length of Dev 1 and 2.

3. FLUX FOCUSING IN PLANAR JJ

The Fraunhofer interference pattern periodicity, B_0, in a JJ is determined by the geometrical area, A, enclosed between two superconducting leads, i.e. $B_0 = \Phi_0/A$. However, in the presence of flux focusing, the periodicity is reduced from the theoretical value [3]. To estimate the effect of flux focusing we measure the differential resistance, $\mathrm{d}V/\mathrm{d}I$, as a function of applied current, I, and perpendicular magnetic field, B, for the device JJ of the DC SQUID (see Fig. S3). For this measurement, the reference JJ is pinched off by applying a voltage of $-2.5\,\mathrm{V}$ to the top gate. We observe the first node at $2.1\,\mathrm{mT}$ instead of the expected Fraunhofer periodicity of $B_0 = 8.6\,\mathrm{mT}$. This gives a dimensionless flux focusing factor, f, of 4.1 for this junction.

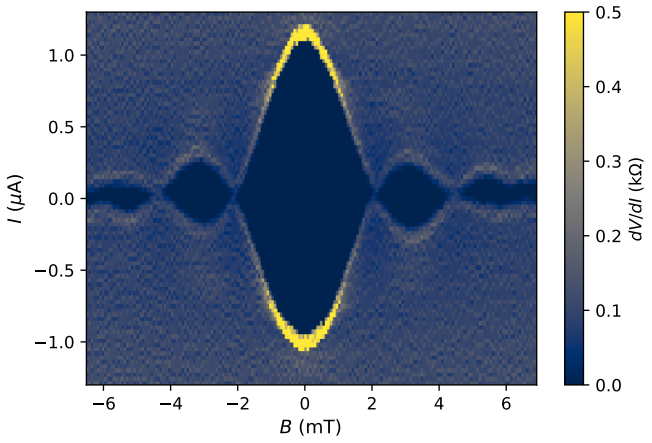

FIG. S3. Differential resistance, $\mathrm{d}V/\mathrm{d}I$, as a function of applied current, I, and perpendicular magnetic field, B for the device JJ of the DC SQUID.

To explain our spectroscopy maps measured at the top and bottom ends of Dev 1 and Dev 2 we introduce a toy model with flux focusing in Sec. 6. Although the above extracted f

gives an estimate of the focusing factor, the exact value can vary from junction to junction. The best agreement between the experimental spectroscopy maps and the toy model is be achieved with $f = 6.2$ for Dev 1 and 7.2 for Dev 2 (see Fig. 3 in the main text as well as Fig. S4]. The larger f values (and therefore stronger flux focusing) are in fact expected due to the shorter JJ length and larger lead length of Dev 1 and Dev 2 compared to the values for the device JJ of the DC SQUID [3].

4. JOSEPHSON PENETRATION DEPTH

The Josephson penetration depth for a JJ with the thickness of the superconducting electrodes comparable or smaller than the penetration depth is dominated by the kinetic inductance contribution and is given as [4]: $\lambda_J = (\Phi_0 w/4\pi\mu_0 J_c \lambda^2)^{1/2}$, where $w = 5\,\mu$m is the junction width, J_c is the critical current density, and λ is the superconducting penetration depth of Al.

For our junctions, the thickness of the Al electrodes (7 nm) is much smaller compared to the previously reported value of $\lambda = 180$ nm for a similar heterostructure [3]. Therefore we use the above expression to determine λ_J. Since the critical current cannot be measured for Dev 1 and Dev 2, we estimate it based on values obtained for the DC SQUID. The critical current of the device JJ with width $w = 2\,\mu$m is $I_c = 1.05\,\mu$A (see Fig. S3) and the thickness of 2DEG is $t = 30\,$nm. Using these values we get $J_c = I_c/wt = 1.75 \times 10^7 \mathrm{A/m^2}$ and $\lambda_J = 34\,\mu$m, which is much larger than the width of the JJs ($w = 5\,\mu$m). This ensures that the gauge-invariant phase difference can be expressed as $\varphi(y) = \phi + \phi'$, with $\phi' = -2\pi \frac{fBly}{\Phi_0}$.

5. TUNNELING SPECTROSCOPY FOR DEV 2

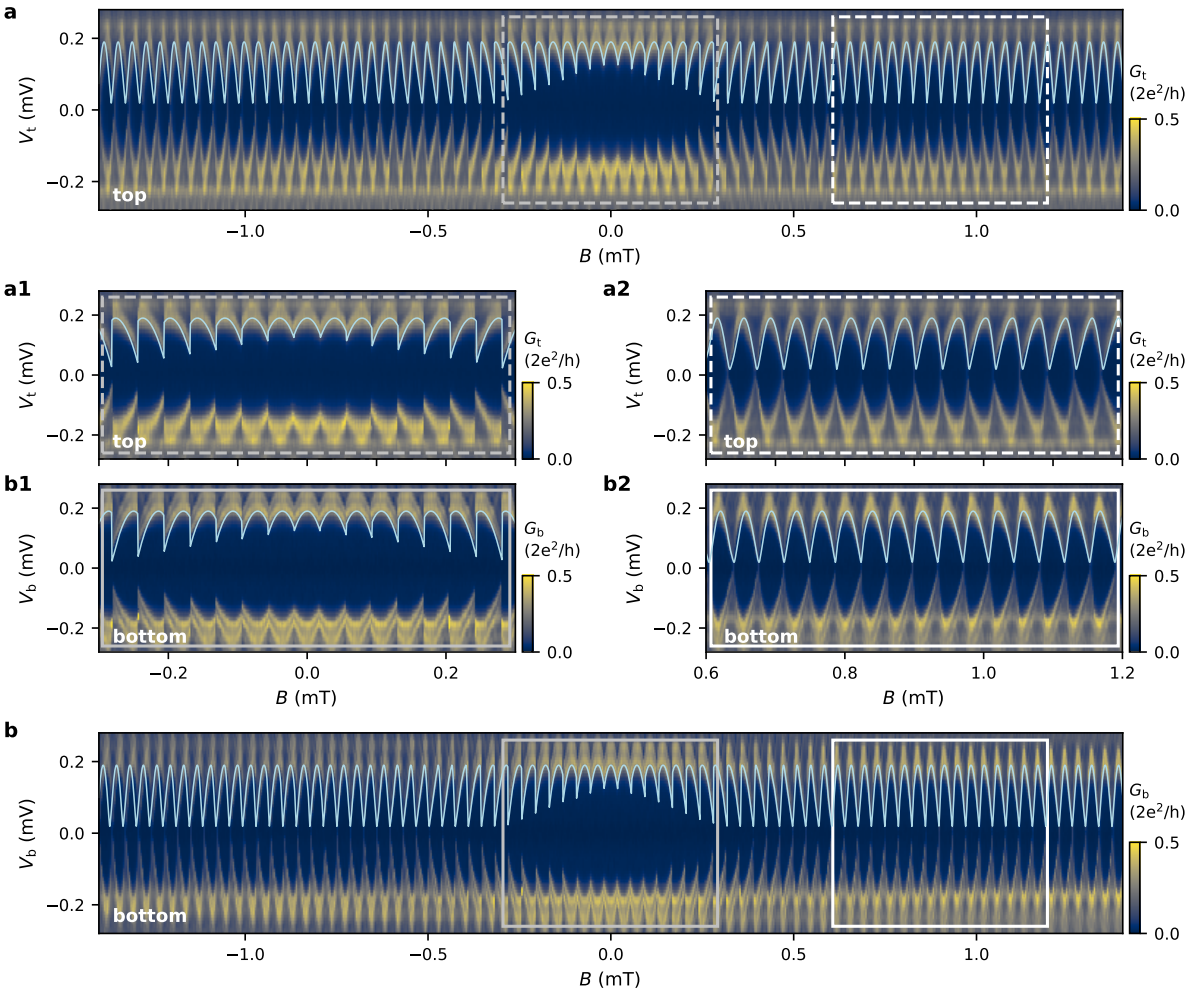

FIG. S4. **a** Spectroscopy map at the top end of Dev 2 with zoom-ins presented in **a1** and **a2**. The bottom spectroscopy map is shown in **b** with zoom-ins in **b1** and **b2**. Both measurements were obtained with $V_{g1} = -1.60\,\mathrm{V}$, $V_{g2} = -1.42\,\mathrm{V}$, $V_{g3} = -2.10\,\mathrm{V}$, $V_{g4} = -1.43\,\mathrm{V}$. The model (light blue line) assumes coupling to a single ABS ($\tau = 0.99$), taking into account the local phase difference in the JJ and the loop inductance ($L = 321\,\mathrm{pH}$) for the field-phase conversion.

6. TOY MODEL

This model is used to calculate the Andreev bound states (ABSs) energies of a Josephson junction embedded in a superconducting loop in the presence of a perpendicular magnetic field, as used to substantiate the measurement results shown in Fig. 3 and Fig. S5. The junction has a length l (the distance between the superconducting contacts) and a width w (the distance between the edges of the junction where the tunneling probes are connected).

We assume a homogeneous density of the supercurrent in the junction and that the current is carried by M ABSs uniformly distributed across the junction at positions $y_n = -w/2 + (n-1) \cdot w/(M-1)$ with integer $n \in [1, M]$.

The positive energies of the ABSs in the junction with the transmission coefficient τ are given by [5]:

$$E_n(\varphi_n) = \Delta\sqrt{1 - \tau \sin^2(\frac{\varphi_n}{2})}, \tag{S1}$$

where, in the presence of the external perpendicular magnetic field, $\varphi_n = \phi + \frac{2\pi}{\Phi_0}\int_{(0,y_n)}^{(l,y_n)} \mathbf{A} \cdot d\mathbf{l}$ is the gauge-invariant phase drop across the junction for an ABS located at position y_n. ϕ is the superconducting phase difference. For the vector potential in the Landau gauge $\mathbf{A} = (-yB, 0, 0)$, the phase drop in the junction at y_n is $\varphi_n = \phi - (2\pi/\Phi_0) \cdot fBly_n$, where we included f as the magnetic field focusing factor. The latter equation gives the phase evolution of the ABS located at the edges of the junction as $\varphi_{\mathrm{t/b}} = \phi \mp (\pi/\Phi_0) \cdot fBlw$ [6] with a minus (plus) sign for the upper (bottom) edge.

The zero-temperature supercurrent obtained from the positive-energy ABSs in the junction is given by:

$$I(\varphi) = \frac{e\Delta^2\tau}{2\hbar}\sum_n^M \frac{\sin(\varphi_n)}{E_n(\varphi_n)}. \tag{S2}$$

In the experimental setup, the superconducting phase difference ϕ is induced by a flux $\Phi = B\pi R^2$ that threads a superconducting loop with radius R. The non-zero loop inductance L results in the following phase-flux relation [7]:

$$\phi = \frac{2\pi}{\Phi_0}(\Phi - LI(\varphi)). \tag{S3}$$

We obtain the energies of the ABSs located at the edges of the junction versus B using the following procedure. In the first step, we solve Eq. S3 for a given B and obtain the ϕ value that minimizes the total energy of the system $E(\phi) = LI^2(\varphi)/2 - \sum_n^M E_n(\varphi_n)$ calculated

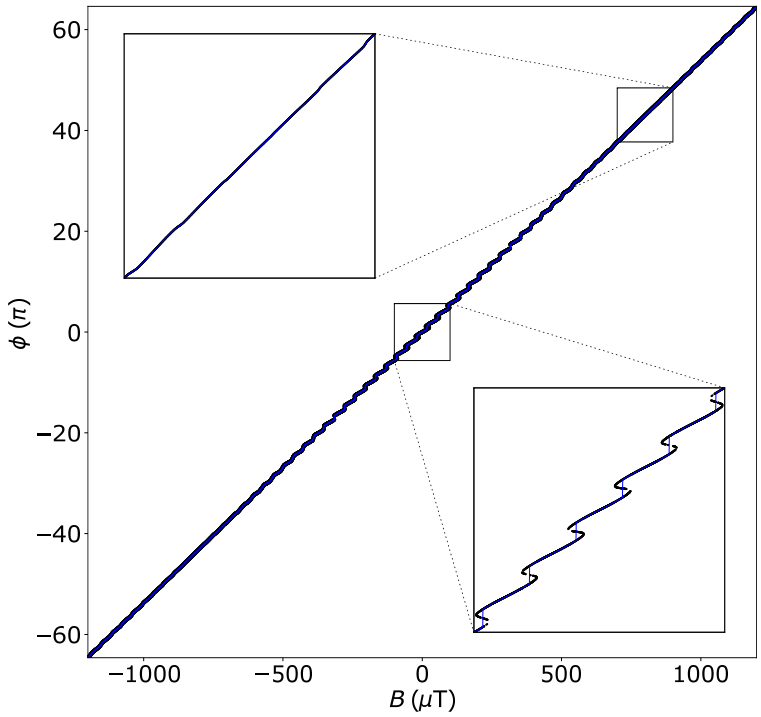

FIG. S5. Superconducting phase difference versus applied magnetic field obtained for $L = 321$ pH, $l = 80$ nm, $w = 5000$ nm, $M = 35$, $\tau = 0.99$, $R = 4207$ nm, $\Delta = 0.2$ meV and $f = 6.2$. The black dots show possible phase values for a given B, while the blue curve shows the superconducting phase difference obtained by minimizing the total energy.

as the sum of the energy contained in the superconducting loop and the free energy of the junction ($F = const - E_j = const - \sum E_n$). An example of a flux-to-phase conversion curve is shown in Fig. S5. Finally, we use the phase difference value to calculate E_n corresponding to the ABSs located at the outermost edges of the junction using Eq. S1.

Figure S6 shows an ABS located at the top (top panel) and bottom (bottom panel) end of the JJ in the presence and absence of the loop inductance and the local phase difference arising from the magnetic vector potential as indicated. The reversal of the skewness can only happen when both the loop inductance and the local phase difference are present.

Table S1 summarizes the parameters that are used for the overlays for Dev 1 (Fig. 3 of the main text) and Dev 2 (Fig. S4).

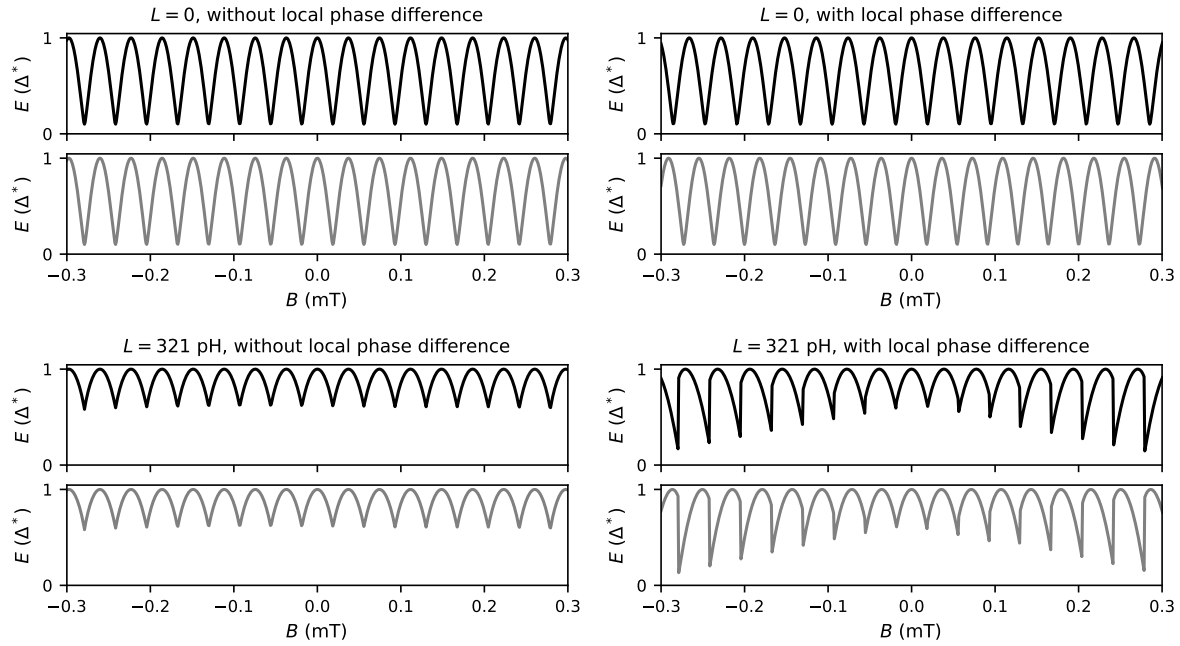

FIG. S6. ABS energy versus magnetic field in the presence or absence of the loop inductance and with or without local phase difference in the JJ as indicated. The top and bottom panels correspond to an ABS located at the top and bottom end of the JJ, respectively. For all plots, the following parameters are used: $l = 80$ nm, $w = 5000$ nm, $M = 35$, $\tau = 0.99$, $R = 4207$ nm, $\Delta = 0.2$ meV and $f = 6.2$.

Parameter	Dev 1	Dev 2
l (nm)	80	80
w (μm)	5	5
R (nm)	4207	4190
L (pH)	321	321
Δ (meV)	0.2	0.19
f	6.2	7.2
M	35	45
τ	0.99	0.99

TABLE S1. Toy model parameters used for Dev 1 and Dev 2.

7. MICROSCOPIC MODEL

A. Tunneling spectroscopy calculations

We consider a four-terminal device, with two vertical superconducting leads separated by the normal region (which creates the superconductor-normal-superconductor junction) and two normal leads that are placed horizontally at the top and bottom—see Fig. S7. Between the horizontal leads and the normal scattering region, we introduce tunneling barriers that mimic the behavior of QPCs tuned into the tunneling regime.

The considered system is described by the Hamiltonian

$$\begin{bmatrix} H & \Delta \\ \Delta^* & -H \end{bmatrix}, \tag{S4}$$

acting on a wave function in the basis $\Psi = (\Psi_e, \Psi_h)^T$. Here H is defined as

$$H = -\frac{\hbar^2}{2m^*}\nabla^2 + V(r) - \mu. \tag{S5}$$

μ is the chemical potential, m^* is the effective electron mass and $V(r)$ is the rectangular potential barrier of height V_g placed just above and below the normal region of length ($l = 80$ nm).

In the presence of a magnetic field, the Hamiltonian H becomes

$$H' = -\frac{\hbar^2}{2m^*}(\nabla - q\mathbf{A}/\hbar)^2 + V(r) - \mu, \tag{S6}$$

with $q = -|e|$ for the electron and $q = |e|$ for the hole part of the Hamiltonian Eq. S4. We choose the vector potential in the Landau gauge with $\vec{B} = B\hat{z}$, so that $\vec{A} = -By\hat{x}$

The superconducting pairing potential Δ varies spatially and is given by:

$$\Delta(x) = \begin{cases} \Delta_0 & \text{if } x < -l/2 \\ 0 & \text{if } -l/2 \leq x \leq l/2 \\ \Delta_0 e^{\iota\phi} & \text{if } x > l/2 \end{cases}$$

We discretize the Hamiltonian Eq. S4 on a square lattice with discretization constant $a = 10$ nm. We put the material parameters as $m^* = 0.016m_e$, $\mu = 5$ meV, $\Delta = 0.2$ meV. We introduce the anisotropic mass in the superconducting leads with the mass along the

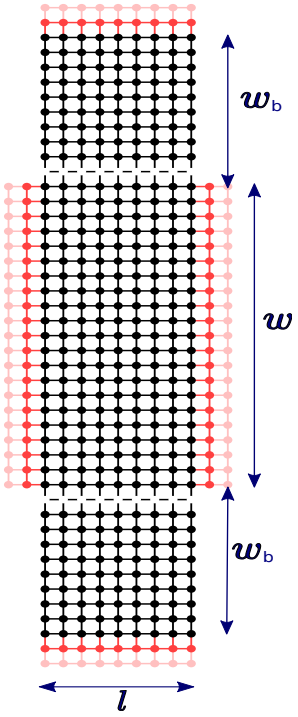

FIG. S7. Schematic of the system considered for tunneling spectroscopy calculations. The dots denote the sites of the computational mesh. The black dots correspond to the scattering region, whereas the pink ones denote the semi-infinite leads. We use $l = 80$ nm (the distance between the superconducting contacts) and $w = 5000$ nm (the distance between the edges of the junction where the tunneling probes are connected). The barrier potential at the top and bottom is separated from the normal leads of width $w_b = 100$ nm. The vertical leads are superconducting, while the horizontal leads are normal.

translation symmetry of the superconducting leads equal to $10m^*$ as appropriate for the description of transparent normal-superconductor interfaces in models where the chemical potential is kept constant [8]. Including a vector potential in this system is done using Peierls substitution as $t_{nm} \to t_{nm} \exp[\frac{-\imath e}{\hbar} \int \mathbf{A} d\mathbf{l}]$ [9, 10].

We exclude the magnetic field from the superconducting leads to account for the screening effect setting $\mathbf{A} = 0$ there. We also put zero vector potential in the top and bottom leads to maintain the translation invariance. This in turn introduces a delta peak in the magnetic field where the horizontal leads are attached (as calculated from $\mathbf{B} = \nabla \times \mathbf{A}$). We have,

however, verified that for the considered small magnetic fields, this does not affect our results, as confirmed by replacing the vector potential by a position-dependent superconducting phase as $\phi \to \phi - \frac{2\pi Bly}{\Phi_0}$ and observing that both results match accurately.

The finite mean free path (l_e) is implemented by introducing a random on-site disorder potential $V_d(x, y)$ with the amplitude uniformly distributed between $-U_d/2$ and $U_d/2$ [11], where

$$U_d = \mu \sqrt{\frac{6\lambda_F^3}{\pi^3 a^2 l_e}}. \tag{S7}$$

Here a, l_e, λ_F are the lattice constant, mean free path and the Fermi wavelength, respectively. We calculate the conductance map with respect to the phase difference ϕ and energy using the scattering matrix approach implemented in the Kwant package [12], using the formula:

$$G_{t/b} = \frac{2e^2}{h}(N^e_{t/b} - T^{ee}_{t/b} + T^{he}_{t/b}), \tag{S8}$$

where t and b stand for top and bottom lead respectively and $N^e_{t/b}$ is the corresponding number of the electron modes. The energy dependent transmissions are evaluated as:

$$T^{\alpha\beta}_{t/b} = Tr([S^{\alpha\beta}_{t/b}]^\dagger S^{\alpha\beta}_{t/b}), \tag{S9}$$

where $S^{\alpha\beta}_{t/b}$ is the block of scattering amplitudes of incident particle of type β in t (b) lead to a particle of type α in the lead t (b).

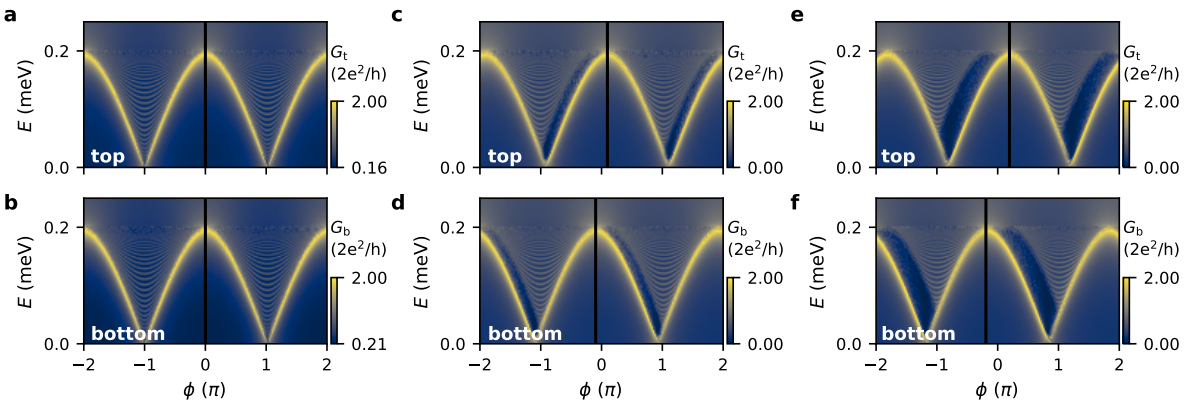

FIG. S8. Conductance versus phase difference and energy calculated for quasiparticles injected from the top lead (upper row) and bottom lead (lower row) at $B = 0$ (**a**,**b**), $B = 0.5$ mT (**c**,**d**) and $B = 1$ mT (**e**,**f**). The vertical black lines denote the expected phase shift of the edge modes due to the magnetic field $\varphi_{\mathrm{t/b}} = \phi \mp (\pi/\Phi_0) \cdot fBlw$.

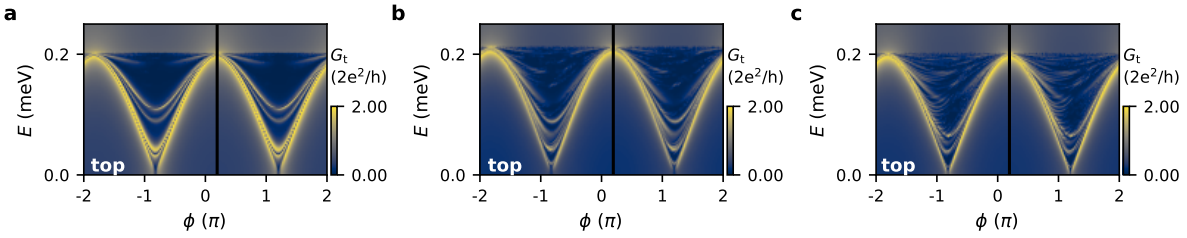

FIG. S9. Conductance versus phase difference and energy calculated for quasiparticles injected from the top lead for $B = 1$ mT and different mean free paths $l_e = 150$ **a**, 500 **b** and 1000 nm **c**.

B. ABS calculation

For the numerical calculation of ABSs spectra we consider a Josephson junction treated as a finite system consisting of a normal scattering region and two long superconducting segments. The two superconducting regions have a length of $l_{SC} = 2000$ nm (much larger than the coherence length $\xi = 1091.16$ nm, calculated using the formula, $\xi = \frac{\hbar v_F}{\Delta}$ where $v_F = \sqrt{2\mu/m^*}$), and they are separated by a normal region of length $l = 80$ nm. The width w of the entire system is taken as 1000 nm. The Hamiltonian remains the same as in equation S6 except for the tunneling barrier potentials (here we do not consider the top and bottom electrode). The anisotropic mass and Peierls phase factor (for magnetic vector potential) are introduced as described above. We diagonalize the Hamiltonian and plot the energy with respect to the phase difference ϕ, and also the probability current in Fig. S10. In the probability current, we observe that in the presence of the perpendicular field each ABSs is localized in a separated region in the junction. The different spatial position of the ABSs is reflected by their different phase shifts in the spectrum plotted in Fig. S10 (a).

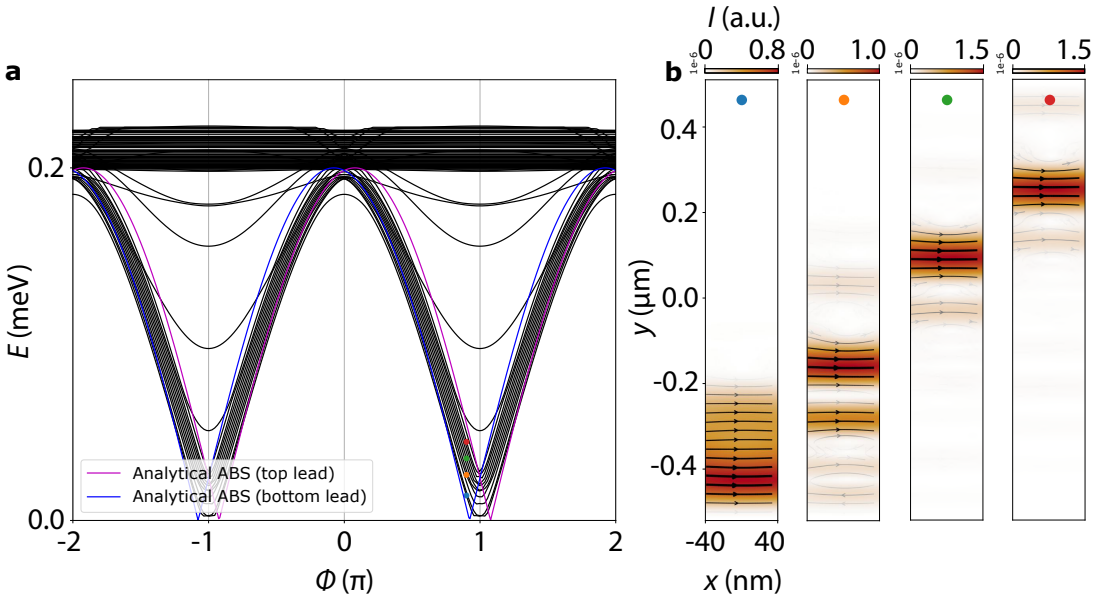

FIG. S10. **a** ABS spectrum of a SNS junction with two SC regions ($l_{SC} = 2000$ nm) separated by a normal region ($l = 80$ nm, $w = 1000$ nm) at $B = 2$ mT without disorder. The color curves denote analytically calculated ABS from Eq. S1 with $\tau = 1$. **b** Supercurrent in the normal area of the junction calculated for the ABS whose energies are denoted by the color circles in **a**.

References

[1] T. Laeven, B. Nijholt, M. Wimmer, and A. R. Akhmerov, Enhanced proximity effect in zigzag-shaped majorana josephson junctions, Phys. Rev. Lett. **125**, 086802 (2020).

[2] A. I. Braginski and J. Clarke, *The SQUID Handbook* (John Wiley and Sons, Ltd, 2004).

[3] H. J. Suominen, J. Danon, M. Kjaergaard, K. Flensberg, J. Shabani, C. J. Palmstrøm, F. Nichele, and C. M. Marcus, Anomalous Fraunhofer interference in epitaxial superconductor-semiconductor Josephson junctions, Phys. Rev. B **95**, 035307 (2017).

[4] S. K. Tolpygo and M. Gurvitch, Critical currents and Josephson penetration depth in planar thin-film high-t_c Josephson junctions, Appl. Phys. Lett. **69**, 3914 (1996).

[5] C. W. J. Beenakker, Universal limit of critical-current fluctuations in mesoscopic Josephson junctions, Phys. Rev. Lett. **67**, 3836 (1991).

[6] D. Sticlet, P. Wójcik, and M. P. Nowak, Squid pattern disruption in transition metal dichalcogenide Josephson junctions due to nonparabolic dispersion of the edge states, Phys. Rev. B **102**, 165407 (2020).

[7] A. Banerjee, O. Lesser, M. A. Rahman, H. R. Wang, M. R. Li, A. Kringhøj, A. M. Whiticar, A. C. C. Drachmann, C. Thomas, T. Wang, M. J. Manfra, E. Berg, Y. Oreg, A. Stern, and C. M. Marcus, Signatures of a topological phase transition in a planar Josephson junction, arXiv.2201.03453 (2022).

[8] D. Sticlet, B. Nijholt, and A. Akhmerov, Robustness of Majorana bound states in the short-junction limit, Phys. Rev. B **95**, 115421 (2017).

[9] R. Peierls, Zur theorie des diamagnetismus von leitungselektronen, Zeitschrift für Physik **80**, 763 (1933).

[10] D. R. Hofstadter, Energy levels and wave functions of bloch electrons in rational and irrational magnetic fields, Phys. Rev. B **14**, 2239 (1976).

[11] T. Ando, Quantum point contacts in magnetic fields, Phys. Rev. B **44**, 8017 (1991).

[12] C. W. Groth, M. Wimmer, A. R. Akhmerov, and X. Waintal, Kwant: a software package for quantum transport, New J. Phys. **16**, 063065 (2014).

Chapter 6

Nonlocal transport signatures of topological superconductivity in a phase-biased planar Josephson junction

Reprinted with permission from Kuiri, D., and Nowak, M. P., *Physical Review B*, **108**, 205405 (2023).
DOI: 10.1103/PhysRevB.108.205405

Nonlocal transport signatures of topological superconductivity in a phase-biased planar Josephson junction

D. Kuiri [*] and M. P. Nowak [†]

AGH University of Krakow, Academic Centre for Materials and Nanotechnology, al. A. Mickiewicza 30, 30-059 Krakow, Poland

(Received 30 June 2023; revised 4 October 2023; accepted 12 October 2023; published 3 November 2023)

Hybrid Josephson junctions realized on a two-dimensional electron gas are considered promising candidates for developing topological elements that are easily controllable and scalable. Here, we theoretically study the possibility of the detection of topological superconductivity via the nonlocal spectroscopy technique. We show that the nonlocal conductance is related to the system's band structure, allowing probe of the gap closing and reopening related to the topological transition. We demonstrate that the topological transition induces a change in the sign of the nonlocal conductance at zero energy due to the change in the quasiparticle character of the dispersion at zero momentum. Importantly, we find that the tunability of the superconducting phase difference via flux in hybrid Josephson junctions systems is strongly influenced by the strength of the Zeeman interaction, which leads to considerable modifications in the complete phase diagram that can be measured under realistic experimental conditions.

DOI: 10.1103/PhysRevB.108.205405

I. INTRODUCTION

Planar superconductor-normal-superconductor (SNS) Josephson junctions have been proposed as a promising platform for engineering and exploiting Majorana bound states due to the tunability of the topological transition by the superconducting phase difference [1] and the scalability of two-dimensional (2D) heterostructure systems [2]. For the realization of topological SNS devices, typically two separate superconducting electrodes proximitize the two-dimensional electron gas (2DEG), creating a SNS junction where the good quality of the normal-superconducting interfaces results in an induced gap close to that of the parent superconductor [3]. Upon application of an in-plane magnetic field, the Zeeman interaction leads to the splitting of Andreev bound states (ABS) in phase, resulting in the opening of the topological regime whenever the fermion parity is odd [1]. The topological regime is already obtained for the vanishingly small Zeeman interaction energies at the phase difference π. This becomes an important factor in achieving the topological superconductivity in SNS junctions realized on normal-superconductor hybrids as a strong Zeeman interaction can lead to the appearance of an abundance of trivial in-gap states [4,5] that decrease the induced gap and can obscure Majorana zero-energy modes.

Originally, in normal-superconductor nanostructures, such as proximitized nanowires [6], Majorana bound states were sought by tunneling spectroscopy, where the presence of a zero-bias peak was assigned to the appearance of topological zero-energy states [7–9]. However, zero-bias peaks can also result from disorder-induced trivial ABS [10–12] or be due to the specifics of the tunneling barriers used [13].

Tunneling spectroscopy was considered [14] (among other techniques such as scanning tunneling microscopy [15] or its spin-polarized variant [16]) as a way to probe bound states in planar SNS junctions. It allowed revealing the edge-dependent evolution of ABS in the perpendicular field [17–19]. In fact the zero-bias peaks were observed in planar SNS junctions [20,21] but, as in the case of nanowire systems, single-edge conductance cannot be considered as a conclusive determinant of the topological character of a zero-energy state. Relying on the observation of a single feature expected for topological systems can lead to false positive results [11,22]. Instead, specialized protocols [23,24] have recently been proposed that require the observation of several signatures of the topological transition, preferably in a wide range of experimentally controllable parameters.

In this context, a promising method is a nonlocal measurement [25,26], which has recently been the subject of intense research effort. Local and nonlocal spectroscopy was recently performed on planar SNS junctions in the tunneling regime [27], but lacked a clear signature of the topological transition. In this work, we focus on the signatures of the topological transition in phase-biased SNS junctions in nonlocal measurements in the context of recently realized two-dimensional Josephson junction heterostructures [17,18,26]. We theoretically study the transport features of the junction both in the spectroscopy limit, i.e., tunneling measurements that are sensitive to the density of states in the junction, and in an open regime, i.e., without tunneling barriers, where the transport features correspond rather to a band structure of the junction. The latter can elucidate the closing and reopening of the gap associated with the topological transition [26].

We find that the nonlocal conductance sign represents the electron- or holelike character of the bands in the junction.

[*] kuiri@agh.edu.pl
[†] mpnowak@agh.edu.pl

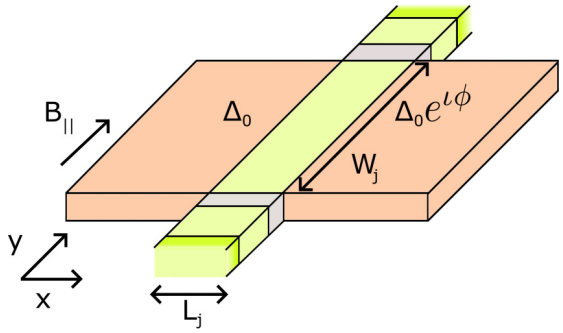

FIG. 1. Schematic diagram of the considered system. A semiconductor strip (yellow-green) is sandwiched between two superconducting electrodes (orange), whose pairing potential has phase difference ϕ. The gray regions denote the potential barriers, placed just above and below the SC region. The green segments in the semiconductor denote the top (1) and bottom (2) normal leads.

The closing and reopening of the gap at $k = 0$ is associated with the meeting of the electron and hole bands at zero energy and, correspondingly, with the change in the sign of the nonlocal conductance. Furthermore, we discuss a serious caveat in the realization of the topological phase in SNS junctions. Namely, we show that in a realistic situation, where phase biasing is done by running a flux through a superconducting loop embedding the SNS junction, the phase slips result in skipping a large region of phase space close to π, prohibiting the creation and probing of Majorana bound states at a small field. We discuss the factors that allow one to limit this obstacle.

The paper is structured as follows. In Sec. II we introduce the numerical model. In Sec. III A we discuss nonlocal spectroscopy results in relation to the effective charge polarization of the bands. In Sec. III B we show how experimentally performed phase biasing limits the magnetic fields in which the topological phase can be observed. We discuss our results in Sec. IV and summarize them in Sec. V.

II. MODEL

We consider a planar SNS junction constituted by a semiconducting strip of length L_j connected to superconducting electrodes of width W_j. The scheme of the considered structure is depicted in Fig. 1.

The Hamiltonian of the system written in the basis $\Psi = (\psi_{e\uparrow}, \psi_{h\downarrow}, \psi_{e\downarrow}, -\psi_{h\uparrow})^T$ (where e and h correspond to electron and hole components with spin up $\uparrow$ or down $\downarrow$, respectively) is

$$H = \left(\frac{\hbar^2 {k_x}^2}{2m^*} + \frac{\hbar^2 {k_y}^2}{2m^*} - \mu\right)\sigma_0 \otimes \tau_z + \frac{1}{2}g(x)\mu_B B\sigma_y \otimes \tau_0 + \alpha(x)(\sigma_x k_y - \sigma_y k_x) \otimes \tau_z + \Delta(x)\tau_+ + \Delta^*(x)\tau_-, \quad (1)$$

where $k_{x(y)} = -\imath\partial/\partial x(y)$, σ_i and τ_i with $(i = x, y, z)$ are the Pauli matrices that act on the spin and electron-hole degree of freedom, respectively, with $\tau_\pm = (\sigma_0 \otimes \sigma_x \pm \imath\sigma_0 \otimes \sigma_y)/2$, where σ_0 is the (2×2) identity matrix.

We consider the nonzero pairing potential in superconducting contacts, which is modeled by the spatial dependence of the gap parameter $\Delta(x)$,

$$\Delta(x) = \begin{cases} \Delta_0 & \text{if } x < -L_j/2, \\ 0 & \text{if } -L_j/2 \leqslant x \leqslant L_j/2, \\ \Delta_0 e^{\imath\phi} & \text{if } x > L_j/2, \end{cases}$$

with ϕ the superconducting phase difference. Accordingly, we neglect the Zeeman splitting and spin-orbit effects in the superconductor setting $g(x) = \alpha(x) = 0$ in them. The in-plane magnetic field is applied along the y direction. For concreteness, we adopt the material parameters corresponding to the InSb semiconductor and the Al superconductor, that is, $m^* = 0.014m_e$, $\mu = 5$ meV, $\Delta_0 = 0.2$ meV, and $\alpha = 50$ meV nm. We also assume typical dimensions for this type of structure, that is, $L_j = 80$ nm and $W_j = 2000$ nm [18,21,27].

For numerical simulations, we discretize the Hamiltonian on a square lattice with the lattice constant $a = 10$ nm. Since we use a uniform chemical potential in our calculations, for a proper description of Andreev scattering at the NS interface [28], we introduce an anisotropic mass in the superconducting leads with the effective mass in the direction parallel to the interface $m^*_\parallel = 10m^*$ [29]. The code used for the presented calculations is available online [30].

In this study, we consider three variants of the SNS system. The first is the *open* system as shown in Fig. 1 used to study the transport properties. Here, the normal regions extend beyond the width of the superconducting contacts by length 100 nm, which includes 10 nm tunneling barriers of height 50 meV. They are connected to semi-infinite leads that allow the transport of in-gap electrons/holes into/from the junction. The normal region is connected to semi-infinite superconducting leads. Such geometries have recently been experimentally realized in InSbAs [18] or InAs [27] 2DEGs proximitized by Al.

Experimentally, the nonlocal conductance is measured by grounding the superconductor and registering the current change in one of the normal leads upon application of the voltage bias in the other. Numerically we calculate the nonlocal conductance considering the scattering properties of the quasiparticles injected and scattered back to normal leads using the scattering matrix approach implemented in the Kwant package [31] with the formula

$$G_{ij}(E) = \frac{\partial I_i}{\partial V_j} = \frac{e^2}{h}\left(T^{ee}_{ij} - T^{he}_{ij} - \delta_{ij}N^e_i\right). \quad (2)$$

I_i is the current entering terminal i from the scattering region, V_j is the voltage at terminal j, and N^e_i is the number of electron modes at energy E in terminal i. T^{ee}_{ij} and T^{he}_{ij} are electron-to-electron and electron-to-hole transmission amplitudes (with j being the source and i the drain) calculated at energy E that represents the applied bias voltage V_j at zero temperature [26].

To investigate the properties of the bound states that form in the junction, we consider a finite *isolated* system by disconnecting the protruding normal segments and leads [32]. Finally, to study the properties of the band structure, we introduce the *translation-invariant* system constructed by removing the normal leads and making the junction invariant in the y direction, where k_y is a good quantum number.

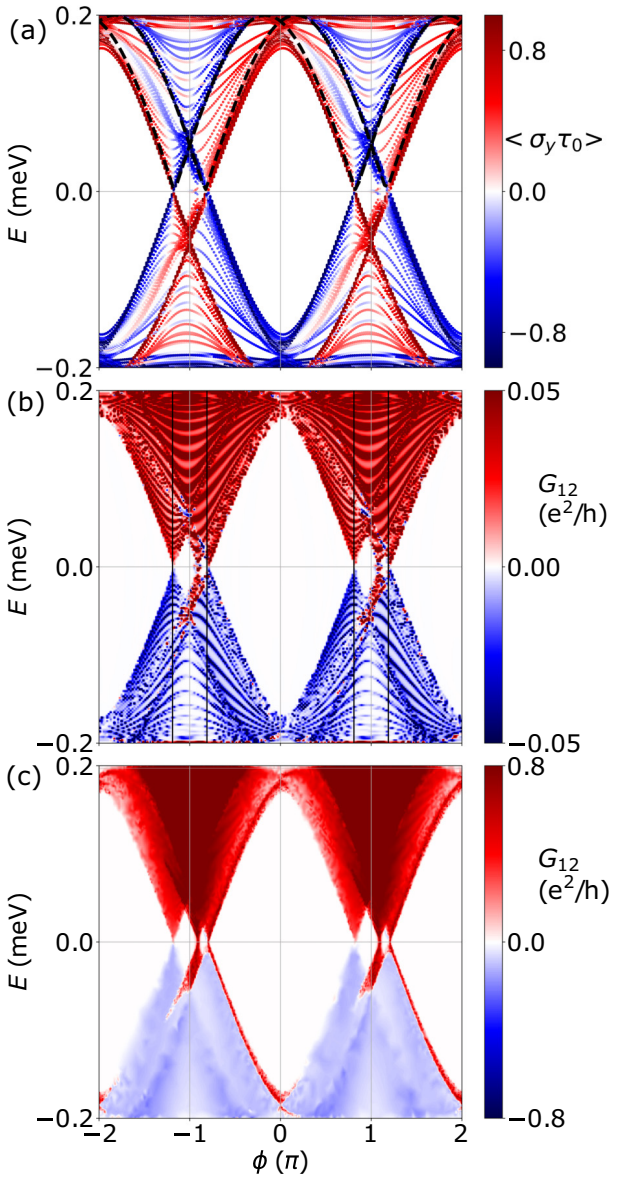

FIG. 2. (a) ABS energy spectrum of the isolated SNS junction. The analytical ABS spectrum is shown with black dashed lines. The colors denote the average spin polarization of ABS along the y direction. Nonlocal conductance with (b) and without (c) tunneling barriers versus the superconducting phase difference. The results are obtained for the in-plane field $B = 0.5$ T.

III. RESULTS

A. Nonlocal conductance as a measure of topological transition

The 2π-periodic spectrum of isolated junction in a nonzero in-plane field is shown in Fig. 2(a). The evolution of the ABS of a single-mode spinful junction in the presence of the magnetic field is captured by the formula

$$E_\sigma(\phi) = \Delta\sqrt{1 - \tau\,\sin^2\left(\frac{\phi + \varphi_\sigma}{2}\right)}, \tag{3}$$

where $\varphi_\sigma = 2\sigma E_z L_j/\hbar v_F$, τ is the junction transmission coefficient, $E_z = g\mu_B B/2$ is the Zeeman energy, $\sigma = \pm 1$ corresponds to positive and negative spin components, and $v_F = \sqrt{2\mu/m^*}$ is the Fermi velocity. Overlaying the numerically calculated spectrum with the analytical one in Fig. 2(a) we see that the cones made up of ABS are split in phase by the Zeeman interaction. Inspecting the mean spin polarization of ABS calculated as the expectation value of the operator $\sigma_y\tau_0$, we observe that the edge of each cone is made of ABS with positive and negative spin polarization along the y direction. Upon increasing the magnetic field, for the negative g factor considered here, the positively (negatively) spin-polarized states move down (up) in energy. This in turn results in an increase in the distance between the positive-energy cones. The bottom tip of each cone sets out a phase point when the fermion parity changes and the system undergoes a phase transition—with the topological phase being present in each $\phi = [0, 2\pi]$ (mod 2π) segment only between the cones. Since the plot shows spin polarization, the spinless Majorana bound states are not visible.

Calculating the nonlocal tunneling spectroscopy we obtain the map shown in Fig. 2(b) where the gap closing and reopening upon the increase of the superconducting phase is visible. An analogous result is obtained when the tunneling barriers are removed [Fig. 2(c)]. Most importantly, we observe that in both plots the topological transition manifests itself as the sign change of the nonlocal signal at zero energy [see the vertical black lines in Fig. 2(b)] leading to the rectification of the current, similar to the case of an NS junction [26].

In Figs. 2(b) and 2(c) there is also a middle cone visible in which the nonlocal conductance does not change sign at zero energy and which does not mark the topological transition, as we will show in the following.

1. Charge polarization of the bands

As we will show, the sign of nonlocal conductance outlines the leading transport phenomenon in the junction. According to the formula, Eq. (2), a positive conductance signal is obtained when the dominant transport process involves electron transport through the proximitized region, while a negative signal is obtained when the electron is converted into a hole in a crossed Andreev reflection process.

To elucidate the change of the nonlocal conductance, we consider an invariant system. In Fig. 3(a) we plot the dispersion relation obtained for the phase difference set in the vicinity of the left cone, that is, $\phi = 0.84\pi$. We see the gap closing at $k_y = 0$ as the bands cross zero energy, causing the fermion parity change, which in turn leads to the topological transition.

We introduce the quasiparticle polarization of the bands factor (P) which is calculated as $P = vk_y$, where $v = \frac{1}{\hbar}\frac{\partial E}{\partial k_y}$ and color the bands in the dispersion relation in Fig. 3(a) with it. We observe that the bands at positive energy mostly have an electronlike character, i.e., the sign of the Fermi velocity matches the sign of the wave vector k_y. The situation for negative energy is the opposite and the bands there are mostly of a holelike character.

Positive band polarization allows electrons with positive energies to flow between the top and bottom contacts with little Andreev reflection [see Fig. 3(b)]. We observe that the electron can freely propagate from the bottom to the top

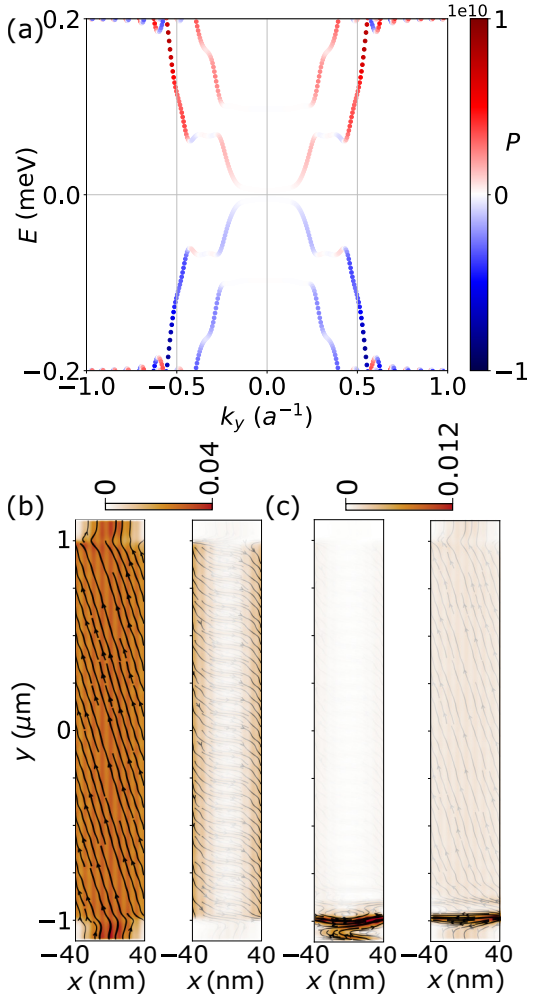

FIG. 3. (a) Dispersion relation for $B = 0.5$ T and $\phi = 0.84\pi$. The colors denote the average charge polarization of the bands. Electron (left) and hole (right) components of probability currents obtained for $E = 0.169$ meV (b) and $E = -0.169$ meV (c).

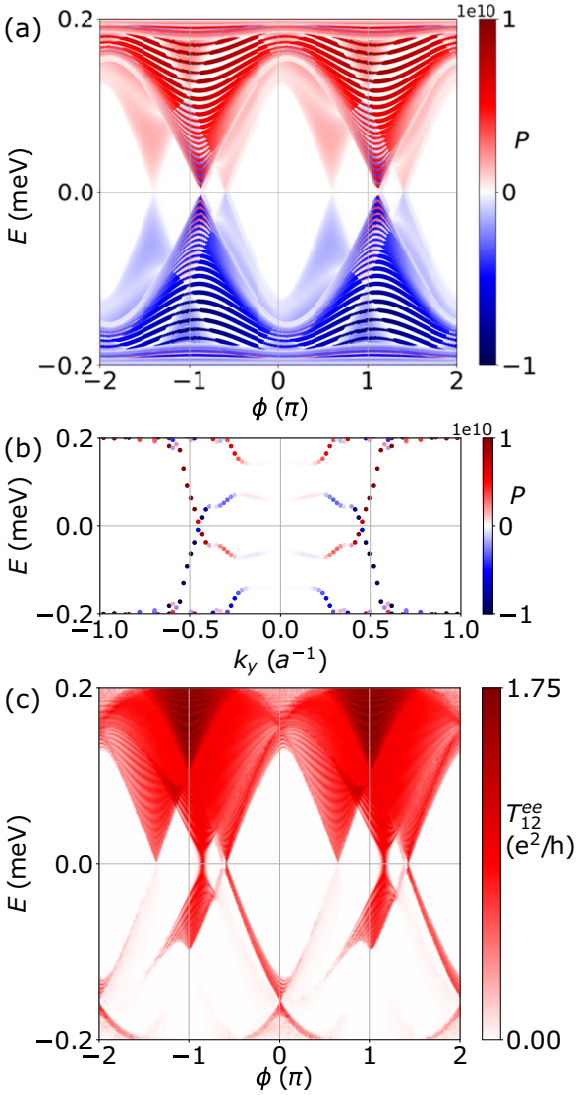

FIG. 4. Charge polarization obtained for $k_y \in [-a^{-1}, a^{-1}]$ versus energy and phase difference. (b) The band structure obtained for $\phi = 1.15\pi$. (c) T_{12}^{ee} nonlocal conductance component. The results are obtained for $B = 1$ T.

contact [left map in Fig. 3(b)] with little Andreev reflection [right map in Fig. 3(b)]. On the other hand, the mostly hole character of the negative energy bands results in a blockade of the electron transport [see the left map in Fig. 3(c)] and instead crossed Andreev reflection occurs [see the right map in Fig. 3(c)], which in turn results in negative nonlocal conductance that is related to the splitting of the Cooper pairs between top and bottom contacts.

It should also be noted that part of the band structure can also have an electronlike character, even at negative energy, which, e.g., can cause the red outlines of the rightmost cone at negative energy as seen in Fig. 2(c).

In Fig. 4(a) we show the P factor for the invariant system calculated by projecting the P values obtained in the range $k_y \in [-a^{-1}, a^{-1}]$ for each phase difference value for the increased in-plane field $B = 1$ T. We indeed see that in the outermost cones in each 2π segment of the spectrum the particle polarization of the bands is positive at positive energy and vice versa. The opposite polarizations result in the change of the sign of the nonlocal conductance at zero energy, which marks the topological transition.

In the map of Fig. 4(a) there is also a clear signature of the appearance of positively charged bands both in positive and negative energy between the two outermost cones in the topological region. If we look at the exemplary dispersion relation, obtained for the phase where the positive- and negative-energy middle cones meet [Fig. 4(b)], we observe that the gap closing occurs at nonzero k_y. Therefore, this gap closing does not result in a phase transition. The modes in those bands have a high Fermi velocity at zero energy and therefore a small ϕ_σ Zeeman phase shift that results in a weak dependence on the position of this cone on the strength of the in-plane field. Finally, since those bands always have a considerable electron polarization, the electrons can be transmitted through the system for both positive and negative energies. This is clearly visible in the map of Fig. 4(c), where we show the electron transmission coefficient. This effect in turn results in lack of sign change of the nonlocal conductance at zero

energy as it is for the cones that mark the topological/trivial transition.

B. Phase biasing by a perpendicular magnetic field

Phase biasing of the junction is achieved by placing the junction in a superconducting loop and threading the loop with a perpendicular magnetic field $B_\perp$ resulting in the magnetic flux $\Phi = B_\perp \pi R^2$, with R being the radius of the loop. Typically, those loops have significant inductance L [18,21] leading to nonlinear magnetic field to phase conversion governed by the equation

$$\phi = \frac{2\pi}{\Phi_0}\left(\Phi - L\sum_{\sigma=\pm1} I_\sigma(\phi)\right). \tag{4}$$

Typically the perpendicular field $B_\perp$ magnitude is a few orders lower than the magnitude of the in-plane field; therefore, one can consider that it does bring negligible effects in terms of Zeeman spin splitting. The Zeeman interaction due to the in-plane field nevertheless leads to the evolution of ABSs through the formula Eq. (3) and causes the modification of the supercurrent whose phase dependence at zero temperature for a junction embedding M spinful modes can be approximated as

$$I_\sigma(\phi) = \frac{e\Delta^2\tau M}{4\hbar}\frac{\sin(\phi+\varphi_\sigma)}{E_\sigma(\phi)}. \tag{5}$$

The $B_\perp$ to phase conversion obtained in the absence of the in-plane magnetic field B, where $\varphi_\sigma = 0$, is plotted with a thick curve in Fig. 5(a). The obtained dependency is strongly nonlinear due to the $LI(\phi)$ term in Eq. (4). Assuming a quasistatic approximation, for each value of $B_\perp$ we minimize $\varepsilon(\phi) = L[\sum_{\sigma=\pm1} I_\sigma(\phi)]^2/2 - M\sum_{\sigma=\pm1} E_\sigma(\phi)$ to obtain the phase difference that guarantees the ground state of our system. The result is a single-valued conversion curve $B_\perp$ to phase presented with a thin black line in Fig. 5(a). Here we take the parameters corresponding to the recent experiment [18], i.e., $M = 30$, $L = 321$ pH, $\tau = 0.99$, and $R = 4207$ nm.

Following the curve from the negative values of $B_\perp$ we observe phase slips close to the values $-\pi$ and π. As a result, regulating the phase difference by the perpendicular field allows one to obtain phase values only from certain regions [18], which actually omits the most desired values close to π. The Zeeman interaction leads to a splitting in the ABS structure, as seen in Fig. 2(a). As a result, the current jumps are less pronounced and no longer occur at $\pm\pi$—see the red dots in Fig. 5(a).

In Fig. 5(b) with blue dots we show the possible attainment of phase difference values versus the in-plane magnetic field. We indeed see that only at considerable Zeeman splitting energies it is possible to induce the π phase difference. In the same plot, we denote the analytical estimate of the phase values that guarantee the topological regime obtained from the analytical ABS spectrum as presented in Fig. 2(a). It is clear that, despite the topological gap opening at an already small parallel magnetic field at $\phi = \pi$ it is not possible to set the necessary phase bias to actually induce the topological phase. We observe that only a strong Zeeman interaction unveils the phase-difference region, close to $\pm\pi$—where the topological

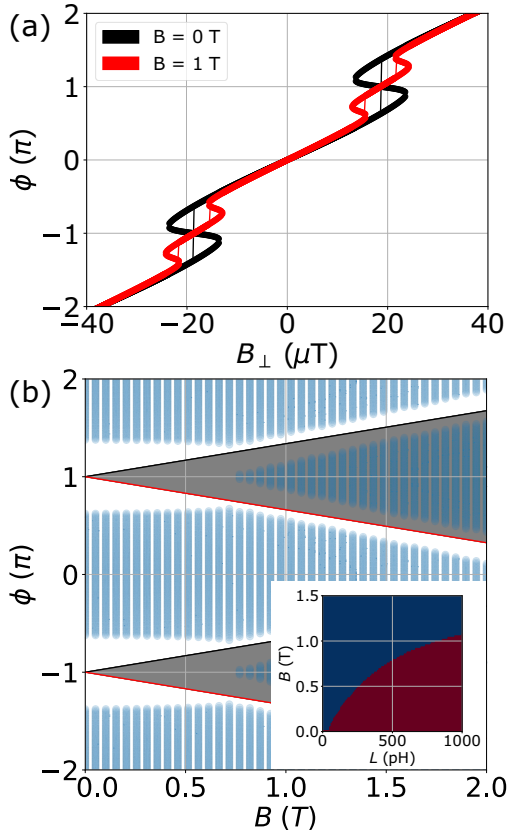

FIG. 5. (a) Plot of phase difference versus perpendicular field obtained without (black) and with (red) the in-plane field. The thick curves show the results without energy minimization and the thin lines correspond to the case of the energy minimization included. (b) The blue dots represent the feasible phase values that can be obtained by applying the perpendicular magnetic field $B_\perp$ for a given value of the in-plane field B. Gray areas, outlined by black and red lines, show the predicted [from the solution of Eq. (3)] phase-magnetic field range in which the topological regime is expected. The inset shows in red the parameter range in which the $\phi = \pi$ phase bias is available upon variation of the superconducting loop inductance.

superconductivity is present. This shows that the Zeeman interaction not only leads to the opening of the topological transition in the junction due to splitting of the ABS but also significantly modifies the flux-phase conversion that is necessary to bias the junction into the topological regime.

Finally, we study the case where the flux-phase conversion is calculated from a numerical spectrum of the junction instead of a simple approximation of Eq. (5). For each value of the in-plane field, we calculate numerically the spectrum of an isolated junction and then obtain the supercurrent $I(\varphi) = -\frac{e}{\hbar}\sum_{E_n>0}\frac{\partial E_n}{\partial\varphi}$. We then follow the same procedure of flux-to-phase conversion as described above. The results for three values of the in-plane field are shown in Figs. 6(a), 6(b) and 6(c). We see that only for a strong in-plane field is the linear flux to phase conversion restored with the possibility to bias the junction with π phase difference.

In Figs. 6(d), 6(e) and 6(f) we show nonlocal spectroscopy results versus the perpendicular field. We see that despite considering a transparent junction the probed ABS do not touch zero energy due to phase slips. Hence the topological

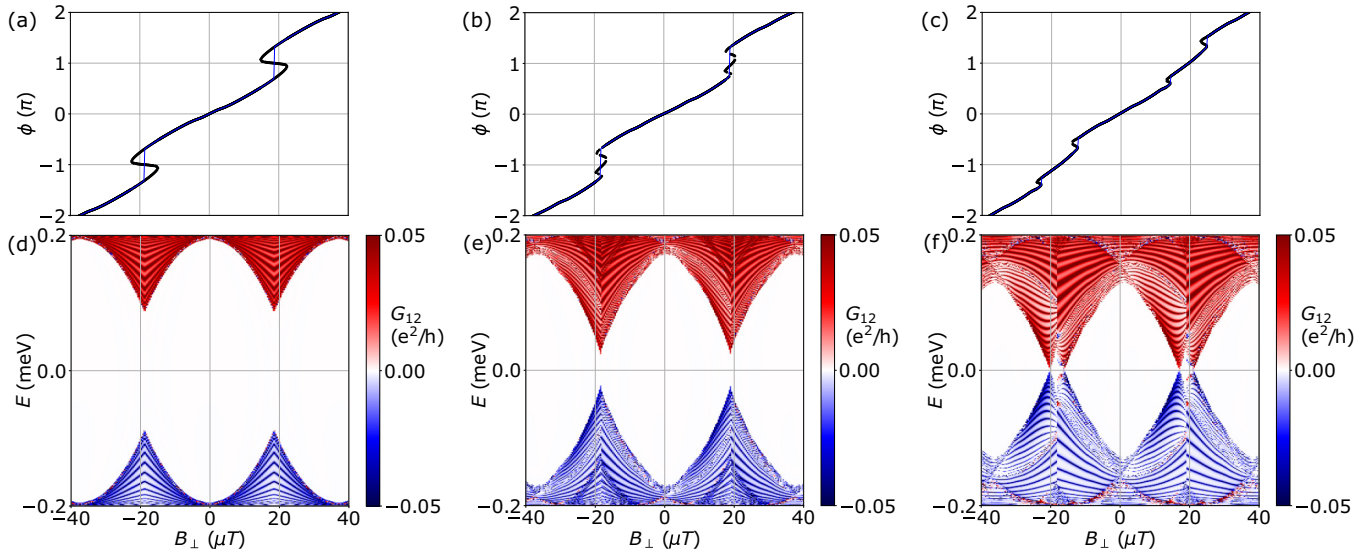

FIG. 6. (a),(b),(c) Perpendicular field to phase conversion obtained from numerical ABS spectrum for absent (a) parallel field and (b) 0.5 T and (c) 1 T. (d),(e),(f) Nonlocal tunneling spectroscopy results as a function of the perpendicular field used for phase biasing

region, although present in the spectra plotted against the phase difference in Fig. 2(a), is not present when we consider a realistic situation of flux-induced phase biasing. Only at considerable Zeeman interaction strength (here 1 T) is the transition between the trivial and topological regime visible as signified by the gap closing and reopening associated with the change of the sign of nonlocal conductance at zero energy [see Fig. 6(f)].

IV. DISCUSSION

We showed that, despite the fact that the phase bias can lower the critical Zeeman energy required for the topological transition [1], the phase biasing and specifically tuning the junction to $\phi = \pi$ configuration turns out to be difficult to perform in practice, and is in fact dependent on the microscopical parameters of the SNS junction (such as the supercurrent) and the device geometry itself (e.g., the superconducting loop size). Phase jumps as shown in Figs. 6(d) and 6(e) are actually visible in virtually every spectroscopic measurement of the ABS structure in planar junctions [17–21,27]. For instance, in the results of Ref. [18], upon closer examination of the energy phase relation, it was found that the measured Andreev bound states exhibit prominent cusps, a phenomenon not anticipated for transparent junctions. These cusps signify the occurrence of phase slips, which manifest themselves when the superconducting loop that embeds the junction possesses a substantial inductance. The phase slips in the experiment of Ref. [18] showed that it is possible to probe only a part of the ABS spectrum, which then affected the outcome of the measurement in a stronger *perpendicular field*, where the asymmetry in local spectroscopy measured from top and bottom was obtained. As these types of structures [17,18] are in principle to be used for nonlocal spectroscopy, the observed limited phase space probing represents a serious obstacle in probing the topological transition in them.

Let us discuss the conditions that will make it more favorable to bias the junction with phase π. Since it is the $LI(\phi)$ term that induces the nonlinearity of flux to phase conversion, one should consider limiting it to restore the possibility of realizing the π phase difference at small Zeeman fields. We approximate the condition under which increasing $B_\perp$ results in linear growth of the phase in the vicinity of the values of $\pi \pmod{2\pi}$ as when the second local maximum of $B_\perp(\phi)$ becomes larger than the first in each repeating 2π segment. For the case of $\tau \to 1$ we can analytically estimate the values of these two extrema, which leads to the condition

$$\varphi_\sigma + \frac{2\pi}{\Phi_0} L I_+(\pi + 2\varphi_\sigma) < 0, \tag{6}$$

where I_+ is half of the total current, assuming the same number of spin positive and spin negative modes. Solving it for L and $B_\perp$ yields the critical magnetic field at which π phase biasing becomes possible. We plot the resulting diagram in the inset of Fig. 5(b) where blue denotes the parameter range that allows one to obtain the phase bias π. We observe a rapid growth of the critical field with an increase in L. The inductance of the superconducting loop is typically dominated by the kinetic inductance $L = l\hbar R_0/w\pi\Delta$ [33], where l is the length, w is the width of the arm of the superconducting loop, and R_0 is normal state sheet resistance [21]. Therefore, smaller loops with wide arms could in principle be used to decrease the critical Zeeman field, which is necessary to phase bias the junction into the topological regime.

Limiting the current is typically less favorable because it requires either limiting the transparency of the junction by decreasing the mean free path or making the width of the junction (W_j) smaller, thus decreasing the number of ABS. The latter is again unfavorable because it induces overlap between Majorana modes, lifting their degeneracy, and would require usages of extended geometries [34,35]. An alternative approach could involve applying the gate voltage to the normal region of the junction, which in principle could decrease the number of ABS and therefore decrease the current in the junction [36].

V. SUMMARY AND CONCLUSIONS

In this theoretical study, we investigated the possibility of detection of the topological transition in a planar Josephson junction via the nonlocal spectroscopy technique. We showed that the topological transition that is associated with the fermion parity change which is controlled by the in-plane magnetic field and the phase difference in the junction results in a change of the sign of the nonlocal conductance at zero energy. We showed that this phenomenon is directly related to the change in the quasiparticle character of the bands and can be used to determine the topological transition in the transport measurements. As we showed, in a realistic situation the control of the phase bias in the junction is strongly dependent on the strength of the in-plane magnetic field as the Zeeman interaction controls the current-phase relation. This leads to the inability of scanning the entire phase space, specifically reaching the π bias required for topological transition at a small Zeeman interaction strength, unless the inductance of the superconducting loop embedding the junction or the current in the junction is considerably reduced.

ACKNOWLEDGMENTS

We acknowledge the stimulating discussions with S. Goswami, C. M. Moehle, P. K. Rout, and N. A. Jainandunsing. This work was supported by the National Science Center, Poland (NCN), Agreement No. UMO-2020/38/E/ST3/00418.

[1] F. Pientka, A. Keselman, E. Berg, A. Yacoby, A. Stern, and B. I. Halperin, Topological superconductivity in a planar Josephson junction, Phys. Rev. X **7**, 021032 (2017).

[2] M. Hell, M. Leijnse, and K. Flensberg, Two-dimensional platform for networks of Majorana bound states, Phys. Rev. Lett. **118**, 107701 (2017).

[3] M. Kjaergaard, F. Nichele, H. J. Suominen, M. P. Nowak, M. Wimmer, A. R. Akhmerov, J. A. Folk, K. Flensberg, J. Shabani, C. J. Palmstrøm, and C. M. Marcus, Quantized conductance doubling and hard gap in a two-dimensional semiconductor–superconductor heterostructure, Nat. Commun. **7**, 12841 (2016).

[4] H. J. Suominen, M. Kjaergaard, A. R. Hamilton, J. Shabani, C. J. Palmstrøm, C. M. Marcus, and F. Nichele, Zero-energy modes from coalescing Andreev states in a two-dimensional semiconductor-superconductor hybrid platform, Phys. Rev. Lett. **119**, 176805 (2017).

[5] C. M. Moehle, C. T. Ke, Q. Wang, C. Thomas, D. Xiao, S. Karwal, M. Lodari, V. van de Kerkhof, R. Termaat, G. C. Gardner, G. Scappucci, M. J. Manfra, and S. Goswami, Insbas two-dimensional electron gases as a platform for topological superconductivity, Nano Lett. **21**, 9990 (2021).

[6] H. Zhang, Ö. Gül, S. Conesa-Boj, M. P. Nowak, M. Wimmer, K. Zuo, V. Mourik, F. K. de Vries, J. van Veen, M. W. A. de Moor, J. D. S. Bommer, D. J. van Woerkom, D. Car, S. R. Plissard, E. P. Bakkers, M. Quintero-Pérez, M. C. Cassidy, S. Koelling, S. Goswami, K. Watanabe *et al.*, Ballistic superconductivity in semiconductor nanowires, Nat. Commun. **8**, 16025 (2017).

[7] V. Mourik, K. Zuo, S. M. Frolov, S. R. Plissard, E. P. A. M. Bakkers, and L. P. Kouwenhoven, Signatures of majorana fermions in hybrid superconductor-semiconductor nanowire devices, Science **336**, 1003 (2012).

[8] A. Das, Y. Ronen, Y. Most, Y. Oreg, M. Heiblum, and H. Shtrikman, Zero-bias peaks and splitting in an al–inas nanowire topological superconductor as a signature of majorana fermions, Nat. Phys. **8**, 887 (2012).

[9] M. T. Deng, C. L. Yu, G. Y. Huang, M. Larsson, P. Caroff, and H. Q. Xu, Anomalous zero-bias conductance peak in a nb–insb nanowire–nb hybrid device, Nano Lett. **12**, 6414 (2012).

[10] T. D. Stanescu and S. D. Sarma, Proximity-induced superconductivity generated by thin films: Effects of fermi surface mismatch and disorder in the superconductor, Phys. Rev. B **106**, 085429 (2022).

[11] H. Pan and S. D. Sarma, Physical mechanisms for zero-bias conductance peaks in Majorana nanowires, Phys. Rev. Res. **2**, 013377 (2020).

[12] H. Pan, C.-X. Liu, M. Wimmer, and S. D. Sarma, Quantized and unquantized zero-bias tunneling conductance peaks in majorana nanowires: Conductance below and above $2e^2/h$, Phys. Rev. B **103**, 214502 (2021).

[13] A. Vuik, B. Nijholt, A. R. Akhmerov, and M. Wimmer, Reproducing topological properties with quasi-Majorana states, SciPost Phys. **7**, 061 (2019).

[14] Y. Zhang, K. Guo, and J. Liu, Transport characterization of topological superconductivity in a planar Josephson junction, Phys. Rev. B **102**, 245403 (2020).

[15] B. H. Wu, S. A. Hassan, X. F. Xu, C. R. Wang, W. J. Gong, and J. C. Cao, Quantum transport of planar Josephson junctions with Majorana bound states, Phys. Rev. B **102**, 085414 (2020).

[16] S. Głodzik, N. Sedlmayr, and T. Domański, How to measure the Majorana polarization of a topological planar Josephson junction, Phys. Rev. B **102**, 085411 (2020).

[17] F. Nichele, E. Portolés, A. Fornieri, A. M. Whiticar, A. C. C. Drachmann, S. Gronin, T. Wang, G. C. Gardner, C. Thomas, A. T. Hatke, M. J. Manfra, and C. M. Marcus, Relating Andreev bound states and supercurrents in hybrid Josephson junctions, Phys. Rev. Lett. **124**, 226801 (2020).

[18] C. M. Moehle, P. K. Rout, N. A. Jainandunsing, D. Kuiri, C. T. Ke, D. Xiao, C. Thomas, M. J. Manfra, M. P. Nowak, and S. Goswami, Controlling andreev bound states with the magnetic vector potential, Nano Lett. **22**, 8601 (2022).

[19] A. Banerjee, M. Geier, M. A. Rahman, D. S. Sanchez, C. Thomas, T. Wang, M. J. Manfra, K. Flensberg, and C. M. Marcus, Control of Andreev bound states using superconducting phase texture, Phys. Rev. Lett. **130**, 116203 (2023).

[20] A. Fornieri, A. M. Whiticar, F. Setiawan, E. Portolés, A. C. C. Drachmann, A. Keselman, S. Gronin, C. Thomas, T. Wang, R. Kallaher, G. C. Gardner, E. Berg, M. J. Manfra, A. Stern, C. M. Marcus, and F. Nichele, Evidence of topological superconductivity in planar josephson junctions, Nature (London) **569**, 89 (2019).

[21] A. Banerjee, O. Lesser, M. A. Rahman, H.-R. Wang, M.-R. Li, A. Kringhøj, A. M. Whiticar, A. C. C. Drachmann, C. Thomas,

T. Wang, M. J. Manfra, E. Berg, Y. Oreg, A. Stern, and C. M. Marcus, Signatures of a topological phase transition in a planar Josephson junction, Phys. Rev. B **107**, 245304 (2023).

[22] S. M. Frolov, P. Zhang, B. Zhang, Y. Jiang, S. Byard, S. R. Mudi, J. Chen, A. H. Chen, M. Hocevar, M. Gupta, C. Riggert, and V. S. Pribiag, "Smoking gun" signatures of topological milestones in trivial materials by measurement fine-tuning and data postselection, arXiv:2309.09368 [cond-mat.mes-hall].

[23] D. I. Pikulin, B. van Heck, T. Karzig, E. A. Martinez, B. Nijholt, T. Laeven, G. W. Winkler, J. D. Watson, S. Heedt, M. Temurhan, V. Svidenko, R. M. Lutchyn, M. Thomas, G. de Lange, L. Casparis, and C. Nayak, Protocol to identify a topological superconducting phase in a three-terminal device, arXiv:2103.12217 [cond-mat.mes-hall].

[24] J.-Y. Wang, N. van Loo, G. P. Mazur, V. Levajac, F. K. Malinowski, M. Lemang, F. Borsoi, G. Badawy, S. Gazibegovic, E. P. A. M. Bakkers, M. Quintero-Pérez, S. Heedt, and L. P. Kouwenhoven, Parametric exploration of zero-energy modes in three-terminal InSb-Al nanowire devices, Phys. Rev. B **106**, 075306 (2022).

[25] H. Pan, J. D. Sau, and S. D. Sarma, Three-terminal nonlocal conductance in Majorana nanowires: Distinguishing topological and trivial in realistic systems with disorder and inhomogeneous potential, Phys. Rev. B **103**, 014513 (2021).

[26] T. O. Rosdahl, A. Vuik, M. Kjaergaard, and A. R. Akhmerov, Andreev rectifier: A nonlocal conductance signature of topological phase transitions, Phys. Rev. B **97**, 045421 (2018).

[27] A. Banerjee, O. Lesser, M. A. Rahman, C. Thomas, T. Wang, M. J. Manfra, E. Berg, Y. Oreg, A. Stern, and C. M. Marcus, Local and nonlocal transport spectroscopy in planar Josephson junctions, Phys. Rev. Lett. **130**, 096202 (2023).

[28] N. A. Mortensen, K. Flensberg, and A.-P. Jauho, Angle dependence of Andreev scattering at semiconductor–superconductor interfaces, Phys. Rev. B **59**, 10176 (1999).

[29] D. Sticlet, B. Nijholt, and A. Akhmerov, Robustness of Majorana bound states in the short-junction limit, Phys. Rev. B **95**, 115421 (2017).

[30] D. Kuiri and M. P. Nowak, Non-local transport signatures of topological superconductivity in a phase-biased planar Josephson junction - code, Zenodo (2023), doi:10.5281/zenodo.8086328.

[31] C. W. Groth, M. Wimmer, A. R. Akhmerov, and X. Waintal, Kwant: a software package for quantum transport, New J. Phys. **16**, 063065 (2014).

[32] For the calculation of the eigenspectrum of the junction we replace the semi-infinite superconducting leads with finite segments of superconductor of the length 2000 nm larger than the estimated coherence length 1166 nm.

[33] A. J. Annunziata, D. F. Santavicca, L. Frunzio, G. Catelani, M. J. Rooks, A. Frydman, and D. E. Prober, Tunable superconducting nanoinductors, Nanotechnology **21**, 445202 (2010).

[34] T. Laeven, B. Nijholt, M. Wimmer, and A. R. Akhmerov, Enhanced proximity effect in zigzag-shaped Majorana Josephson junctions, Phys. Rev. Lett. **125**, 086802 (2020).

[35] P. P. Paudel, T. Cole, B. D. Woods, and T. D. Stanescu, Enhanced topological superconductivity in spatially modulated planar Josephson junctions, Phys. Rev. B **104**, 155428 (2021).

[36] P. K. Rout (private communication).

Chapter 7

Enhancement of the topological regime in elongated Josephson junctions

DOI: 10.1103/PhysRevB.111.085416

Enhancement of the topological regime in elongated Josephson junctions

D. Kuiri [1,*] P. Wójcik [2,†] and M. P. Nowak [1,‡]

[1] *AGH University of Krakow, Academic Centre for Materials and Nanotechnology, al. A. Mickiewicza 30, 30-059 Krakow, Poland*

[2] *AGH University of Krakow, Faculty of Physics and Applied Computer Science, al. A. Mickiewicza 30, 30-059 Krakow, Poland*

(Received 13 September 2024; revised 22 January 2025; accepted 27 January 2025; published 13 February 2025)

We theoretically study topological superconductivity in elongated planar Josephson junctions. In the presence of spin-orbit coupling and an in-plane magnetic field, the Josephson junction can enter the topological phase and host zero-energy Majorana bound states over a range of the superconducting phase difference centered around π, with the span of this range determined by the strength of the magnetic field. We demonstrate that the topological superconducting phase range can be greatly increased by elongation of the junction, which causes an amplification of the Zeeman-induced phase shift of Andreev bound states. We show that the appearance of trivial in-gap states that occurs in elongated junctions can prohibit the creation of Majorana modes, but it can be mitigated by further proximitization of the junction with additional superconducting contacts. The topological transition in this system can be probed by measurements of the critical current and we show that the elongation of the junction leads to a linear decrease of the transition critical magnetic field beneficial for experimental studies.

DOI: 10.1103/PhysRevB.111.085416

I. INTRODUCTION

Planar superconductor-normal-superconductor (SNS) junctions have emerged as promising platforms for studying topological superconductivity as they combine necessary spin interactions such as Rashba spin-orbit coupling, a strong Zeeman interaction [provided by the semiconducting normal part typically realized in InAs, InSbAs [1–8] two-dimensional electron gases (2DEG)] accompanied by the extended tunability of the system band structure through the variation of the superconducting phase difference ϕ between the two superconducting contacts [9,10]. Typically, in hybrid SNS junctions, a superconducting gap with a value similar to that of the parent superconductor is opened by proximitizing 2DEG by a conventional superconductor such as Al [11].

Experiments aimed at the realization of topological superconductivity look for zero-energy Majorana bound states (MBS) that appear at junction edges in the topological phase [10]. Typically, tunneling spectroscopy is used to explore the presence of zero-bias conductance peaks [3,5], their correlation at the two edges of the system, or a nonlocal signal characterizing the closing and reopening of the gap [12,13]. The system can be tuned in or out from the topological regime mainly by two experimentally accessible knobs: the strength of the Zeeman interaction, which is controlled by the in-plane magnetic field magnitude and by the superconducting phase difference. The latter is induced by embedding the junction in a large superconducting loop, which is threaded by a magnetic flux [5,8]. This method inconveniently suffers from nonzero loop inductance, which translates into phase jumps [13,14] that prevent accessing of the $\phi = \pi$ region, where the MBS form. This in consequence results in the need for MBS to be present in a large phase range, which in turn requires large in-plane magnetic fields. This denies the original feature of the topological SNS junctions, which is the possibility of achieving the topological phase at small magnetic fields [9]. The strong Zeeman interaction in hybrid SNS systems leads to the appearance of an abundance of trivial in-gap states [6,15], reduces the induced gap, and the required considerable magnetic field closes the superconducting gap of parent low-critical-field superconductors, such as Al.

In this paper, we show that the topological regime in the SNS junction can be greatly extended by elongating the junction. However, this comes with a caveat: the formation of transverse modes located in the normal part of the junction, which quickly close the induced gap and destroy the MBS. We propose a way to overcome this problem by further proximitization of the normal region by two superconducting contacts. This kind of configuration has been considered in the context of multiterminal Josephson junctions [16–23] that have been studied in terms of quasiparticle quartets [24–26], Cooper pair splitters [27], and superconducting diode effect [28–30]. We show that the topological phase span in the superconducting phase space is linearly dependent on the junction length and that the topological transition can be probed via critical current measurement [9,14,31–33], which also benefits from the enhancement of the topological regime with a linear decrease of the critical magnetic field with junction elongation.

II. PROOF OF CONCEPT

For a perfectly transparent junction the two spin Andreev bound states (ABS) components, dependent on the superconducting gap difference ϕ, can be described by formula $E_\sigma(\phi) = \pm\Delta|\cos[(\phi/2 + \varphi_\sigma)]|$, where

*Contact author: kuiri@agh.edu.pl
†Contact author: pawel.wojcik@fis.agh.edu.pl
‡Contact author: mpnowak@agh.edu.pl

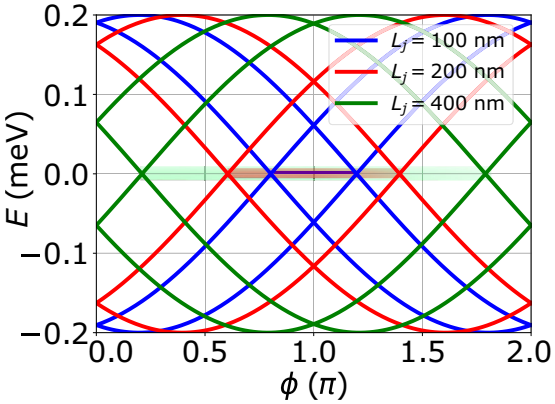

FIG. 1. Schematic energy-phase relation of an SNS junction under the Zeeman effect. The blue, red, and green curves show ABS energies for the same magnetic field strength ($B = 0.5$ T) but with an increase in the junction length. The topological regime opens around $\phi = \pi$ with MBS appearing at zero energy (denoted with light lines) and its phase span increases as the junction is elongated.

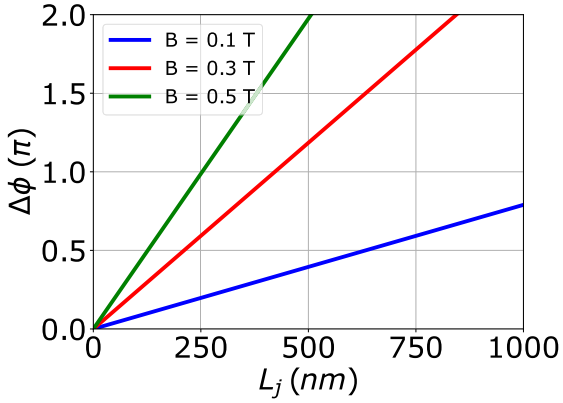

FIG. 2. The phase span of the topological regime versus the length of the junction for three values of the magnetic field.

$\varphi_\sigma = \sigma E_z L_j/\hbar v_F$, $E_z = g\mu_B B/2$ is the Zeeman energy, $\sigma = \pm 1$ corresponds to positive and negative spin components and $v_F = \sqrt{2\mu/m^*}$ is the Fermi velocity [34–36]. In the calculation of the phase shift we omit the effect of the spin-orbit coupling to the Fermi velocity [36] as it is small compared to the chemical potential term and has a negligible impact on the obtained results. Here we use $\mu = 5$ meV, $m^* = 0.014m_e$, $\Delta = 0.2$ meV, and $g = 50$ as typical parameters for the InSb SNS junctions [8]. As follows from the formula, in the absence of the Zeeman interaction, the ABS energy spectrum is twofold degenerate. The Zeeman interaction splits the degeneracy and moves apart in phase two branches of ABS states (see the blue curves in Fig. 1). Between the two branches, around $\phi = \pi$, where the fermion parity is odd, the topological regime emerges, and two MBS are formed at the edges of the junction. Their zero-energy levels are schematically indicated by faint lines in Fig. 1.

Crucially, we see that the phase shift of the ABS is proportional to the length of the junction L_j—the distance between the superconducting electrodes. In fact, in Fig. 1 we see that the region in which MBS are present is greatly increased when the length of the junction is extended. We can see that for $L_j = 400$ nm, MBS appear in almost the entire phase region, while for $L_j = 100$ nm they are present only in the small region around $\phi = \pi$, which can prevent it from being experimentally reached in flux-induced phase-biased Josephson junctions [13].

The size of the odd-parity phase region, which is denoted by the faint lines at zero energy in Fig. 1, $\Delta\phi = |\phi_+ - \phi_-|$ is determined by the positive and negative roots of $E_\sigma = 0$ given by $\phi_\pm = \pm\chi BL_j + \pi(1 + 2n)$, where $n \in \mathbb{Z}$, resulting in $\Delta\phi = |2\chi BL_j|$ with $\chi = g\mu_B/\hbar v_F$. In Fig. 2 we show the linear increase in the topological phase span with increasing junction length with the tilt determined by the magnetic field value. It should be noted that the increase of the length of the junction at a given magnetic field can lead to a situation where the topological phase covers the full 2π phase region with MBS appearing even at $\phi = 0$ in accordance with the phase diagram shown in Ref. [9].

In the following sections, we discuss the theoretical framework, numerical simulations, and results that support the proposed idea.

III. RESULTS

A. Induced gap—Green's function model

First, we study the dispersion relation of an SNS junction to understand the effect of the elongation of the junction on the induced gap. We consider a finite system along the superconductor-normal-superconductor direction (x) and translation-invariant along the perpendicular direction with a well-defined momentum k_y. The SNS junction consists of two S segments corresponding to a proximitized semiconductor flanking a normal (N) semiconducting region [37]. The system is described by the Hamiltonian,

$$H_0 = \left(\frac{\hbar^2 k_x^2}{2m^*} + \frac{\hbar^2 k_y^2}{2m_\parallel^*} - \mu\right)\sigma_0 \otimes \tau_z + \frac{1}{2} g\mu_B B_y \sigma_y \otimes \tau_0 + \alpha(x)(\sigma_x k_y - \sigma_y k_x) \otimes \tau_z \quad (1)$$

written in Nambu basis $\Psi^T = (\psi_{e\uparrow}, \psi_{h\downarrow}, \psi_{e\downarrow}, -\psi_{h\uparrow})$ that represents the electron (e) or hole (h) components with spin up ($\uparrow$) or down ($\downarrow$). $k_x = -\imath\partial/\partial x$, k_y is a good quantum number, σ_i and τ_i with $i = x, y, z$ are the Pauli matrices acting on spin and electron-hole degree of freedom, respectively. The magnetic field and spin-orbit coupling are included only in the normal part of the junction.

The excitations of the system are obtained from the system Green's function [38–40]

$$G^{-1}(w) = w - H_0 - \sum(w), \quad (2)$$

where

$$\sum(w) = -\gamma\left[\frac{\omega\sigma_0 \otimes \sigma_0 + \Delta(x)\tau_+ + \Delta^*(x)\tau_-}{\sqrt{\Delta(x)^2 - \omega^2}}\right], \quad (3)$$

is a self-energy resulting from the uniform coupling of the system to the superconductor [38,39] with the pairing term

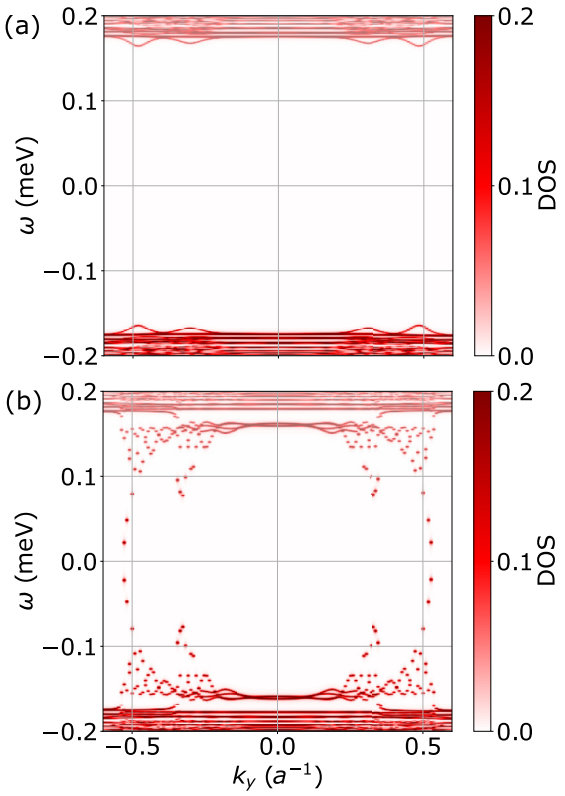

FIG. 3. Density of states of a junction invariant along the NS interface as a function of transverse momentum k_y for the junction length (a) $L_j = 100$ nm and (b) $L_j = 500$ nm for $\phi = 0$ and $B = 0$.

given by

$$\Delta(x) = \begin{cases} \Delta_0 & \text{if} \quad x < -L_j/2 \\ 0 & \text{if} \quad |x| \leqslant L_j/2 \\ \Delta_0 e^{i\phi} & \text{if} \quad x > L_j/2 \end{cases}, \tag{4}$$

which corresponds to a 2DEG proximitized by two superconducting segments placed on top of the heterostructure [1–7]. Equation (3) is applicable to energies within the superconducting gap, $|\omega| < \Delta_0$. The density of states is calculated based on the formula $\rho(\omega) = -\frac{1}{\pi}\mathrm{Im}[G(w)]$ [41], where we adopt the parameters that correspond to the InSb semiconductor and the Al superconductor with $m^* = 0.014m_e$, $\mu = 5$ meV, $\Delta_0 = 0.2$ meV, $\alpha = 50$ meV nm and $\gamma = 0.7$ meV that controls the coupling between the superconductor and the parent semiconductor.

We discretize the Hamiltonian on a square lattice with a lattice spacing of $a = 10$ nm and replace superconducting (proximitized) contacts with finite segments with lengths that exceed the coherence length (estimated to be $\xi \simeq 1$ μm), with $L_{\mathrm{SC}} = 2$ μm. Since in our calculation we use a uniform chemical potential, for a proper description of Andreev scattering at the NS interface [42], we introduce an anisotropic mass in the proximitized contacts with the effective mass in the direction parallel to the interface $m^*_{\parallel} = 1000m^*$ [43]. The results were obtained in part with the use of the KWANT package [44] and the numerical code behind the calculations is available in an online repository [45].

In Fig. 3 we show the calculated densities of states versus ω and k_y that visualize the junction spectrum for $L_j = 100$ nm (a) and $L_j = 500$ nm (b) at zero magnetic field and $\phi = 0$. We observe the appearance of an induced gap with magnitude close to 200 μeV and an abundance of quasiparticle bands outside the gap that originate from the wide superconductors. In contrast to the $L_j = 100$ nm results [Fig. 3(a)], where the gap is opened in the whole Brillouin zone, for $L_j = 500$ nm [Fig. 3(b)] there are a great number of states with large momenta k_y localized within the induced gap. As we shall see, those states that appear upon elongation of the junction constitute an obstacle in enhancing the topological gap by elongation of the junction in the simple two-terminal SNS geometry.

B. Integrated superconductivity

For further analysis of the in-gap states and to numerically approach finite junctions with realistic sizes, determined by the junction length L_j and width W_j (the size of the junction along the superconducting contacts), in the next step we move on to a less numerically demanding model, where the induced superconductivity is integrated into the regions surrounding the normal part of the junction [12,13].

The system Hamiltonian becomes

$$H = \left(\frac{\hbar^2 k_x^2}{2m^*} + \frac{\hbar^2 k_y^2}{2m^*} - \mu\right)\sigma_0 \otimes \tau_z + \frac{1}{2}g(x)\mu_B B\sigma_y \otimes \tau_0 + \alpha(x)(\sigma_x k_y - \sigma_y k_x) \otimes \tau_z + \Delta(x)\tau_+ + \Delta^*(x)\tau_- \tag{5}$$

with $\tau_\pm = (\tau_x \pm \imath\tau_y)/2$ and $\tau_x = \sigma_0 \otimes \sigma_x$, $\tau_y = \sigma_0 \otimes \sigma_y$.

The Hamiltonian is discretized on a square mesh with lattice constant $a = 10$ nm. All the system parameters remain the same as in the former section.

First, we consider a translational invariant system as in the section above. In Fig. 4 we show two dispersion relations for a system with $L_j = 100$ nm (a) and $L_j = 500$ nm (b). As previously, we observe appearance of in-gap states for the elongated junction, which justifies the application of the integrated superconductivity approximation. In Fig. 4 the colors denote the weight of the wave function localized in the normal region of the junction calculated as $W_N = \int_{-L_j/2}^{L_j/2} |\Psi(x, k_y)|^2 dx$. For $L_j = 100$ nm, we observe a pronounced superconducting gap open for all k_y values. The bands with the energies outside the induced gap correspond to the quasiparticle states residing mostly in the superconducting leads with small W_N values denoted by a dark blue color. The situation is strikingly different in the elongated junction whose spectrum we plot in Fig. 4(b). Here, the gap closes for larger k_y values with modes that reside mainly in the normal part of the junction with pronounced W_N values.

The presence of these high k_y in-gap states has immediate consequences for the ABS structure of the finite-size SNS which we show in Fig. 5. Here, the junction length L_j is 100 nm (a) and 500 nm (b) with the width of the systems $W_j = 2000$ nm. In Fig. 5(a), we see that the spectrum consists of two spin-split branches of ABS and, between them, a small region with zero-energy states corresponding to MBS in accordance with the proof-of-concept model of Fig. 1. The situation for the elongated junction depicted in Fig. 5(b) is

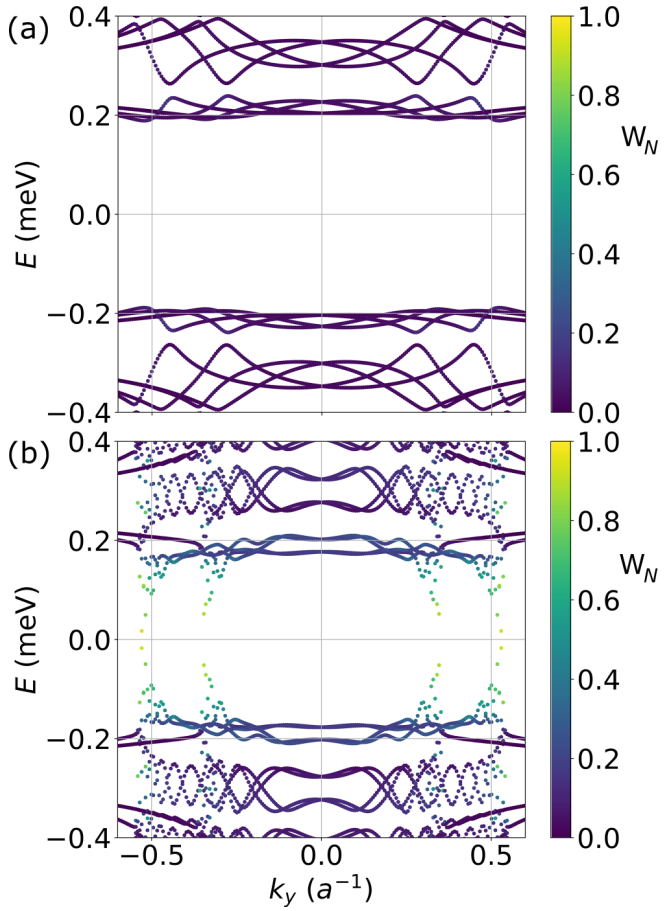

FIG. 4. Dispersion relation for translational-invariant SNS junction for (a) $L_j = 100$ nm and the (b) $L_j = 500$ nm. The colors denote W_N, the weight of the wave function localized in the normal region.

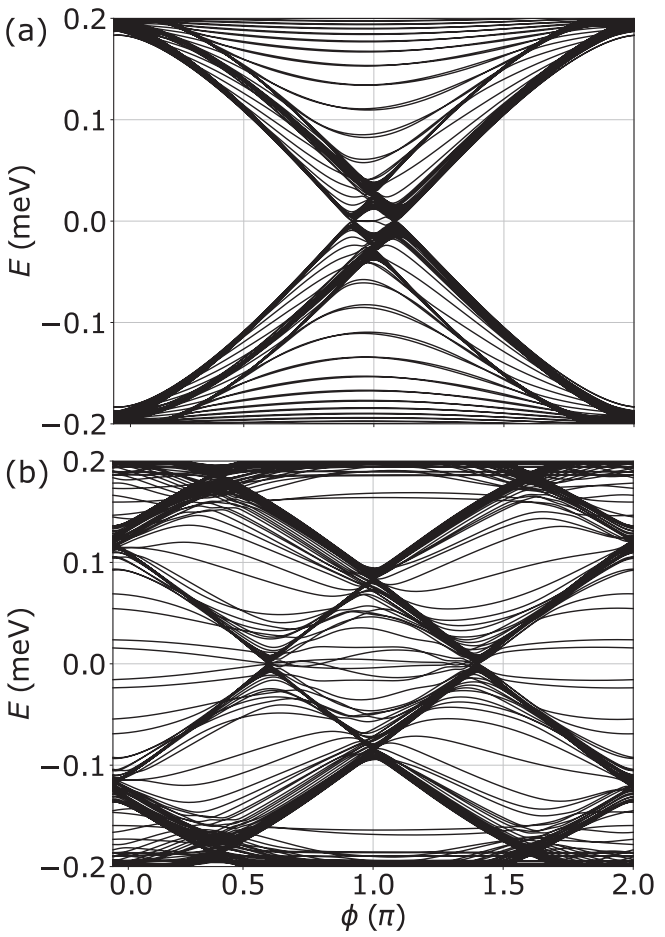

FIG. 5. ABS energies versus the superconducting phase difference for a finite-size SNS junction with the length (a) $L_j = 100$ nm and (b) $L_j = 500$ nm. The result are obtained for $B = 0.2$ T and the width of the junction $W_j = 2000$ nm.

starkly different. We again observe two spin-split branches, this time with much larger splitting due to the amplification of the Zeeman effect discussed earlier. However, in the spectrum, there is an abundance of in-gap states whose energies are nearly phase independent. This is in line with the results of Fig. 4(b) where we saw that the in-gap modes are localized mostly in the normal region and therefore they are weakly affected by change of the phase difference in the nearby superconducting leads. Crucially, those states, mostly localized in the normal regime, couple the two junction edges, making it impossible to form the MBS, which is accompanied by a lack of zero-energy states and a lack of visible induced gap in the topological phase.

C. Proximitizing the in-gap modes

Recently, it has been proposed that a zigzag configuration could help mitigate the adverse effects caused by the in-gap modes [46]. Here we propose a different strategy which is simpler in terms of the required precision in shaping the superconducting contacts and also avoids the limit of the zigzag junction length set by reopening the straight paths when the separation between the superconductors increases—important in the context of the enhancement of the topological regime.

Since the in-gap modes have large momenta parallel to the superconducting interfaces and are localized mainly in the normal region, they correspond to quasiparticles traveling between the normal edges of the junction. Hence, we place two additional superconducting contacts at the top and bottom edges of the junction [see Fig. 6(b)] that force Andreev reflections of the vertically propagating quasiparticles, which in turn leads to the reopening of the induced gap. We assume the same superconducting gap value in the top and bottom contacts as in the left and right leads (with the phase $\phi = 0$), and the length of 2000 nm that exceeds the value of the superconducting coherence length.

Induced proximitization of the in-gap modes has direct consequences for the ABS spectrum of the junction. In Fig. 6(a) we plot the eigenspectrum of the junction and observe the removal of phase-independent ABS states appearing with energies $|E| < 0.1$ meV in Fig. 5(b). Most importantly, the lack of localized states spreading in the bulk of the normal region allows now for creation of zero-energy modes which correspond to spatially delocalized MBS whose probability density we plot with blue color in Fig. 6(b). It is worth mentioning that the superconducting phase difference, which is implied by setting $\phi \neq 0$ on the right terminal, also breaks the inversion symmetry with respect to $x = 0$ and causes a nonsymmetric localization of the MBS at the corners of the junction.

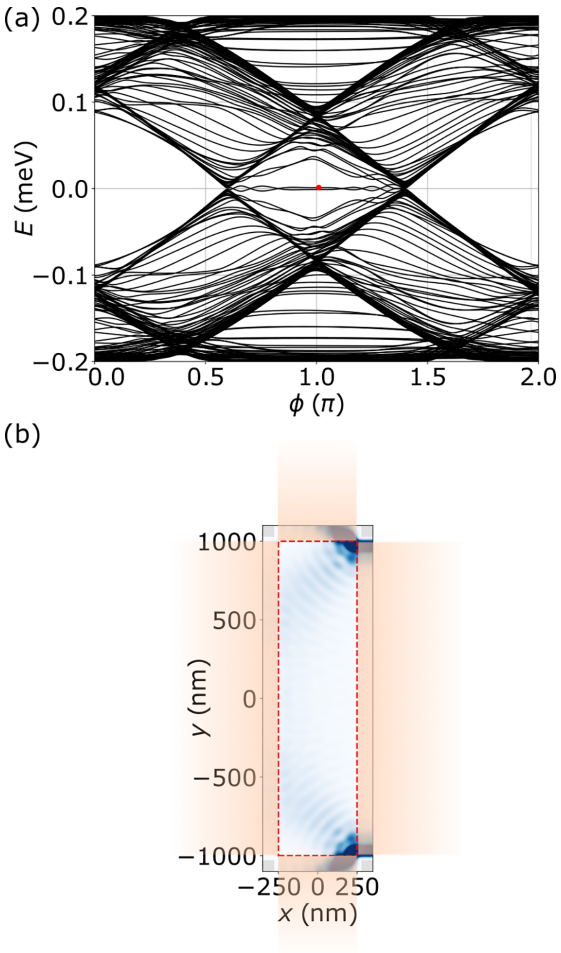

FIG. 6. (a) ABS spectrum for an elongated junction with the length $L_j = 500$ nm for $B = 0.2$ T with extra two superconducting contacts at the bottom and the top of the junction. (b) Scheme of the extended junction with both left and right and top and bottom superconducting contacts (orange). The blue color map represents the probability density for the MBS denoted with the red dot in (a).

The elongation of the junction eventually leads to a situation in which the junction length becomes comparable to the superconducting coherence length. In this situation, the ABS structure undergoes a transition, adopting a linear configuration [47]. In Fig. 7 we show the spectrum of a junction of length $L_j = 1000$ nm $\simeq \xi$. We observe a pronounced topological gap open in the system, and the presence of nearly-degenerate zero energy state almost in the entire phase range despite the small magnetic field value of $B = 0.2$ T, compatible with the prediction of Fig. 1.

D. Possible measurement of topological transition

The presence of the top and bottom superconducting electrodes prohibits performing local [1,3] or nonlocal [12,13] tunneling spectroscopy to probe the ABS structure and the closing and reopening of the gap. However, the topological transition in the ground state of the junction can be investigated by tracing the critical current of the junction $I_c = \max_\phi I(\phi)$ (with $I(\phi) = -\frac{e}{\hbar}\sum_{E_i>0}\frac{\partial E_i}{\partial \phi}$) in an external magnetic field [9]. E_i are either obtained as eigenvalues of

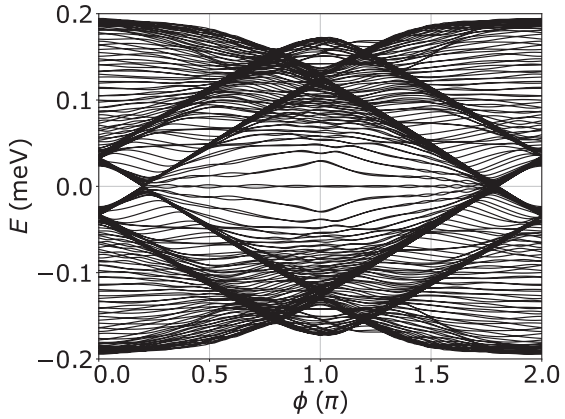

FIG. 7. ABS spectrum for a junction of length $L_j = 1000$ nm and $B = 0.2$ T.

the Hamiltonian Eq. (5) or for the case of analytical approach are calculated by taking $\sum E_i(\phi) = E_+(\phi) + E_-(\phi)$ from the model of Sec. II with the resulting current scaled to be comparable to the one obtained numerically. The numerical results are obtained for the junction with the top and bottom superconducting contacts attached.

In Fig. 8 we show with red solid lines the critical current and with blue solid lines the ground-state phase ϕ_{GS} which results in the minimization of the SNS junction energy calculated as the sum over energies of ABS states $E_j(\phi) = \sum_{E_i<0} E_i(\phi)$. We see that as the critical current reaches the minimum, the ground state of the junction switches from the trivial regime (with a phase difference close to 0) to the topological regime (with the phase difference π). Crucially, the switching magnetic field is greatly reduced in the elongated junction, as can be seen comparing the panel (a) obtained for $L_j = 100$ nm with Fig. 8(b) calculated for $L_j = 500$ nm. In the same figure with dashed lines we show the ground-state phase and the critical current obtained from the analytical model for ABS spectrum of Fig. 1.

Moreover, from the analytical model for the Zeeman-split ABS we can estimate the magnetic field at which the junction switches its ground-state phase, which occurs at $\sum_\sigma \Delta|\cos(\varphi_\sigma)| = \sum_\sigma \Delta|\cos(\pi/2 + \varphi_\sigma)|$ as

$$B_c = n\frac{hv_f}{4L_j g\mu_B}, \tag{6}$$

with $n \in \mathbb{Z}$ as previously considered for Zeeman-driven Fulde-Ferrell-Larkin-Ovchinnikov-like mechanism that through a spatial variation of the superconducting pairing leads to a minimum in the critical current [14,48]. We see that the linear scaling of the span of the topological region is translated into a linear decrease of the critical field necessary to achieve the topological phase when probing the junction by the critical field.

IV. DISCUSSION

The typical length of the junctions studied experimentally so far was around 100 nm [1–6,8], while the measured mean free path was reported to be 600 nm for InAs systems [2–5], suggesting that the junction length could be increased

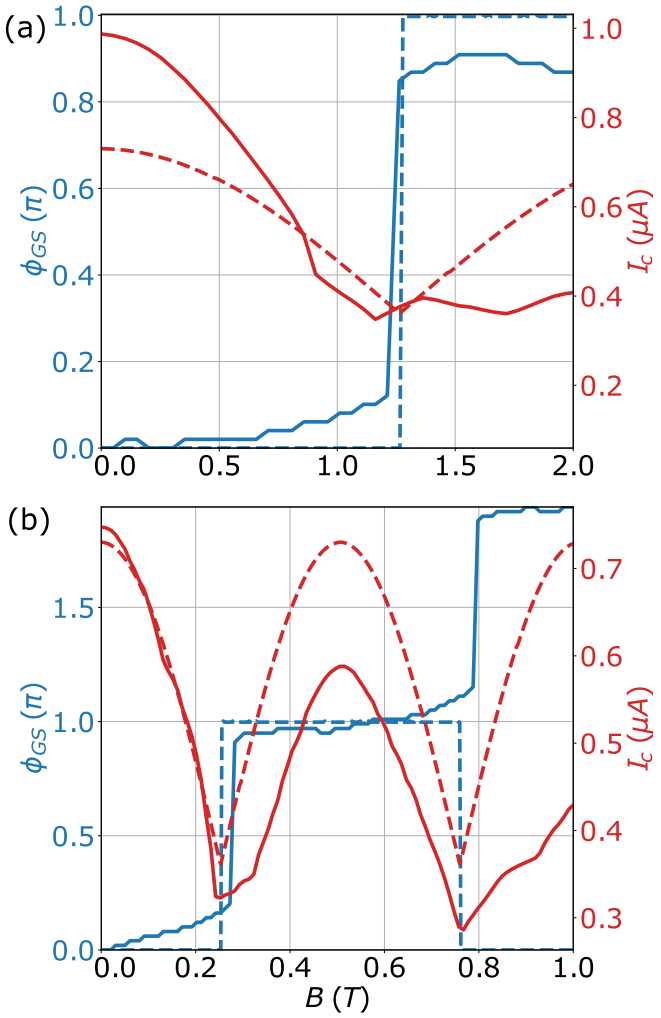

FIG. 8. Superconducting phase difference leading to the ground-state of the junction (blue) and critical current of the junction (red curves), showing minima at phase transitions. The results are obtained for junctions with length (a) $L_j = 100$ nm and (b) $L_j = 500$ nm. Solid lines represent numerical calculations, while dashed lines correspond to analytical results.

several times without reducing its transparency significantly and allowing for a several-times increase in the span of the topological region and multiple reductions of the critical magnetic field for the topological transition probed by the critical current. Another possible limit in the achievable junction length is the phase coherence length. However, it is typically much larger than the mean free path as found experimentally for these kinds of heterostructures [7,49,50], so whenever the junction is clean enough so that the mean free path is longer than the length of the junction, the phase coherence should not be a constraint.

It is also worth comparing the junction length with another length scale present in those systems, namely the spin-orbit coupling length $l_{SO} = \hbar^2/m^*\alpha$, which for the Rashba-type interaction, to some extent can be controlled by gating the system. For considered here $\alpha = 50$ meV nm $l_{SO} = 109$ nm and clearly, the junction length exceeds l_{SO}, yet the topological phase is fully developed. We have verified that increasing the spin-orbit coupling strength up to 100 meV nm results in a minimal variation of the energy structure, suggesting that the spin-orbit length does not impose a constraint on L_j. It specifically does not affect the topological transition points. This is also expected in analogy to a single superconductor system (such as a nanowire proximitized by a superconducting shell) where the topological transition criterion is $E_z^2 > \Delta^2 + \mu^2$ and does not include the spin-orbit coupling term. It is rather expected that the strength of the spin-orbit interaction affects the spatial extent of the Majorana bound state such that for the systems with stronger spin-orbit coupling the Majorana bound state coherence length decreases [51], therefore systems with stronger spin-orbit interactions would be desirable in terms of realization of topological Josephson junctions with limited width (the span in y direction).

V. SUMMARY AND CONCLUSIONS

We studied topological superconductivity in elongated planar Josephson junctions. We showed that the increase of the separation between the superconducting contacts causes the amplification of the Zeeman effect affecting the Andreev bound-state spectrum. As the junction becomes longer, at a constant magnetic field, the phase separation between the Andreev bound states increases, extending the phase-span of the topological region. However, as the length increases the junction also becomes populated with trivial in-gap states which prohibit creation of Majorana bound states. We show that those in-gap states can be removed from the spectrum by further proximitizing the junction with two additional superconducting contacts, which restores the topological gap and edge-mode Majorana states. Our numerical study complemented with an analytical model shows that the amplification of the phase-span of the topological regime linearly depends on the junction length. We show that the topological transition can be probed by critical current measurement which also benefits from linear reduction of the critical field, at which the transition occurs as the length of the junction is increased. Furthermore, the presence of Majorana edge modes can be further verified in this type of system by local probing of the density of states [52] or the spin structure of the edge modes [53].

ACKNOWLEDGMENTS

This work was supported by the National Science Center (NCN) Agreement No. UMO-2020/38/E/ST3/00418. We gratefully acknowledge Polish high-performance computing infrastructure PLGrid (HPC Center: ACK Cyfronet AGH) for providing computer facilities and support within computational Grant No. PLG/2024/017374.

[1] F. Nichele, E. Portolés, A. Fornieri, A. M. Whiticar, A. C. C. Drachmann, S. Gronin, T. Wang, G. C. Gardner, C. Thomas, A. T. Hatke, M. J. Manfra, and C. M. Marcus, Relating Andreev bound states and supercurrents in hybrid Josephson junctions, Phys. Rev. Lett. **124**, 226801 (2020).

[2] A. Banerjee, M. Geier, M. A. Rahman, D. S. Sanchez, C. Thomas, T. Wang, M. J. Manfra, K. Flensberg, and C. M. Marcus, Control of Andreev bound states using superconducting phase texture, Phys. Rev. Lett. **130**, 116203 (2023).

[3] A. Fornieri, A. M. Whiticar, F. Setiawan, E. Portolés, A. C. C. Drachmann, A. Keselman, S. Gronin, C. Thomas, T. Wang, R. Kallaher, G. C. Gardner, E. Berg, M. J. Manfra, A. Stern, C. M. Marcus, and F. Nichele, Evidence of topological superconductivity in planar Josephson junctions, Nature (London) **569**, 89 (2019).

[4] A. Banerjee, O. Lesser, M. A. Rahman, C. Thomas, T. Wang, M. J. Manfra, E. Berg, Y. Oreg, A. Stern, and C. M. Marcus, Local and nonlocal transport spectroscopy in planar Josephson junctions, Phys. Rev. Lett. **130**, 096202 (2023).

[5] A. Banerjee, O. Lesser, M. A. Rahman, H.-R. Wang, M.-R. Li, A. Kringhøj, A. M. Whiticar, A. C. C. Drachmann, C. Thomas, T. Wang, M. J. Manfra, E. Berg, Y. Oreg, A. Stern, and C. M. Marcus, Signatures of a topological phase transition in a planar Josephson junction, Phys. Rev. B **107**, 245304 (2023).

[6] C. M. Moehle, C. T. Ke, Q. Wang, C. Thomas, D. Xiao, S. Karwal, M. Lodari, V. van de Kerkhof, R. Termaat, G. C. Gardner, G. Scappucci, M. J. Manfra, and S. Goswami, InSbAs two-dimensional electron gases as a platform for topological superconductivity, Nano Lett. **21**, 9990 (2021).

[7] J. Shabani, M. Kjaergaard, H. J. Suominen, Y. Kim, F. Nichele, K. Pakrouski, T. Stankevic, R. M. Lutchyn, P. Krogstrup, R. Feidenhans'l, S. Kraemer, C. Nayak, M. Troyer, C. M. Marcus, and C. J. Palmstrøm, Two-dimensional epitaxial superconductor-semiconductor heterostructures: A platform for topological superconducting networks, Phys. Rev. B **93**, 155402 (2016).

[8] C. M. Moehle, P. K. Rout, N. A. Jainandunsing, D. Kuiri, C. T. Ke, D. Xiao, C. Thomas, M. J. Manfra, M. P. Nowak, and S. Goswami, Controlling Andreev bound states with the magnetic vector potential, Nano Lett. **22**, 8601 (2022).

[9] F. Pientka, A. Keselman, E. Berg, A. Yacoby, A. Stern, and B. I. Halperin, Topological superconductivity in a planar Josephson junction, Phys. Rev. X **7**, 021032 (2017).

[10] M. Hell, M. Leijnse, and K. Flensberg, Two-dimensional platform for networks of Majorana bound states, Phys. Rev. Lett. **118**, 107701 (2017).

[11] M. Kjaergaard, F. Nichele, H. J. Suominen, M. P. Nowak, M. Wimmer, A. R. Akhmerov, J. A. Folk, K. Flensberg, J. Shabani, C. J. Palmstrøm, and C. M. Marcus, Quantized conductance doubling and hard gap in a two-dimensional semiconductor–superconductor heterostructure, Nat. Commun. **7**, 12841 (2016).

[12] T. O. Rosdahl, A. Vuik, M. Kjaergaard, and A. R. Akhmerov, Andreev rectifier: A nonlocal conductance signature of topological phase transitions, Phys. Rev. B **97**, 045421 (2018).

[13] D. Kuiri and M. P. Nowak, Nonlocal transport signatures of topological superconductivity in a phase-biased planar Josephson junction, Phys. Rev. B **108**, 205405 (2023).

[14] M. C. Dartiailh, W. Mayer, J. Yuan, K. S. Wickramasinghe, A. Matos-Abiague, I. Žutić, and J. Shabani, Phase signature of topological transition in Josephson junctions, Phys. Rev. Lett. **126**, 036802 (2021).

[15] H. J. Suominen, M. Kjaergaard, A. R. Hamilton, J. Shabani, C. J. Palmstrøm, C. M. Marcus, and F. Nichele, Zero-energy modes from coalescing Andreev states in a two-dimensional semiconductor-superconductor hybrid platform, Phys. Rev. Lett. **119**, 176805 (2017).

[16] J. C. Cuevas and H. Pothier, Voltage-induced Shapiro steps in a superconducting multiterminal structure, Phys. Rev. B **75**, 174513 (2007).

[17] A. H. Pfeffer, J. E. Duvauchelle, H. Courtois, R. Mélin, D. Feinberg, and F. Lefloch, Subgap structure in the conductance of a three-terminal Josephson junction, Phys. Rev. B **90**, 075401 (2014).

[18] N. Pankratova, H. Lee, R. Kuzmin, K. Wickramasinghe, W. Mayer, J. Yuan, M. G. Vavilov, J. Shabani, and V. E. Manucharyan, Multiterminal Josephson effect, Phys. Rev. X **10**, 031051 (2020).

[19] M. P. Nowak, M. Wimmer, and A. R. Akhmerov, Supercurrent carried by nonequilibrium quasiparticles in a multiterminal Josephson junction, Phys. Rev. B **99**, 075416 (2019).

[20] E. G. Arnault, S. Idris, A. McConnell, L. Zhao, T. F. Larson, K. Watanabe, T. Taniguchi, G. Finkelstein, and F. Amet, Dynamical stabilization of multiplet supercurrents in multiterminal Josephson junctions, Nano Lett. **22**, 7073 (2022).

[21] G. V. Graziano, J. S. Lee, M. Pendharkar, C. J. Palmstrøm, and V. S. Pribiag, Transport studies in a gate-tunable three-terminal Josephson junction, Phys. Rev. B **101**, 054510 (2020).

[22] G. V. Graziano, M. Gupta, M. Pendharkar, J. T. Dong, C. P. Dempsey, C. Palmstrøm, and V. S. Pribiag, Selective control of conductance modes in multi-terminal Josephson junctions, Nat. Commun. **13**, 5933 (2022).

[23] J. Cayao and M. Sato, Non-Hermitian multiterminal phase-biased Josephson junctions, Phys. Rev. B **110**, 235426 (2024).

[24] K.-F. Huang, Y. Ronen, R. Mélin, D. Feinberg, K. Watanabe, T. Taniguchi, and P. Kim, Evidence for 4*e* charge of Cooper quartets in a biased multi-terminal graphene-based Josephson junction, Nat. Commun. **13**, 3032 (2022).

[25] R. Mélin and D. Feinberg, Quantum interferometer for quartets in superconducting three-terminal Josephson junctions, Phys. Rev. B **107**, L161405 (2023).

[26] T. Jonckheere, J. Rech, C. Padurariu, L. Raymond, T. Martin, and D. Feinberg, Quartet currents in a biased three-terminal diffusive Josephson junction, Phys. Rev. B **108**, 214517 (2023).

[27] A. Freyn, B. Douçot, D. Feinberg, and R. Mélin, Production of nonlocal quartets and phase-sensitive entanglement in a superconducting beam splitter, Phys. Rev. Lett. **106**, 257005 (2011).

[28] M. Gupta, G. V. Graziano, M. Pendharkar, J. T. Dong, C. P. Dempsey, C. Palmstrøm, and V. S. Pribiag, Gate-tunable superconducting diode effect in a three-terminal Josephson device, Nat. Commun. **14**, 3078 (2023).

[29] M. Coraiola, A. E. Svetogorov, D. Z. Haxell, D. Sabonis, M. Hinderling, S. C. ten Kate, E. Cheah, F. Krizek, R. Schott, W. Wegscheider, J. C. Cuevas, W. Belzig, and F. Nichele, Flux-tunable Josephson diode effect in a hybrid four-terminal Josephson junction, ACS Nano **18**, 9221 (2024).

[30] J. H. Correa and M. P. Nowak, Theory of universal diode effect in three-terminal Josephson junctions, SciPost Phys. **17**, 037 (2024).

[31] A. Maiellaro, J. Settino, C. Guarcello, F. Romeo, and R. Citro, Hallmarks of orbital-flavored Majorana states in Josephson junctions based on oxide nanochannels, Phys. Rev. B **107**, L201405 (2023).

[32] A. Maiellaro, M. Trama, J. Settino, C. Guarcello, F. Romeo, and R. Citro, Engineered Josephson diode effect in kinked Rashba nanochannels, SciPost Phys. **17**, 101 (2024).

[33] C. Guarcello, A. Maiellaro, J. Settino, I. Gaiardoni, M. Trama, F. Romeo, and R. Citro, Probing topological superconductivity of oxide nanojunctions using fractional Shapiro steps, Chaos, Solitons Fractals **189**, 115596 (2024).

[34] C. W. J. Beenakker, Universal limit of critical-current fluctuations in mesoscopic Josephson junctions, Phys. Rev. Lett. **67**, 3836 (1991).

[35] S. V. Mironov, A. S. Mel'nikov, and A. I. Buzdin, Double path interference and magnetic oscillations in Cooper pair transport through a single nanowire, Phys. Rev. Lett. **114**, 227001 (2015).

[36] D. Sticlet, P. Wójcik, and M. P. Nowak, Squid pattern disruption in transition metal dichalcogenide Josephson junctions due to nonparabolic dispersion of the edge states, Phys. Rev. B **102**, 165407 (2020).

[37] F. Setiawan, A. Stern, and E. Berg, Topological superconductivity in planar Josephson junctions: Narrowing down to the nanowire limit, Phys. Rev. B **99**, 220506(R) (2019).

[38] T. D. Stanescu, R. M. Lutchyn, and S. Das Sarma, Majorana fermions in semiconductor nanowires, Phys. Rev. B **84**, 144522 (2011).

[39] T. D. Stanescu and S. Tewari, Majorana fermions in semiconductor nanowires: Fundamentals, modeling, and experiment, J. Phys.: Condens. Matter **25**, 233201 (2013).

[40] F. Setiawan, C.-T. Wu, and K. Levin, Full proximity treatment of topological superconductors in Josephson-junction architectures, Phys. Rev. B **99**, 174511 (2019).

[41] T. D. Stanescu, R. M. Lutchyn, and S. Das Sarma, Soft superconducting gap in semiconductor-based Majorana nanowires, Phys. Rev. B **90**, 085302 (2014).

[42] N. A. Mortensen, K. Flensberg, and A.-P. Jauho, Angle dependence of Andreev scattering at semiconductor–superconductor interfaces, Phys. Rev. B **59**, 10176 (1999).

[43] D. Sticlet, B. Nijholt, and A. Akhmerov, Robustness of Majorana bound states in the short-junction limit, Phys. Rev. B **95**, 115421 (2017).

[44] C. W. Groth, M. Wimmer, A. R. Akhmerov, and X. Waintal, KWANT: A software package for quantum transport, New J. Phys. **16**, 063065 (2014).

[45] D. Kuiri, M. P. Nowak, and P. Wójcik, Enhancement of topological regime in elongated Josephson junctions - code (2024), https://zenodo.org/records/13740205.

[46] T. Laeven, B. Nijholt, M. Wimmer, and A. R. Akhmerov, Enhanced proximity effect in zigzag-shaped Majorana Josephson junctions, Phys. Rev. Lett. **125**, 086802 (2020).

[47] R. M. Lutchyn, J. D. Sau, and S. Das Sarma, Majorana fermions and a topological phase transition in semiconductor-superconductor heterostructures, Phys. Rev. Lett. **105**, 077001 (2010).

[48] S. Hart, H. Ren, M. Kosowsky, G. Ben-Shach, P. Leubner, C. Brüne, H. Buhmann, L. W. Molenkamp, B. I. Halperin, and A. Yacoby, Controlled finite momentum pairing and spatially varying order parameter in proximitized HgTe quantum wells, Nat. Phys. **13**, 87 (2017).

[49] F. Herling, C. Morrison, C. S. Knox, S. Zhang, O. Newell, M. Myronov, E. H. Linfield, and C. H. Marrows, Spin-orbit interaction in InAs/GaSb heterostructures quantified by weak antilocalization, Phys. Rev. B **95**, 155307 (2017).

[50] J. S. Lee, B. Shojaei, M. Pendharkar, A. P. McFadden, Y. Kim, H. J. Suominen, M. Kjaergaard, F. Nichele, H. Zhang, C. M. Marcus, and C. J. Palmstrøm, Transport studies of epi-Al/InAs two-dimensional electron gas systems for required building-blocks in topological superconductor networks, Nano Lett. **19**, 3083 (2019).

[51] M. P. Nowak and P. Wójcik, Renormalization of the Majorana bound state decay length in a perpendicular magnetic field, Phys. Rev. B **97**, 045419 (2018).

[52] B. H. Wu, S. A. Hassan, X. F. Xu, C. R. Wang, W. J. Gong, and J. C. Cao, Quantum transport of planar Josephson junctions with Majorana bound states, Phys. Rev. B **102**, 085414 (2020).

[53] S. Głodzik, N. Sedlmayr, and T. Domański, How to measure the Majorana polarization of a topological planar Josephson junction, Phys. Rev. B **102**, 085411 (2020).

Chapter 8

Summary

The main goal of this thesis is to study ABSs and MBSs in JJs, since JJs offer a robust architecture for realizing MZMs with potential applications in quantum computing. To this end, we employed numerical and analytical models and compared them with experiments to reveal how superconducting phase difference, magnetic field, SOC, disorder, and device geometry affect confined states in JJs.

We demonstrated that in planar JJs, the magnetic vector potential induces opposite superconducting phase differences at the two ends of the junction. As a result, tunneling spectroscopy probes detect only localized ABSs in their vicinity, giving rise to abrupt phase jumps, spectral skewness, and opposite shifts between the two ends. Our model and numerical simulations reproduced the experimental findings, highlighting that the observed behavior originates from ABSs localized at the junction ends near the barriers.

We then studied nonlocal conductance as a probe of the topological phase. We showed that a sign change in the zero-energy nonlocal conductance provides a signature of the topological transition, associated with a fermion parity change. At the same time, we revealed that finite loop inductance in phase-biased devices causes phase slips, preventing access to the crucial phase interval near $\phi = \pi$ where MZMs appear. These findings clarify experimental limitations and point toward design strategies, such as reducing inductance, to stabilize the topological regime.

To further enlarge the accessible topological region, we proposed junction elongation. Our simulations demonstrated that increasing the junction length linearly expands the phase interval supporting MZMs and lowers the magnetic field required for the topological transition. However, elongation of the junction introduces unwanted transverse modes that close the induced gap and destroy the MBSs. We showed that adding extra superconducting contacts suppresses these modes, restoring the topological gap. The effects of topological region enlargement were also shown to appear in critical-current measurements, making them experimentally accessible.

Overall, this thesis established how superconducting phase control, device geometry, SOC, and magnetic fields affect ABSs, MBSs, and nonlocal transport in JJs. By combining analytical

and numerical models, simulations, and direct comparison with experiments, the work advances the understanding of topological superconductivity, fills theoretical gaps, and provides practical implications for experimental realizations of MBSs in hybrid JJs.

References

[1] R. P. Feynman, International Journal of Theoretical Physics **21**, 467 (1982).

[2] M. A. Nielsen and I. L. Chuang, *Quantum Computation and Quantum Information*, 10th ed. (Cambridge University Press, Cambridge, UK, 2010).

[3] S. Sachdev, *Quantum Phase Transitions*, 2nd ed. (Cambridge University Press, Cambridge, UK, 2011).

[4] E. Dagotto, Reviews of Modern Physics **66**, 763 (1994).

[5] H. Q. Lin, Physical Review B **42**, 6561 (1990).

[6] J. Hubbard, Proceedings of the Royal Society A **276**, 238 (1963).

[7] M. Imada, A. Fujimori, and Y. Tokura, Reviews of Modern Physics **70**, 1039 (1998).

[8] L. K. Grover, Phys. Rev. Lett. **79**, 325 (1997).

[9] P. W. Shor, SIAM Journal on Computing **26**, 1484 (1997).

[10] A. W. Harrow and A. Montanaro, Nature **549**, 203 (2017).

[11] A. Kitaev, Annals of Physics **303**, 2 (2003).

[12] C. Nayak, S. H. Simon, A. Stern, M. Freedman, and S. Das Sarma, Reviews of Modern Physics **80**, 1083 (2008).

[13] Topological Quantum Matter Teaching Platform, Majoranas and quantum computation: Basic ideas, https://topocondmat.org/w2_majorana/braiding.html (2025), accessed: 2025-09-15.

[14] M. Sato and Y. Ando, Reports on Progress in Physics **80**, 076501 (2017).

[15] R. M. Lutchyn, J. D. Sau, and S. Das Sarma, Phys. Rev. Lett. **105**, 077001 (2010).

[16] Y. Oreg, G. Refael, and F. von Oppen, Phys. Rev. Lett. **105**, 177002 (2010).

[17] V. Mourik, K. Zuo, S. M. Frolov, S. R. Plissard, E. P. A. M. Bakkers, and L. P. Kouwenhoven, Science **336**, 1003 (2012).

[18] A. Fornieri, A. M. Whiticar, F. Setiawan, E. Portolés, A. C. C. Drachmann, A. Keselman, S. Gronin, C. Thomas, T. Wang, R. Kallaher, G. C. Gardner, E. Berg, M. J. Manfra, A. Stern, C. M. Marcus, and F. Nichele, Nature **569**, 89 (2019).

[19] F. Pientka, A. Keselman, E. Berg, A. Yacoby, A. Stern, and B. I. Halperin, Phys. Rev. X **7**, 021032 (2017).

[20] C. M. Moehle, P. K. Rout, N. A. Jainandunsing, D. Kuiri, C. T. Ke, D. Xiao, C. Thomas, M. J. Manfra, M. P. Nowak, and S. Goswami, Nano Letters **22**, 8601 (2022).

[21] A. Stern and E. Berg, Phys. Rev. Lett. **122**, 107701 (2019).

[22] H. Ren, F. Pientka, S. Hart, A. T. Pierce, M. Kosowsky, L. Lunczer, R. Schlereth, B. Scharf, E. M. Hankiewicz, L. W. Molenkamp, B. I. Halperin, and A. Yacoby, Nature **569**, 93 (2019).

[23] K. Kaperek, S. Heun, M. Carrega, P. Wójcik, and M. P. Nowak, Phys. Rev. B **106**, 035432 (2022).

[24] M. Hell, M. Leijnse, and K. Flensberg, Phys. Rev. Lett. **118**, 107701 (2017).

[25] T. O. Rosdahl, A. Vuik, M. Kjaergaard, and A. R. Akhmerov, Phys. Rev. B **97**, 045421 (2018).

[26] A. Banerjee, O. Lesser, M. A. Rahman, C. Thomas, T. Wang, M. J. Manfra, E. Berg, Y. Oreg, A. Stern, and C. M. Marcus, Phys. Rev. Lett. **130**, 096202 (2023).

[27] D. Kuiri and M. P. Nowak, Phys. Rev. B **108**, 205405 (2023).

[28] A. Banerjee, O. Lesser, M. A. Rahman, H.-R. Wang, M.-R. Li, A. Kringhøj, A. M. Whiticar, A. C. C. Drachmann, C. Thomas, T. Wang, M. J. Manfra, E. Berg, Y. Oreg, A. Stern, and C. M. Marcus, Phys. Rev. B **107**, 245304 (2023).

[29] M. C. Dartiailh, W. Mayer, J. Yuan, K. S. Wickramasinghe, A. Matos-Abiague, I. Žutić, and J. Shabani, Phys. Rev. Lett. **126**, 036802 (2021).

[30] D. Kuiri, P. Wójcik, and M. P. Nowak, Phys. Rev. B **111**, 085416 (2025).

[31] H. K. Onnes, Leiden Communications (1911).

[32] J. Bardeen, L. N. Cooper, and J. R. Schrieffer, Phys. Rev. **106**, 162 (1957).

[33] J. Bardeen, L. N. Cooper, and J. R. Schrieffer, Phys. Rev. **108**, 1175 (1957).

[34] P. G. D. Gennes, *Superconductivity of Metals and Alloys*, 1st ed. (CRC Press, 1999).

[35] M. Tinkham, *Introduction to Superconductivity*, 2nd ed. (Dover Publications, Mineola, New York, 1996).

[36] B. Josephson, Physics Letters **1**, 251 (1962).

[37] J. F. Annett, *Superconductivity, Superfluids and Condensates*, 1st ed. (Oxford University Press, 2004).

[38] G. E. Blonder, M. Tinkham, and T. M. Klapwijk, Phys. Rev. B **25**, 4515 (1982).

[39] C. W. J. Beenakker, Phys. Rev. B **46**, 12841 (1992).

[40] M. Kjaergaard, F. Nichele, H. J. Suominen, M. P. Nowak, M. Wimmer, A. R. Akhmerov, J. A. Folk, K. Flensberg, J. Shabani, C. J. Palmstrøm, and C. M. Marcus, Nature Communications **7**, 12841 (2016).

[41] H. Zhang, Ö. Gül, S. Conesa-Boj, M. P. Nowak, M. Wimmer, F. K. de Vries, J. van Veen, M. W. A. de Moor, J. D. S. Bommer, D. J. van Woerkom, D. Car, S. R. Plissard, E. P. Bakkers, M. Quintero-Pérez, M. C. Cassidy, S. Koelling, S. Goswami, K. Watanabe, T. Taniguchi, and L. P. Kouwenhoven, Nature Communications **8**, 16025 (2017).

[42] I. O. Kulik, Soviet Physics JETP **30**, 944 (1970).

[43] I. O. Kulik, Zh. Eksp. Teor. Fiz. **57**, 1741 (1969), also available in English translation as Soviet Physics JETP.

[44] A. M. Zagoskin, *Quantum Theory of Many-Body Systems: Techniques and Applications* (Springer, New York, 2014).

[45] M. Leijnse and K. Flensberg, Semiconductor Science and Technology **27**, 124003 (2012).

[46] C. Nayak, S. H. Simon, A. Stern, M. Freedman, and S. Das Sarma, Rev. Mod. Phys. **80**, 1083 (2008).

[47] C. Beenakker, Annual Review of Condensed Matter Physics **4**, 113 (2013).

[48] C. W. J. Beenakker, Rev. Mod. Phys. **87**, 1037 (2015).

[49] P. Marra, Journal of Applied Physics **132**, 231101 (2022).

[50] S. M. Albrecht, A. P. Higginbotham, M. Madsen, F. Kuemmeth, T. S. Jespersen, J. Nygård, P. Krogstrup, and C. M. Marcus, Nature **531**, 206 (2016).

[51] J. Klinovaja and D. Loss, Phys. Rev. B **86**, 085408 (2012).

[52] L. Fidkowski and A. Kitaev, Phys. Rev. B **81**, 134509 (2010).

[53] L. Fu, Phys. Rev. Lett. **104**, 056402 (2010).

[54] A. M. Turner, F. Pollmann, and E. Berg, Phys. Rev. B **83**, 075102 (2011).

[55] Y. Tanaka, S. Tamura, and J. Cayao, Prog. Theor. Exp. Phys. **2024**, ptae065 (2024).

[56] A. Y. Kitaev, Physics-Uspekhi **44**, 131 (2001).

[57] R. M. Lutchyn, E. P. A. M. Bakkers, L. P. Kouwenhoven, P. Krogstrup, C. M. Marcus, and Y. Oreg, Nature Reviews Materials **3**, 52 (2018).

[58] M. T. Deng, C. L. Yu, G. Y. Huang, M. Larsson, P. Caroff, and H. Q. Xu, Nano Letters **12**, 6414 (2012).

[59] A. Das, Y. Ronen, Y. Most, Y. Oreg, M. Heiblum, and H. Shtrikman, Nature Physics **8**, 887 (2012).

[60] A. D. K. Finck, D. J. Van Harlingen, P. K. Mohseni, K. Jung, and X. Li, Phys. Rev. Lett. **110**, 126406 (2013).

[61] H. O. H. Churchill, V. Fatemi, K. Grove-Rasmussen, M. T. Deng, P. Caroff, H. Q. Xu, and C. M. Marcus, Phys. Rev. B **87**, 241401 (2013).

[62] E. J. H. Lee, X. Jiang, M. Houzet, R. Aguado, C. M. Lieber, and S. De Franceschi, Nature Nanotechnology **9**, 79 (2014).

[63] J. Liu, A. C. Potter, K. T. Law, and P. A. Lee, Phys. Rev. Lett. **109**, 267002 (2012).

[64] F. Pientka, G. Kells, A. Romito, P. W. Brouwer, and F. von Oppen, Phys. Rev. Lett. **109**, 227006 (2012).

[65] E. Prada, P. San-Jose, and R. Aguado, Phys. Rev. B **86**, 180503 (2012).

[66] G. Kells, D. Meidan, and P. W. Brouwer, Phys. Rev. B **86**, 100503 (2012).

[67] R. Žitko, J. S. Lim, R. López, and R. Aguado, Phys. Rev. B **91**, 045441 (2015).

[68] S. Datta, *Electronic Transport in Mesoscopic Systems*, Cambridge Studies in Semiconductor Physics and Microelectronic Engineering (Cambridge University Press, Cambridge, 1995).

[69] M. Büttiker, Phys. Rev. Lett. **57**, 1761 (1986).

[70] Y. V. Nazarov and Y. M. Blanter, *Quantum Transport: Introduction to Nanoscience* (Cambridge University Press, Cambridge, 2009).

[71] C. W. J. Beenakker, Rev. Mod. Phys. **69**, 731 (1997).

[72] G. Datseris and R. Fleischmann, arXiv:1905.06637 (2019), 1905.06637 .

[73] D. S. Fisher and P. A. Lee, Phys. Rev. B **23**, 6851 (1981).

[74] R. Landauer, IBM Journal of Research and Development **1**, 223 (1957).

[75] D. J. Thouless and S. Kirkpatrick, J. Phys. C: Solid State Phys. **14**, 235 (1981).

[76] P. A. Lee and D. S. Fisher, Phys. Rev. Lett. **47**, 882 (1981).

[77] A. MacKinnon, Z. Phys. B Condensed Matter **59**, 385 (1985).

[78] T. Ando, Phys. Rev. B **44**, 8017 (1991).

[79] K. Kazymyrenko and X. Waintal, Phys. Rev. B **77**, 115119 (2008).

[80] M. Wimmer and K. Richter, Journal of Computational Physics **228**, 8548 (2009).

[81] M. Settnes, S. R. Power, and A.-P. Jauho, Phys. Rev. B **91**, 125408 (2015).

[82] S. Rotter, J.-Z. Tang, L. Wirtz, J. Trost, and J. Burgdörfer, Phys. Rev. B **62**, 1950 (2000).

[83] F. Teichert, A. Zienert, J. Schuster, and M. Schreiber, Journal of Computational Physics **334**, 607 (2017).

[84] G. Thorgilsson, G. Viktorsson, and S. I. Erlingsson, Journal of Computational Physics **261**, 256 (2014).

[85] A. R. Rocha, V. M. García-Suárez, S. Bailey, C. Lambert, J. Ferrer, and S. Sanvito, Phys. Rev. B **73**, 085414 (2006).

[86] C. W. Groth, M. Wimmer, A. R. Akhmerov, and X. Waintal, New Journal of Physics **16**, 063065 (2014).

[87] X. Waintal, M. Wimmer, A. Akhmerov, C. Groth, B. K. Nikolic, M. Istas, T. Örn Rosdahl, and D. Varjas, Computational quantum transport (2024), arXiv:2407.16257 [cond-mat.mes-hall] .